

SCHRIFTENREIHE DES HZB · EXAMENSARBEITEN

Element-resolved Ultrafast Magnetization Dynamics in Ferromagnetic Alloys and Multilayers

Andrea Eschenlohr
Dissertation

Institut für Methoden und Instrumentierung
der Forschung mit Synchrotronstrahlung

November 2012

HZB–B 39

Berichte des Helmholtz-Zentrums Berlin (HZB-Berichte)

Das Helmholtz-Zentrum Berlin für Materialien und Energie gibt eine Serie von Berichten über Forschungs- und Entwicklungsergebnisse oder andere Aktivitäten des Zentrums heraus. Diese Berichte sind auf den Seiten des Zentrums elektronisch erhältlich. Alle Rechte an den Berichten liegen beim Zentrum außer das einfache Nutzungsrecht, das ein Bezieher mit dem Herunterladen erhält.

Reports of the Helmholtz Centre Berlin (HZB-Berichte)

The Helmholtz Centre Berlin for Materials and Energy publishes a series of reports on its research and development or other activities. The reports may be retrieved from the web pages of HZB and used solely for scientific, non-commercial purposes of the downloader. All other rights stay with HZB.

ISSN 1868-5781

doi: <http://dx.doi.org/10.5442/d0033>

Element-resolved Ultrafast Magnetization Dynamics in Ferromagnetic Alloys and Multilayers

Dissertation zur Erlangung des akademischen Grades
Dr. rer. nat.

eingereicht an der
Mathematisch-Naturwissenschaftlichen Fakultät
der Universität Potsdam

von

Dipl.-Phys. Andrea Eschenlohr

Potsdam, Juni 2012

Contents

<i>List of Figures</i>	5
<i>List of Tables</i>	7
1 Introduction	9
1.1 Scope of this Thesis	11
2 What is Ultrafast Demagnetization?	13
2.1 Discovery of the Effect and Review of Experimental Work	14
2.2 Phenomenological Descriptions	16
2.2.1 Rate Equation Models	16
2.2.2 Models Based on the Landau-Lifshitz Equation	18
2.2.3 Multisublattice Model	18
2.3 Microscopic Models for the Underlying Origin of Ultrafast Demagnetization	19
2.3.1 Direct Interaction Between Photons and Spins	19
2.3.2 Electron-Phonon Spin-flip Scattering	20
2.3.3 Superdiffusive Spin Transport	21
3 Ultrafast X-ray Methods for Magnetic Measurements	23
3.1 Generation of Sub-ps X-ray Pulses with the BESSY II Femtoslicing Facility	24
3.2 Laser Pump – X-ray Probe Setup	27
3.2.1 X-ray Monochromators	27
3.2.2 Pump Laser Parameters	29
3.2.3 Endstation and Detection Scheme	30
3.3 Static and Time-resolved X-ray Magnetic Circular Dichroism	31
3.3.1 Analysis Procedure for Static Spectroscopy	32
3.3.2 Time-resolved XMCD Measurements	34
4 Relation between Ultrafast Demagnetization and Exchange Interaction in Ferromagnetic Alloys	37
4.1 Transition Metal Alloys $\text{Ni}_{50}\text{Fe}_{50}$ and $\text{Ni}_{80}\text{Fe}_{20}$	38
4.1.1 Sample Structure and Static Characterization	39
4.1.2 Decoupling of Constituent Magnetic Moments on the Ultrafast Timescale	41
4.1.3 Composition Dependence of Demagnetization – Experiment vs. Theory	46
4.2 Rare Earth Alloy $\text{Gd}_{60}\text{Tb}_{40}$	51
4.2.1 Sample Structure and Static Characterization	51
4.2.2 Accessing the Timescale of Indirect Exchange Interaction	52

4.2.3	Non-equilibrium and Quasi-equilibrium Magnetization Dynamics	55
5	Influence of Hot Electron Transport on Ultrafast Demagnetization in Ferromagnetic Multilayers	59
5.1	Sample Structure and Pumping Conditions	60
5.2	Ultrafast Demagnetization of the Buried Ni Layer in Au/Ni	61
5.3	Theoretical Description of Ultrafast Demagnetization in Au/Ni	66
5.3.1	Direct Interaction Between Photons and Spins	66
5.3.2	Superdiffusive Spin Transport	67
6	Conclusion and Outlook	71
6.1	Materials Dependence of Ultrafast Demagnetization	71
6.2	Applicability of Proposed Theoretical Models for Ultrafast Demagnetization	72
6.3	Outlook	72
6.3.1	Demagnetization through Injection of Spin-polarized Electrons in Co/Ru/Fe	72
6.3.2	Methodical Improvements and Complementary X-ray Sources	73
	Bibliography	75
	Acknowledgements	85

List of Figures

2.1	Three temperature model	17
3.1	Femtosing source	25
3.2	Sequenced Femtosing mode	26
3.3	Laser pump – x-ray probe setup before upgrade	27
3.4	Laser pump – x-ray probe setup after upgrade	28
3.5	Pump laser path setup	30
3.6	Pump laser spot profile	31
3.7	X-ray magnetic circular dichroism (XMCD) chamber	32
3.8	Electronic transitions in XMCD	33
3.9	Static absorption and XMCD spectra	35
4.1	Static absorption and XMCD spectra of Ni ₅₀ Fe ₅₀ sample	39
4.2	Static absorption and XMCD spectra of Ni ₈₀ Fe ₂₀ sample	40
4.3	Time-resolved XMCD measurement of Ni ₅₀ Fe ₅₀	43
4.4	Time-resolved XMCD measurement of Ni ₈₀ Fe ₂₀	44
4.5	Time-resolved XMCD measurement of Fe	45
4.6	Demagnetization time constants vs. magnetic moments in NiFe alloy	46
4.7	Demagnetization time constants vs. Fe concentration x in Ni _{1-x} Fe _x	48
4.8	Exchange interaction vs. Fe concentration x in Ni _{1-x} Fe _x	50
4.9	Static absorption and XMCD spectra of Gd ₆₀ Tb ₄₀ sample	52
4.10	Element-specific hystereses of Gd ₆₀ Tb ₄₀	53
4.11	Time-resolved XMCD measurement of Gd ₆₀ Tb ₄₀	54
4.12	Time-resolved XMCD measurement of Gd ₆₀ Tb ₄₀ at reduced fluence	56
4.13	Low-alpha mode measurement of Gd ₆₀ Tb ₄₀	58
5.1	Pump laser absorption in Au/Ni sample.	61
5.2	Pump laser absorption in Ni reference sample	62
5.3	Ultrafast demagnetization of Au/Ni at high pump fluence	63
5.4	Ultrafast demagnetization of Au/Ni at reduced pump fluence	64
5.5	Simulated ultrafast demagnetization of Au/Ni	69
6.1	Time-resolved XMCD measurement of Co/Ru/Fe	73

List of Tables

2.1	Review of experimental work on ultrafast demagnetization	15
3.1	Comparison of Femtoslicing beamlines	29
4.1	Magnetic moments vs. stoichiometry in NiFe alloys	41
4.2	Demagnetization time constants vs. stoichiometry in NiFe alloys . .	44
4.3	Demagnetization time constants vs. stoichiometry in rare earths . .	57
5.1	Demagnetization time constants vs. fluence in Au/Ni	66

Chapter 1

Introduction

Research into ultrafast magnetization dynamics is driven both by a desire to increase our understanding of fundamental magnetic interactions, and by the technological relevance of the materials under investigation. The ultimate aim is to design new, complex magnetic materials for future storage media. But before one can move from simple model systems to more complex materials which exhibit the properties desired for technological applications, one has to understand how the interplay of fundamental magnetic interactions and materials properties creates effects such as ultrafast demagnetization [1] or all-optical magnetic switching [2].

A true understanding of the underlying origin of these phenomena requires access to the microscopic properties of the investigated samples, and ideally it should be possible to observe ultrafast magnetization dynamics on the length and time scales they occur. Consequently, research into magnetization dynamics proceeds in step with advances in instruments development and the advent of novel experimental methods. Ultrafast demagnetization, i.e. the quenching of the magnetization of a ferromagnetic sample on a sub-picosecond timescale, could only be discovered after femtosecond (fs) pulsed lasers became available, and the timescale of the observed effect was not given by the time resolution of the probe anymore. These first experimental results by Beaurepaire et al. [1] showed a decrease of the magnetization of a thin Ni film to almost half of its original value during the first picosecond (ps) after excitation with a 60 fs laser pulse. The method chosen for measuring the magnetization in this all-optical pump-probe experiment was the magneto-optical Kerr effect (MOKE). However, MOKE in the visible wavelength range is not element-sensitive. This is an obvious limitation when MOKE is applied to alloy or multilayer samples consisting of more than one element, where it is desirable to follow the transient behavior of the magnetization after laser excitation in different constituents or layers separately.

Natural candidates for element-selective magnetic measurements are spectroscopic methods using x-rays like x-ray magnetic circular dichroism (XMCD) or x-ray magnetic linear dichroism (XMLD), which are well established methods for the magnetic characterization of samples in the static case. Here, the difficulty lies in generating x-ray pulses short enough to reach the sub-ps range, and to maintain femtosecond time resolution in a laser pump – x-ray probe experiment, where temporal jitter or drift between pump and probe might occur. The demand for ultrafast x-ray experiments has spurred the development of femtosecond pulsed x-ray sources ranging in size and complexity from laboratory sources based on high harmonic generation (HHG) or laser plasma sources to large scale facilities like Femtoslicing sources at electron storage rings or free electron lasers (FEL).

The experiments presented in this thesis were performed at the Femtoslicing facility at the electron storage ring BESSY II, operated by Helmholtz Zentrum Berlin für

Materialien und Energie GmbH (HZB). Femtoslicing is a storage ring based method for generating sub-ps x-ray pulses with the help of a femtosecond laser, which imprints its time structure on an electron bunch circulating in the storage ring. The HZB Femtoslicing source, one of the few facilities of this type operating worldwide, has unique properties which make it especially suitable for experiments on ultrafast magnetization dynamics, chiefly among them circular polarization of the generated soft x-ray pulses. The L-edges of transition metals such as Ni, Fe and Co, and the M-edges of rare earths like Gd and Tb can be reached in this photon energy range, and fs time-resolved XMCD measurements provide access to the transient behavior of spin and orbital momenta.

In the following thesis I will present experimental work which takes full advantage of the element selectivity of fs time-resolved x-ray spectroscopy. The investigated samples are ferromagnetic binary alloys from transition metals or rare earths, and multilayer structures which include a ferromagnetic layer. These materials are more complex than the pure element samples used in previous experiments to demonstrate the effect of ultrafast demagnetization and establish its characteristic time constants in various pure materials, yet simple enough to contribute in solving one specific part of the puzzle of the microscopic origin of ultrafast demagnetization. Comparing the experimental results to theoretical models will further clarify certain aspects of the ultrafast demagnetization process.

One particular question motivating me was how the time constants of demagnetization are connected to the microscopic properties of a specific material. In ferromagnetic alloys, the constituents are coupled by (indirect) exchange interaction. Does this coupling persist after femtosecond laser excitation? The constituents can also carry magnetic moments that are different from each other and from the respective pure materials. How does the initial configuration of the magnetic moments influence the time constants of demagnetization? With time resolved x-ray spectroscopy, one can now resolve the contributions of the different constituents in an alloy. In this thesis, I find a transient decoupling of the sublattices during ultrafast demagnetization in NiFe alloys, leading to distinctly different time constants of demagnetization for Ni and Fe. And yet, (indirect) exchange interaction cannot be neglected in a theoretical description of ultrafast demagnetization in ferromagnetic alloys since only including it along with the magnetic moments of the constituents leads to correct predictions for the observed time constants, as measurements on both NiFe and GdTb alloys show.

Another issue that merits closer investigation is the role of hot electrons and transport effects in ultrafast demagnetization. Despite a large body of experimental and theoretical work on spin injection and spin transport in the field of magnetism, their relevance to magnetization dynamics on femtosecond timescales has not been investigated until very recently [3, 4]. Since it is difficult to separate magnetization dynamics caused by direct excitation of the sample with a femtosecond laser pulse from those induced by transport, or even to identify the latter in the first place, the investigated samples were designed to allow separating these effects by employing a multilayer structure where the cap layer is made thick enough to absorb most of the pump laser intensity. With element-specific XMCD measurements in transmission geometry, one can then look at the unpumped ferromagnetic layer. In this thesis, several proposed theories for the origin of ultrafast demagnetization are tested on a model system, clearly indicating hot electron transport as a crucial factor for the observed demagnetization.

1.1 Scope of this Thesis

After this introduction, I will give an overview over *experimental and theoretical work* done on the topic of ultrafast demagnetization in Chapter 2. I will first outline in Chapter 2.1 how the effect was discovered, characteristic time constants established for various ferromagnetic metals and the dependence of these time constants on experimental parameters, such as pump laser fluence and polarization, derived with the use of different experimental methods like MOKE, photoemission and XMCD. Chapter 2.2 will then introduce phenomenological models used for describing ultrafast magnetization dynamics, in particular the two temperature/three temperature rate equation models and models based on the Landau-Lifshitz-Gilbert and Landau-Lifshitz-Bloch equations. The search for the microscopic origin of ultrafast demagnetization is still ongoing; Chapter 2.3 will show three candidates for a theoretical description of the process, namely direct interaction between photons and spins, electron-phonon spin-flip scattering and superdiffusive spin transport.

In Chapter 3, I will introduce the *experimental technique* used for the measurements presented in this thesis, beginning with a description of how sub-ps x-ray pulses are created with Femtoslicing and how the Femtoslicing source operates at BESSY II in Chapter 3.1. Chapter 3.2 then continues with an overview of the laser pump – x-ray probe setup at the UE56/1-ZPM and -PGM beamlines. A detailed account of the analysis of static and dynamic XMCD measurements is given in Chapter 3.3.

Chapter 4 shows my *results on ferromagnetic alloys*. In Chapter 4.1, measurements on NiFe alloys will give the element-resolved, distinctly different time constants for the Ni and Fe sublattices, followed by a comparison of these time constants with applicable theoretical models, regarding their relation to the magnetic moments and the exchange interaction between the sublattices of these transition metal alloys. Then, the element-specific demagnetization measurements of GdTb alloy in Chapter 4.2 will illuminate the relation between the observed time constants and microscopic properties of rare earths.

The *results achieved on multilayer samples* will be presented in Chapter 5, showing the demagnetization of a Ni layer buried under a thick Au cap layer, along with theoretical modelling explaining the experimentally observed results through hot electron transport.

Chapter 6 contains a *conclusion* recapitulating the experimental results presented in this thesis and their interpretation, as well as an *outlook* to further experiments on the topic of ultrafast demagnetization in multi-component ferromagnetic samples.

Chapter 2

What is Ultrafast Demagnetization?

The field of magnetization dynamics covers a number of processes occurring on a wide range of timescales. In the picosecond to nanosecond range, precessional and magnetic vortex dynamics take place, as well as magnon generation and propagation and domain wall motion. Research on these topics has a close relation to technological application, in particular magnetic storage technology, since the dynamic processes studied are potentially useful for writing information in magnetic media in a very fast way. Yet writing magnetic bits by precessional switching cannot be infinitely fast: Using electron bunches accelerated to 28 GeV which generate a short and strong magnetic field pulse, it has been shown by Tudosa et al. [5] that the reversal of the magnetization in magnetic recording media does not occur in a deterministic way any more for a pulse duration of 2.3 ps. In this context, ultrafast demagnetization is interesting for potential applications since it gives rise to substantial magnetization changes on timescales of a few hundreds of femtoseconds. Yet so far, studies of ultrafast demagnetization are still at the stage of basic research, with no single phenomenological or microscopic model being able to describe the full range of experimentally observed effects in various magnetic materials.

Sub-ps magnetization dynamics occurs in ferromagnetic [1] and ferrimagnetic [6] metals and ferromagnetic [7] and antiferromagnetic [8] semiconductors. A phenomenon related to ultrafast demagnetization is all-optical switching [2], which refers to magnetization reversal induced by femtosecond laser excitation. This reversal occurs on a timescale of several picoseconds [9] to nanoseconds [10] after an initial sub-ps demagnetization, so the same or similar microscopic mechanisms might be at work here. However, all-optical switching has not been observed on such a broad class of magnetic materials as demagnetization so far, only on ferrimagnetic metals like GdFeCo [2, 9] and TbFeCo [10] alloys. The emphasis in this thesis lies on the ultrafast demagnetization of ferromagnetic metals.

The following chapter describes the experimental and theoretical background of ultrafast demagnetization. I will outline what is known from experimental work so far about the characteristic time constants of demagnetization in elementary transition metal and rare earth ferromagnets, how these time constants were derived with the help of different experimental techniques, and their dependence on experimental parameters such as the pump laser fluence. This is succeeded by an introduction to the theoretical frameworks used to model ultrafast magnetization dynamics, going from phenomenological to microscopic models. It will also be noted where and to what degree these models have been successful in explaining experimental observations.

2.1 Discovery of the Effect and Review of Experimental Work

The advent of pulsed, femtosecond lasers in the late 1980s and early 1990s made pump-probe measurements of electron dynamics possible where the time constants of the observed effects were not solely given by the length of the pump and probe pulses any more. Pump-probe experiments were conducted on normal metals such as Au, Ag and Cu, employing reflectivity [11] or photoemission spectroscopy [12] as the probe. With laser excitation, a nonequilibrium state of the electron system before thermalization [12], which then evolves to an electron system internally thermalized at very high temperatures before thermalization with the lattice, could be accessed, which could not be achieved with slow, resistive heating. In particular, the timescales of electron thermalization [13] and ballistic electron transport [14] after laser irradiation were found in this type of experiment.

Experiments pioneering the laser excitation of ferromagnetic metals were conducted by Vaterlaus et al. [15, 16] on Gd. However, Vaterlaus et al. still worked with pump and probe pulses with a length of 10 ns and 60 ps, respectively [15]. The first observation of magnetization dynamics on the sub-picosecond timescale was made by Beaurepaire et al. [1] in 1996. Beaurepaire et al. measured hysteresis loops of a 22 nm thick Ni film via magneto-optical Kerr effect (MOKE) after excitation with a 60 fs laser pulse, for pump-probe delays up to 15 ps. They found a drop of the remanent magnetization of almost 50 % of the value for the unexcited film already within the first picosecond.

These first results were confirmed by second harmonic generation measurements [17, 18], but the extremely short decay times of the magneto-optical signal of 50 fs or even less raised questions about the interpretation of the measured signal. Indeed, Regensburger et al. [19] and Koopmans et al. [20] found that second harmonic and MOKE measurements, respectively, could be significantly influenced by optical artifacts due to reflectivity changes in the first few hundreds of femtoseconds after laser irradiation, and care has to be taken to separate the magnetic signal from these artifacts. This, and the ongoing search for a microscopic explanation of ultrafast demagnetization spurred the development of other, complementary measurement techniques, which should grant more direct access to magnetic properties such as spin moment and spin polarization of a particular sample.

Time- and spin-resolved two-photon photoemission (2PPE) measurements on 1.2 nm and 0.6 nm thick Ni films [21] found a substantial, sub-ps decrease of the spin-polarization of up to 50 % of the initial value; the demagnetization time constant of 300 fs was still limited by the laser pulse duration, but the results of Beaurepaire et al. [1] could be confirmed by a different experimental method. Later 2PPE experiments on 8 monolayer thin Fe films [22] showed demagnetization time constants ranging from 350 fs to 500 fs for a quenching of the spin polarization of 15 % to 45 %.

The development of the Femtoslicing facility at BESSY II, described in detail in Chapter 3, made it possible to measure femtosecond time-resolved x-ray magnetic circular dichroism. A decrease of the dichroic signal at the Ni L_3 -edge with a characteristic time constant of 120 ± 70 fs was found [23], representing a decrease of a linear combination of spin and orbital angular momentum on the ultrafast timescale. These results were later refined with time-resolved XMCD spectroscopy of the Ni L_3 - and L_2 -edges [24], showing the decrease of spin and orbital angular momentum separately, with a time constant of 130 ± 40 fs. So while an ultrafast reduction of a supposedly magnetic signal could not always be unambiguously attributed to an actual change of the magnetization in the past, it is now established that ultrafast demagnetization exists.

Ref.	element	ΔM [%]	t_D [fs]	method
[25]	Ni	2	74 ± 4	MOKE
[26]	Ni	2	150	MOKE
[27]	Ni	45 – 70	140 – 200	MOKE
[27]	Ni	95	180	MOKE
[23]	Ni	70	120 ± 70	XMCD
[24]	Ni	80	130 ± 40	XMCD
[28]	Fe	10 – 30	50 – 75	MOKE
[22]	Fe	30 – 45	$600 \pm 100 - 500 \pm 100$	2PPE
[27]	Co	10 – 50	160 – 240	MOKE
[29]	Gd	30	760 ± 250	XMCD
[30]	Gd	10	700	MOKE
[29]	Tb	50	740 ± 250	XMCD

Table 2.1: **Review of experimental work on ultrafast demagnetization.** Demagnetization time constants t_D from recent work are listed for the respective element, magnetization quenching ΔM and experimental method.

Ultrafast demagnetization has been observed in a number of elementary transition metals and rare earths. Characteristic time constants are typically obtained by fitting an exponential decay to the experimental data. However, one has to be careful to compare results obtained under similar experimental conditions only; this is particularly true with regard to the pump laser fluence, which is correlated to the amount of demagnetization achieved. Incident pump fluence is often not a good measure, since the actual fluence absorbed in a particular sample depends on the sample structure, such as the type and thickness of a capping layer. Instead, demagnetization time constants from literature are listed in Table 2.1 along with the corresponding magnitude of demagnetization.

Transition metals Ni, Fe and Co have been extensively investigated with various experimental methods over the last years; the results are displayed in Table 2.1. Sub-ps demagnetization in the rare earths Gd and Tb has only recently been found in time-resolved XMCD measurements; the characteristic time constants are also listed in Table 2.1.

Generally, it can be said that transition metals demagnetize faster than rare earths after laser excitation. The time constants obtained for Ni, Fe and Co with various experimental methods mostly lie in the same range, spanning 50-240 fs. The rare earths Gd and Tb also show similar time constants on the order of 750 fs. However, these time constants are at times inconsistent with each other, for example in the case of Dalla Longa et al. [25] and Koopmans et al. [26], who both measured a similar amount of demagnetization of Ni, but with time constants different by a factor of two. This merits a closer look at other experimental parameters that could influence the observed dynamics.

Dalla Longa et al. [25] measured time-resolved MOKE with left and right circularly polarized as well as linearly polarized pump pulses and found no dependence of the resulting time constant of demagnetization on the *pump polarization*. This result is also relevant in discussing direct photon-spin interaction as the microscopic origin of ultrafast demagnetization (see Chapter 2.3.1).

Koopmans et al. [20] found no dependence of the sub-ps magnetization dynamics of Ni on the strength of an *external magnetic field*.

The influence of the *base temperature* on ultrafast magnetization dynamics has been

investigated for Gd [31], showing a continuous increase in the characteristic time constant from 700 fs to 1.4 ps for a base temperature ranging from 50 K to 270 K, close to the Curie temperature of Gd.

Systematic studies of the dependence of demagnetization dynamics on the *pump fluence* have been performed for Ni and Co [27] as well as for Gd [30] and Tb [32]. Both Ni and Co show the shortest demagnetization time constants for low fluence, i.e. weak magnetization quenching. A further increase in the time constants with fluence is however not strong and the values scatter around 160 fs for 45-95 % demagnetization in Ni and 230 fs for 25-50 % demagnetization in Co [27]. A similar behavior is observed in Gd: The demagnetization time constant increases with fluence but quickly saturates [30]. Little variation of the demagnetization constant with pump fluence has been found in Tb for a magnetization quenching ranging from 50 % to almost 100 %, with the demagnetization time ranging around 1 ps [32].

Sample geometry can also be expected to play a role in ultrafast magnetization dynamics. This is particularly relevant when looking at the recovery of the magnetization back to its initial value after ultrafast demagnetization, as heat diffusion out of the excited sample volume depends on the sample thickness and substrate material [33].

It emerges that experimental parameters are indeed important, in particular pump fluence, which determines how strongly the magnetization is quenched after laser irradiation, and base temperature relative to the Curie temperature of the ferromagnet under investigation. In the remaining part of this chapter, theoretical models that aim to describe and explain these diverse experimental observations will be introduced.

2.2 Phenomenological Descriptions

One key issue in the quest for a microscopic model that successfully describes ultrafast demagnetization has been the transfer of spin angular momentum that must necessarily accompany a reduction of the magnetization. In the phenomenological models presented in this section, no mechanism for the transfer of angular momentum is explicitly included. These phenomenological models aim to describe the experimental observations of ultrafast demagnetization without assuming a particular microscopic mechanism leading to spin-flips through the exchange of energy and angular momentum between electrons, spins and the lattice.

2.2.1 Rate Equation Models

In the rate equation type of phenomenological model, namely the two-temperature (2T) and three-temperature (3T) models, electrons and lattice, and in the case of the 3T model, spins, are pictured as heat baths. These heat baths are coupled, with the strength of the coupling given through coupling constants, and can thus exchange energy. The concept of the 3T model is shown in Figure 2.1.

The 2T model was developed for characterizing laser induced electron dynamics in normal metals (see [11] and references therein). Vaterlaus et al. [15] first used such a rate equation formulation to describe magnetization dynamics, namely the spin-lattice relaxation in Gd. Beaurepaire et al. [1] combined these approaches into the 3T model upon finding a delayed response of the spin temperature, i.e. the magnetic response, compared to the electron temperature after femtosecond laser excitation.

In the framework of the 2T and 3T models the pump laser pulse affects only the electron system directly. The electron system is heated instantly to a thermalized

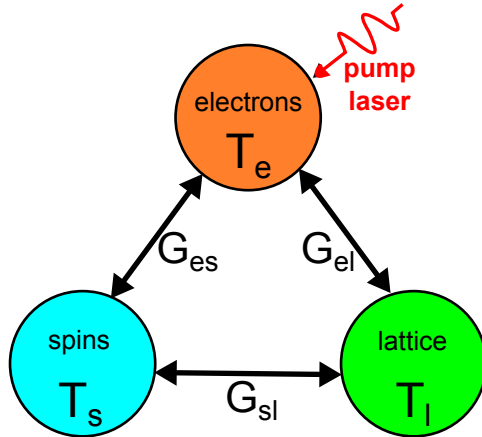


Figure 2.1: **3T model.** A schematic view of the three temperature model, which pictures electrons, spins and the lattice as heat baths which exchange energy upon the excitation of the electron system with a femtosecond laser pulse.

distribution with a corresponding temperature significantly above the initial temperature. This neglects the non-equilibrium electron distribution which has been found experimentally for the first tens of fs after laser excitation; in this state, the electron system cannot be described by a Fermi-Dirac distribution and thus no electron temperature can be derived [34]. The energy equilibration processes between the electron, spin and lattice heat baths are then described by the following rate equations [1]:

$$C_e(T_e) \frac{dT_e}{dt} = -G_{el}(T_e - T_l) - G_{es}(T_e - T_s) + P(t), \quad (2.1)$$

$$C_s(T_s) \frac{dT_s}{dt} = -G_{es}(T_s - T_e) - G_{sl}(T_s - T_l), \quad (2.2)$$

$$C_l(T_l) \frac{dT_l}{dt} = -G_{el}(T_l - T_e) - G_{sl}(T_l - T_s), \quad (2.3)$$

where C refers to the specific heat and T to the temperature, with the subscripts e , s and l denoting the electron, spin and lattice systems, respectively. G_{el} , G_{es} and G_{sl} are the coupling constants between electrons and lattice, electrons and spins, and spins and lattice, respectively. The laser heating of the electron system is introduced by the $P(t)$ term. The 2T and 3T models can be extended to include heat diffusion to the sample substrate [11].

The 3T model offers an intuitive description of the energy equilibration processes during ultrafast demagnetization and the recovery of the magnetization back to equilibrium conditions. An analytical solution of the rate equations can be used to fit experimental demagnetization data [25, 35]. But while the model can satisfactorily describe experimental observations, it has no predictive character. Input from experimental data, for example the electron-lattice thermalization time from reflectivity measurements, is needed to simulate the energy equilibration processes between electrons, spins and the lattice.

2.2.2 Models Based on the Landau-Lifshitz Equation

The Landau-Lifshitz equation describes the precessional motion of a magnetic moment $\vec{m} = V\vec{M}$, where V is the homogeneously magnetized sample volume and \vec{M} the magnetization vector, due to an effective magnetic field \vec{H}_e [36]:

$$\frac{d\vec{m}}{dt} = \gamma\vec{m} \times \vec{H}_e. \quad (2.4)$$

Here γ stands for the gyromagnetic ratio. \vec{H}_e is an effective magnetic field containing the external magnetic field applied to the magnetic material, as well as magneto-crystalline anisotropy, shape anisotropy, and other sample and material dependent contributions. A damping term is added to equation 2.4 in order to include relaxation of the precessional motion back to equilibrium, i.e. alignment parallel to \vec{H}_e , resulting in the Landau-Lifshitz-Gilbert (LLG) equation,

$$\frac{d\vec{m}}{dt} = \gamma\vec{m} \times \vec{H}_e + \frac{\alpha}{|\vec{m}|}\vec{m} \times \frac{d\vec{m}}{dt}, \quad (2.5)$$

with α being a dimensionless damping parameter. The LLG equation is valid for low temperatures and the length of the magnetization vector is conserved [37].

At higher temperatures, the length of the magnetization vector is not conserved any more and longitudinal relaxation has to be taken into account. This can be done using the Landau-Lifshitz-Bloch (LLB) equation, which is valid up to and beyond the Curie temperature T_C [37]. The LLB equation is written as

$$\frac{d\vec{m}}{dt} = \gamma\vec{m} \times \vec{H}_e - \gamma\lambda_{\parallel} \frac{(\vec{m} \cdot \vec{H}_e)\vec{m}}{m^2} + \gamma\lambda_{\perp} \frac{\vec{m} \times (\vec{m} \times \vec{H}_e)}{m^2}, \quad (2.6)$$

where λ_{\parallel} and λ_{\perp} are the dimensionless longitudinal and transversal damping parameters [36].

The LLG and LLB equations can be employed for a size of the simulated magnetic material ranging from nanometers to micrometers. In the former case, the magnetization can be described by an atomic level spin Hamiltonian. For larger sample sizes the macrospin approximation commonly used in micromagnetic simulations must be employed, where the magnetic moment is an average over all atomic magnetic moments in a particular volume. For simulations of laser induced dynamics, thermal fluctuations are included which affect \vec{H}_e . The pump laser pulse is assumed to directly heat the electron system, with the corresponding temperature calculated within the 2T model [37].

The LLG and LLB models have successfully reproduced experimental observations regarding the fluence dependence of ultrafast demagnetization in Ni [39], all-optical switching in GdFeCo [9] and laser-induced magnetization reversal in CoPt [40].

No assumptions are made about the microscopic mechanism(s) behind the damping parameters used in the LLG and LLB models. If one assumes that phonon-mediated spin-flips are the microscopic damping mechanism, the LLB model was shown [38] to be equivalent to the microscopic three-temperature model (M3TM) [27], which will be discussed in more detail in Chapter 2.3.2.

2.2.3 Multisublattice Model

In addition to elementary ferromagnets as outlined in Chapter 2.1, ultrafast demagnetization has been measured in several materials with more than one magnetic constituent. Examples include $\text{Ni}_{80}\text{Fe}_{20}$ [35, 41, 42, 43], $\text{Tb}_{35}\text{Fe}_{65}$ [6] as well as various Heusler alloys [44] and half metals [45]. This motivates a model which explicitly includes the dynamics of multiple sublattices in a magnetic material, which

was developed by Mentink et al. [46].

This model, called "multisublattice model" in the following, includes longitudinal relaxation, not only of relativistic origin, but also of exchange origin. Longitudinal relaxation due to the exchange field can only occur in magnets with more than one sublattice, since exchange relaxation conserves the total angular momentum and relaxation can thus only proceed via angular momentum transfer between the sublattices. The multisublattice model was designed to describe sub-ps magnetization dynamics on the timescale of the exchange interaction and therefore neglects transverse relaxation. The equations of motion for the magnetic moments m_i , $i = 1, 2$ of two sublattices can then be written as [46]:

$$\frac{dm_1}{dt} = \lambda_e(H_1 - H_2) + \lambda_1 H_1, \quad (2.7)$$

$$\frac{dm_2}{dt} = -\lambda_e(H_1 - H_2) + \lambda_2 H_2, \quad (2.8)$$

where H_i refers to the effective magnetic fields acting on the sublattices, λ_i is the relativistic damping parameter describing the transfer of angular momentum between the respective sublattice and the environment, and λ_e is the exchange damping parameter describing the transfer of angular momentum between the sublattices.

Laser excitation in the multisublattice model is included by adding a heat bath with a time-dependent temperature coupled to the magnetic system, similar to the LLG and LLB models presented in the previous section. However, the multisublattice model allows for the heat baths to be out of thermal equilibrium, internally and between each other [46].

Time- and element-resolved measurements of the magnetic sublattices of ferrimagnetic GdFeCo, which show transient ferromagnetic alignment during all-optical switching due to different reversal times for the Gd and FeCo sublattices [9], have been reproduced by the multisublattice model [46]. Chapter 4.1 will show that the multisublattice model can also explain the distinctly different sublattice dynamics of NiFe alloys during ultrafast demagnetization.

2.3 Microscopic Models for the Underlying Origin of Ultrafast Demagnetization

In contrast to the phenomenological models described in the previous section, the three microscopic models introduced in the following explicitly account for the transfer of spin angular momentum during ultrafast demagnetization. The first two models propose photons and phonons, respectively, as a reservoir for angular momentum. In contrast, the third model dispenses with the need for a spin-flip channel altogether by proposing sub-ps demagnetization due to an ultrafast spin current out of the excited sample volume.

2.3.1 Direct Interaction Between Photons and Spins

Direct interaction between pump laser photons and spins was the earliest microscopic explanation proposed for ultrafast demagnetization by Zhang and Hübner in 2000 [47]. According to the authors, ultrafast demagnetization occurs in the presence of both an external laser field and spin-orbit coupling, when spin-orbit coupling smears out singlet and triplet states and thus allows for optically induced spin flips.

An ongoing controversy regarding this type of microscopic model is whether the

number of photons absorbed in the magnetic material due to irradiation with realistic laser fluences is large enough to explain the experimentally observed magnitude of demagnetization [48, 49]. Also, when the pump laser photons serve as the source for the angular momentum needed to flip a spin, demagnetization should proceed differently when the pump laser beam is linearly or circularly polarized. However, Dalla Longa et al. [25] found that any polarization dependent changes in MOKE measurements are purely due to optical artifacts and the magnetization dynamics remain unchanged.

Furthermore, Zhang and Hübner [47] predict a saturation of the demagnetization at 50 % of the magnetic moment in Ni. In contrast to that, demagnetization magnitudes on the order of 70-80 % of the initial value of the magnetic moment have been found experimentally [23, 24]. Additionally, according to Zhang and Hübner [47] ultrafast demagnetization proceeds quasi-instantaneously and the observed time constant is given by the pump pulse length. But the measured demagnetization time constants are typically longer than the pump pulses employed, in particular for the rare earths Gd and Tb, which demagnetize on a timescale of 750 fs for 50 fs long pump pulses [29]. Even if pulse length limited effects are found, their unambiguous attribution to magnetization changes, instead of optical artifacts induced by reflectivity changes, remains controversial [50, 51].

Bigot et al. [52] proposed a similar microscopic mechanism, which additionally takes a laser field induced, time-dependent modification of the spin-orbit interaction into account. This leads to a coherent interaction between the pump photons and the spins, during which angular momentum transfer necessary for spin flips takes place. This model is, however, vulnerable to the same criticisms as the Zhang and Hübner [47] model.

In Chapter 5, the dependence of ultrafast demagnetization on the number of photons absorbed in a ferromagnetic layer is tested explicitly in a multilayer model system, with the result that direct interaction between photons and spins is unlikely to be the dominant cause of ultrafast demagnetization.

2.3.2 Electron-Phonon Spin-flip Scattering

Koopmans et al. [53] proposed that during ultrafast demagnetization, spin angular momentum is transferred to the lattice by way of phonon mediated spin-flip scattering. This spin-flip scattering is of the Elliot-Yafet type [54, 55] found in paramagnetic metals, where each electron-phonon scattering event can lead to a spin flip with a probability α_{EY} , which is material dependent.

The modification of Elliot-Yafet scattering for ferromagnetic metals [56] went through several iterations, starting by identifying α_{EY} , responsible for sub-ps demagnetization, with the macroscopic Gilbert damping parameter which governs precessional dynamics on a timescale of hundreds of picoseconds [26, 57]. This was shown not to be the case by time-resolved measurements on rare-earth doped $\text{Ni}_{80}\text{Fe}_{20}$ [35, 41] – the modification of the Gilbert damping parameter due to doping with heavy rare earths did not lead to changes in the demagnetization time constants as predicted by Koopmans et al. [26].

Koopmans et al. [27] continued by merging the phenomenological 3T model (see Chapter 2.2.1) with a Elliot-Yafet-like spin-flip channel, leading to the so-called microscopic three-temperature model (M3TM). This time, the underlying spin-flip probability was calculated from ab initio density functional theory [58]. The actual demagnetization rate due to electron-phonon spin-flip scattering, and whether it is large enough to explain experimental observations is however contested. Carva et al. [59] found that the demagnetization rate in thermalized electron distributions as assumed by the M3TM was too small, with only a marginal increase for non-equilibrium distributions occurring in pump-probe experiments. Essert et al. [49]

also concluded that electron-phonon spin-flip scattering is not the dominant process behind ultrafast demagnetization and stressed the importance of dynamical changes of the band structure, not included in the M3TM.

As already mentioned in Chapter 2.2.2, the M3TM is equivalent to the LLB model when electron-phonon spin-flip scattering is assumed as the underlying relaxation mechanism [38]. It will be seen in Chapter 4 that the M3TM can reproduce trends observed in demagnetization dynamics such as the scaling of the demagnetization time constant with the atomic magnetic moment, but it fails for certain ferromagnetic alloys.

Other Spin-Flip Scattering Mechanisms

Carpene et al. [28] also suggested a spin-flip mechanism similar to the M3TM, but with magnons acting as the reservoir for spin angular momentum.

Krau et al. [60] proposed a microscopic demagnetization mechanism based on electron-electron Coulomb scattering. By modelling interband scattering processes leading to a redistribution of electrons from majority to minority bands after the optical excitation of spin-polarized electrons, ultrafast demagnetization measurements of Ni and Co could be reproduced, although not without employing several fit parameters.

2.3.3 Superdiffusive Spin Transport

The newest microscopic model for the origin of ultrafast demagnetization is superdiffusive spin transport, proposed by Battiato et al. [4, 61]. This model does not include a channel for the transfer of spin angular momentum, i.e. spin flips, but explains the reduction of magnetization by spin-dependent transport of charge carriers out of a ferromagnetic layer. "Superdiffusive" refers to carrier transport which has ballistic character at the beginning but goes towards diffusive transport for longer times, and is thus not correctly described by either the ballistic or diffusive approximation for all timescales.

In the model of Battiato et al. [4], superdiffusive spin transport leads to ultrafast demagnetization in the following way: Due to pump laser irradiation of a ferromagnetic layer, electrons are excited from quasi-localized d-bands to more mobile sp-bands. This excitation is assumed to be spin conserving. Subsequently, electrons are transported superdiffusively out of the excited sample volume into the substrate. Due to the fact the majority and minority electrons have different lifetimes [62], resulting in a higher mean free path for majority electrons, magnetization is transported away from the probed volume on a sub-ps timescale.

Since the modelling of superdiffusive spin transport involves treating the electron scattering processes leading to their thermalization explicitly, the non-equilibrium state after laser excitation is included by default and the usual assumption of instant thermalization via the 2T model (see Chapter 2.2.1) avoided. Also, the real, material specific band structure is included via the energy- and spin-dependent electron lifetimes.

The amount and timescale of demagnetization resulting from superdiffusive spin transport, calculated for a 15 nm thick Ni film on an Al substrate, were found to coincide with time-resolved XMCD measurements by Stamm et al. [23]. Chapter 5 will show that ultrafast demagnetization can also be induced by superdiffusive carrier transport *into* a ferromagnetic layer, providing further evidence for the influence of transport on ultrafast magnetization dynamics.

Chapter 3

Ultrafast X-ray Methods for Magnetic Measurements

While all-optical methods are well established for time-resolved magnetic measurements (compare Chapter 2.1), x-ray methods offer some unique advantages despite more demanding requirements for the generation of short x-ray pulses and their use in pump-probe experiments. In particular, element selective measurements can be performed through core level spectroscopy [9], x-ray magnetic circular dichroism (XMCD) allows access to spin and orbital angular momenta via sum rule analysis [23, 24, 63], and antiferromagnetic order can be probed with x-ray magnetic linear dichroism (XMLD) or resonant magnetic scattering [8].

The availability of femtosecond x-ray sources for pump-probe experiments on magnetic materials has significantly increased in recent years. These sources range in size and complexity from large scale facilities, i.e. free electron lasers (FEL) [64, 65], to laboratory sources based on high harmonic generation (HHG) [66, 67] or laser plasma sources [68].

Femtosing, the method used for generating the 100 fs long x-ray pulses employed in this thesis, occupies an intermediate position between FEL and laboratory sources – it does require a large scale facility, namely an electron storage ring, to operate, but not one dedicated solely to it. Femtosing is only a local source at one insertion device of the storage ring and runs without affecting the generation and use of x-rays at other insertion devices.

In contrast to FEL and laboratory sources, the BESSY II Femtosing source routinely produces soft x-rays with circular polarization, thus allowing direct access to the dynamics of the magnetic moment at the transition metal L-edges and rare earth M-edges via XMCD [23, 24, 29, 63].

In the following chapter, the principles behind the generation of femtosecond x-ray pulses with Femtosing will be explained and the characteristics of the BESSY II source outlined. This is succeeded by a description of the laser pump – x-ray probe setup at the UE56/1-PGM and -ZPM beamlines, including the properties of pump and probe beams. Finally, the procedures used for analysing both static and time-resolved XMCD data will be detailed.

3.1 Generation of Sub-ps X-ray Pulses with the BESSY II Femtoslicing Facility

The electron bunches circulating in a storage ring have a certain temporal structure and length which is given by the settings and operation mode of this particular storage ring. The pulse length of the x-rays then created at bend magnets and insertion devices like undulators is basically given by the electron bunch length. In the BESSY II normal operation mode [69], the pulse length is on the order of 50-70 ps.

Femtoslicing is a method for generating sub-ps x-ray pulses from a storage ring source by using the interaction of an intense femtosecond laser pulse co-propagating with an electron bunch circulating in the storage ring. The electric field generated by the laser pulse modulates the energy of part of the electrons in the bunch, defining a fs "slice" of them which then generates a correspondingly short x-ray pulse. The idea behind Femtoslicing was first proposed by Zholents and Zolotarev [70] in 1996, and put into practice at the ALS in Berkeley, USA, using a bend magnet as a radiator [71]. The first undulator source for the soft x-ray range was commissioned at BESSY II in 2004 [72, 73, 74], followed in 2006 by a hard x-ray undulator source at the SLS in Villigen, Switzerland [75].

Looking at the Femtoslicing source at BESSY II in detail, the generation of femtosecond x-rays takes place in a section of the storage ring formed by a U139 planar undulator, the modulator, followed by a dipole magnet and the UE56/1 elliptical undulator, the radiator (see Figure 3.1). Energy modulation of a small part of an electron bunch stored in the ring is achieved by an intense femtosecond laser co-propagating with the electron beam through the modulator. In addition to spatial and temporal overlap of the laser spot with the electron beam, a resonance condition needs to be fulfilled for energy modulation to occur [74]:

$$\lambda_L = \frac{\lambda_U}{2\gamma^2} \left(1 + \frac{K^2}{2} \right), \quad (3.1)$$

where λ_L is the laser wavelength, λ_U the modulator period length, γ the electron Lorentz factor and K the undulator deflection parameter. The "sliced" electrons take a different path through the subsequent dipole magnet than the main electron bunch, due to the difference in energies. Then, when traveling through the radiator, they give off short x-ray pulses, which are spatially separated from the long, much more intense pulses coming from the main bunch.

The resulting x-ray pulses are tunable in energy between 400 eV and 1400 eV and their polarization can be varied between linear and circular. In Femtoslicing mode, a circular polarization degree of 70 % is achieved, due to the necessity of an efficient separation of the fs x-rays from the full ps x-ray pulse. The photon flux emitted from the radiator is on the order of 10^6 to 10^7 photons per second per 0.1 % bandwidth; the number of photons available at the experiment depends on the beamline and monochromator settings, as will be discussed in Chapter 3.2.

The x-ray pulse length is given by the laser pulse length, 26 fs slippage of the electrons with respect to the laser field, and electron path length differences between modulator and radiator, resulting in 100 fs (full width at half maximum, FWHM) in total [74]. This already includes temporal broadening due to the monochromator grating, which is on the order of 30 fs (see Chapter 3.2 for details on the PGM and ZPM monochromators).

In addition to short soft x-ray pulses, the Femtoslicing source also generates THz radiation. The laser-induced energy modulation of the "sliced" electrons creates a corresponding dip in the profile of the main electron bunch, leading to the emission

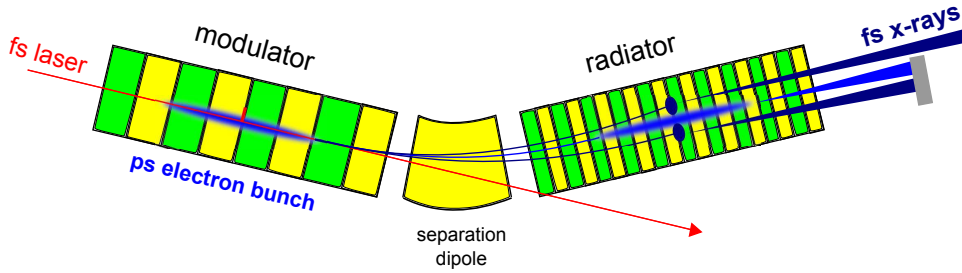


Figure 3.1: **Femtosing source.** Schematically shown are the energy modulation of a small part of the ps electron bunch by the fs laser during their overlap in the modulator, followed by the spatial separation of the energy modulated electrons from the main bunch and subsequent radiation of fs x-rays in the radiator.

of coherent synchrotron radiation in the THz range at a bend magnet further downstream of the Femtoslicing source [73, 74]. This dip and the resulting THz emission persist over several turns in the storage ring. The intensity of the THz radiation from the first turn and the ratio between the first and second turn radiation are an indication of the spatial and temporal overlap of the laser and the electron beam and the magnitude of the energy modulation of the electrons. The THz radiation thus serves as a diagnostics tool for the generation of fs x-rays, and is employed for optimizing the output, either manually or in an automated feedback loop.

Since the 100 fs short x-ray pulses generated with Femtoslicing originate only from a small part of an electron bunch, their short duration comes at the cost of substantially decreased intensity compared to the standard ps x-ray pulses. Consequently, the separation of the femtosecond x-rays from background radiation is particularly important.

Background radiation has several origins: Part comes from residual ps radiation. The bend magnets between modulator and radiator and after the radiator also generate radiation, but at the BESSY II Femtoslicing source they are positioned such that they do not radiate into the UE56/1-PGM and -ZPM beamlines. Another part of the background is the so-called halo, which is caused by the increased emittance of the energy modulated electrons during their relaxation and lasts about 1 ms [74]. At the BESSY II Femtoslicing source, two unique methods have been developed for dealing with the issue of background radiation.

The so-called femtobump is a local adjustment to the electron orbit in the storage ring used for steering the "sliced" electrons onto the radiator axis. When the femtobump is switched on, the fs x-rays take the same path as the ps x-rays when the femtobump is off. This way, femtobump allows for the angular separation of the x-rays generated by the unaffected electron bunch and those from the sliced electrons without any changes to the beamline and monochromator settings, by carefully positioning the front end apertures such that the off-axis radiation is blocked. It should also be noted that since the femtobump can be switched on and off by the accelerator operator within minutes, a quick change from normal mode operation to slicing operation and back is possible.

Also particular to the BESSY II Femtoslicing source is the sequenced mode, shown schematically in Figure 3.2. Part of the background, the halo, increases with the repetition rate of the laser. In order to counteract this, three additional electron bunches, separated by 12 ns and carrying a bunch charge of 5 mA, are injected on top of the multibunch train in the BESSY II normal operation mode [69]. The synchronization of the laser with the storage ring master clock is then modulated such

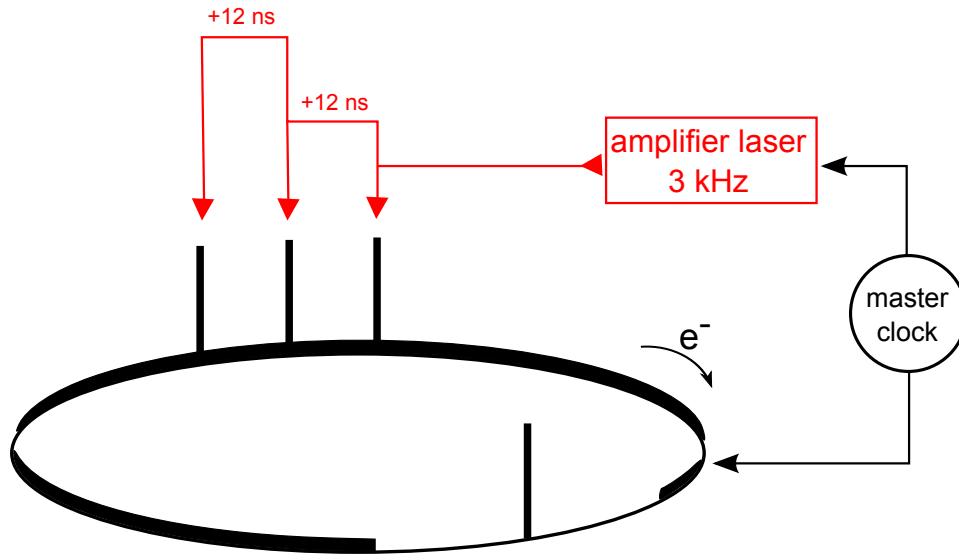


Figure 3.2: **Sequenced Femtoslicing mode.** A schematic view of the sequenced Femtoslicing mode, where the synchronization of the amplifier laser is modulated such that the fs x-rays are alternately generated from three electron bunches injected on top of the multibunch train in the BESSY II storage ring.

that fs x-rays are generated alternately from these three electron bunches. This effectively divides the repetition rate of the laser acting on one electron bunch by three, thus giving the electrons more time to relax and keeping the halo background at tolerable levels.

In the second half of 2010, the BESSY II Femtoslicing facility underwent a substantial upgrade with the installation of a new laser system. The old laser system, an oscillator and multipass amplifier manufactured by KMLabs, running at 3 kHz repetition rate with 2 mJ power per pulse, was replaced by combination of two regenerative amplifiers seeded from a single oscillator (all manufactured by Coherent). The two Coherent amplifiers run at a repetition rate of 6 kHz with a power per pulse of 1.8 mJ; one of them drives the Femtoslicing process itself, while the other is used as the pump laser in pump-probe experiments. The pump amplifier can also drive an optical parametric amplifier (OPA) used for generating variable pump wavelength. The OPA is under commissioning at the time of this writing. For a comparison of the layout of the experimental setup before and after the upgrade, see Figures 3.3 and 3.4, respectively.

The upgrade resulted in a substantially improved performance of the Femtoslicing facility. With two separate amplifiers, an improved fs x-ray flux does not come at the cost of decreased power available for pumping, i.e. exciting the sample, any more, as was the case with the KMLabs single amplifier system, whose output was split with 90 % used for driving the Femtoslicing process and 10 % for pumping. With the new system the x-ray flux was roughly doubled due to the doubling of the repetition rate while keeping the power per pulse similar to the old system. Thanks to the sequenced Femtoslicing mode, the background increase due to the higher repetition rate could be kept at a tolerable level, resulting generally in a better signal/background ratio at improved stability. Consequently, less measurements time is needed to obtain data of comparable quality than before the upgrade.

Of course, the fs x-ray source is only one part of the whole laser pump – x-ray probe

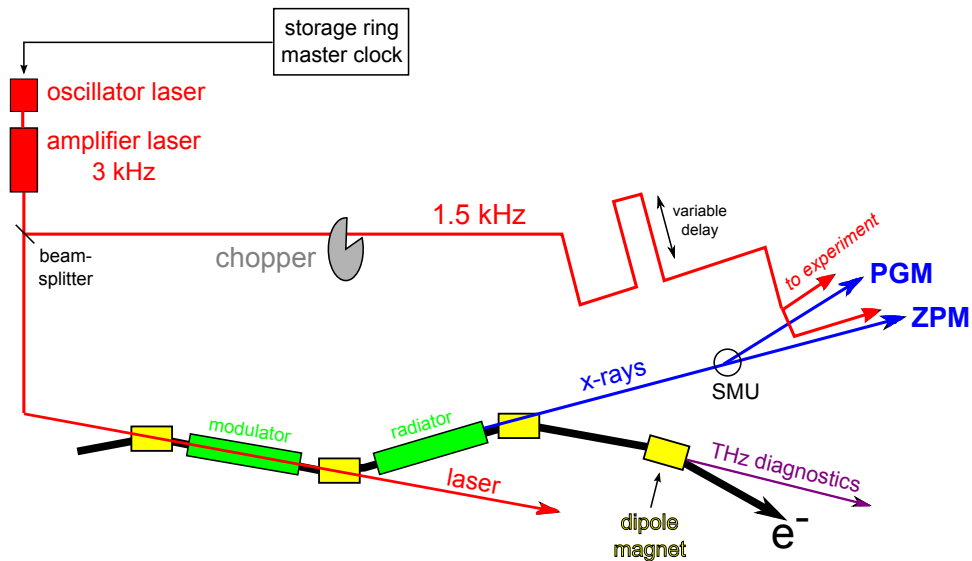


Figure 3.3: **Laser pump – x-ray probe setup before upgrade.** A schematic view of the laser pump – x-ray probe setup before the upgrade performed in the second half of 2010. 90 % of the amplifier beam is used for generating the fs x-rays in the Femtoslicing source, while the remaining 10 % are guided to the experiment in order to serve as the pump beam. SMU designates the switching mirror unit used to switch the x-ray beam between the PGM and ZPM beamlines.

setup, although the most elaborate one. Monochromatization of the x-rays, synchronization with the pump laser and the detection also influence the performance the whole Femtoslicing facility significantly, as will be described in the next section.

3.2 Laser Pump – X-ray Probe Setup

In addition to the Femtoslicing source, the laser pump – x-ray probe setup is comprised of two different beamlines, UE56/1-PGM and -ZPM, two laser hutches for housing the amplifier lasers for generating the fs x-rays and for pumping, respectively, as well as the experimental endstation containing sample with cryostat, magnet and detector.

3.2.1 X-ray Monochromators

Due to the horizontal separation scheme with the femtobump as described in Chapter 3.1, both fs and ps x-ray pulses can be used for probing at both the UE56/1-PGM and -ZPM beamlines. If the femtobump is not switched on, the 50-70 ps long pulses in normal mode are guided into the beamline. Another probing option are the approximately 10 ps (FWHM) long x-ray pulses generated in low-alpha mode. Low-alpha mode involves changing the storage ring's optics, leading to shorter electron bunches at reduced bunch charge and therefore reduced x-ray intensity. For pump-probe measurements in normal or low-alpha mode, the pump laser is synchronized to the so-called hybrid bunch, an electron bunch situated in a 100 ns long gap which separates it from the other electron bunches circulating in the storage ring and carries a charge of 10 mA in normal mode [69]. The plane grating monochromator (PGM) and zone plate monochromator (ZPM) are however not equally well

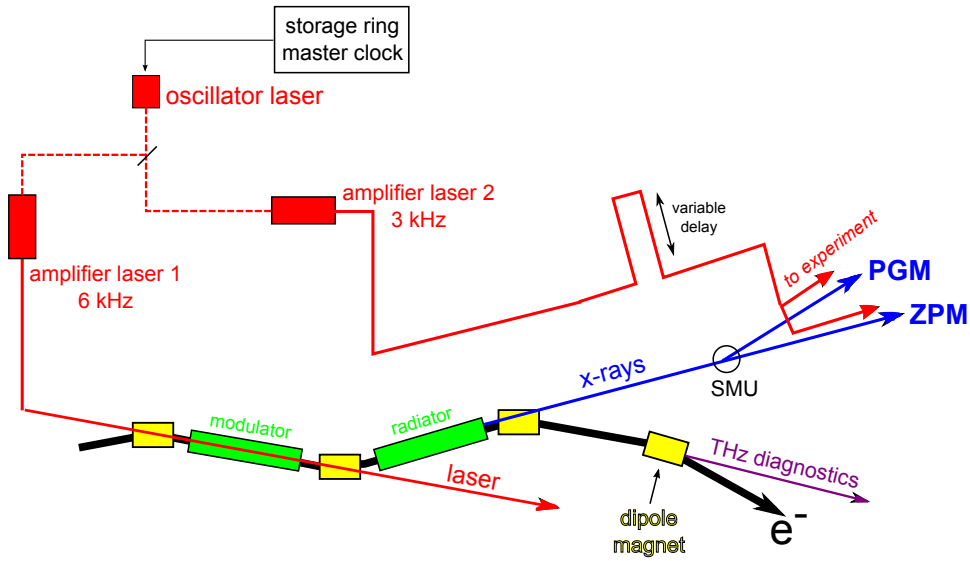


Figure 3.4: **Laser pump – x-ray probe setup after upgrade.** A schematic view of the laser pump – x-ray probe setup after the upgrade performed in the second half of 2010. Compared to Figure 3.3, two separate amplifier lasers now generate the fs x-rays and the pump pulses. Both amplifiers are seeded by the same oscillator synchronized to the storage ring master clock.

suites for all time resolutions.

The PGM is a standard monochromator design optimized for high energy resolution. Since it is comprised of five optical elements, the already strongly reduced x-ray flux in Femtoslicing mode is further reduced due to reflection losses at each optical element. Furthermore, the standard 1200 lines/mm grating used for static spectroscopy cannot be employed in Femtoslicing mode since it causes substantial pulse lengthening. Therefore, a grating with 150 lines/mm is used for fs time-resolved measurements, with a corresponding decrease in energy resolution.

In contrast, the ZPM was specifically designed for time-resolved measurements with low x-ray flux. Only one optical element, a reflection Fresnel zone plate, focusses and monochromatizes the x-rays, resulting in a beamline with a transmission about 20 times higher than the PGM beamline. Since one reflection zone plate is optimized for a particular photon energy, the whole monochromator consists of six such zone plates on a Si substrate, for covering the energy range from the O K-edge at 540 eV to the Gd and Tb M-edges around 1200 eV. Pulse lengthening is on the order of 30 fs for all photon energies covered by the ZPM, keeping the total x-ray pulse length at 100 fs after monochromatization. Drawbacks of the ZPM design are a reduced energy resolution and somewhat larger focus size compared to the PGM, as can be seen in Table 3.1.

Comparing the two monochromators, it is obvious that the ZPM is better suited for measurements in Femtoslicing mode if a moderate energy resolution is sufficient, which is the case for XMCD measurements as will be explained in Chapter 3.3. Therefore, static measurements shown in this thesis were performed at the PGM and time-resolved measurements at the ZPM.

	PGM (150 lines/mm)	ZPM
number of photons [1/s/0.1 % BW]	10^5	10^6
focus size [μm^2]	85×15	300×100
energy resolution [$E/\Delta E$]	1000	500

Table 3.1: **Comparison of Femtoslicing beamlines.** *Listed are the beamline parameters for the UE56/1-PGM and -ZPM beamlines with 100 μm exit slit, in the case of the PGM for the 150 lines/mm grating. The focus sizes are given in horizontal \times vertical size. BW refers to bandwidth, E to the photon energy.*

3.2.2 Pump Laser Parameters

Pump-probe experiments in Femtoslicing mode feature an intrinsic, jitter-free synchronization between laser and x-ray pulses, since both are generated from the same source. Maintaining a stable temporal and spatial overlap of pump and probe is paramount for taking full advantage of this feature, since drifts and instabilities can introduce temporal uncertainties, in particular over the long measurement times (days and weeks) and the large distances between Femtoslicing source, laser oscillator and amplifiers and sample position involved in the experiment.

The laser pulse length is 50 fs, as verified by autocorrelation measurements. In all measurements shown in this thesis, the fundamental wavelength of 780 nm was used for exciting the sample. In order to be particularly sensitive to pump-induced changes of the magnetic signal, the pump-probe signal is acquired alternately with just the probe signal. Consequently, in Femtoslicing mode the repetition rate of the pump laser has to be half of the x-ray repetition rate of 6 kHz. Therefore, the repetition rate of the pump amplifier is electronically set to 3 kHz. Before the laser upgrade, when both beams for pumping and generating the fs x-rays came from the same amplifier, this was achieved with a synchronized chopper in the pump path blocking every other laser pulse, resulting in a pump repetition rate of 1.5 kHz at a probe repetition rate of 3 kHz (compare Figure 3.3). The pump laser path setup at the experiment is shown in Figure 3.5.

Typical pump laser spot sizes are on the order of 800 μm diameter (FWHM), large enough to cover the x-ray probe spot, i.e. the focus size as listed in Table 3.1, and thus ensuring homogeneous excitation of the sample over the whole probed area. The spot size is adjusted by a telescope made of two pairs of cylindrical lenses, which allow to change the horizontal and vertical dimensions of the spot separately. The spot diameter is determined by a Gaussian fit to the spot profile acquired with a CCD camera from a reference path with the same length as the distance between telescope and sample position. A typical pump spot profile is displayed in Figure 3.6.

For adjusting the spatial overlap of the pump and probe beams, the x-ray probe beam is threaded through a pinhole mounted on the sample holder, and the pump spot position relative to the pinhole is checked and adjusted with the help of a CCD camera monitoring the sample position. The pump spot position on the sample is kept stable with a BeamLock 4D V.4.0 manufactured by TEM Messtechnik.

The pump power is checked with a power meter with a thermal detector head, which can handle the typical pump powers in the range of 50 mW to 500 mW. Since the cw output power of the pump amplifier at 3 kHz is on the order of 5.5 W, 90 % of the pump beam is split off and dumped when the fundamental wavelength of 780 nm is used for pumping. The pump power is then regulated with a $\lambda/2$ plate followed by a polarizer.

No cross-correlation of the pump and probe pulses independent of the experiment

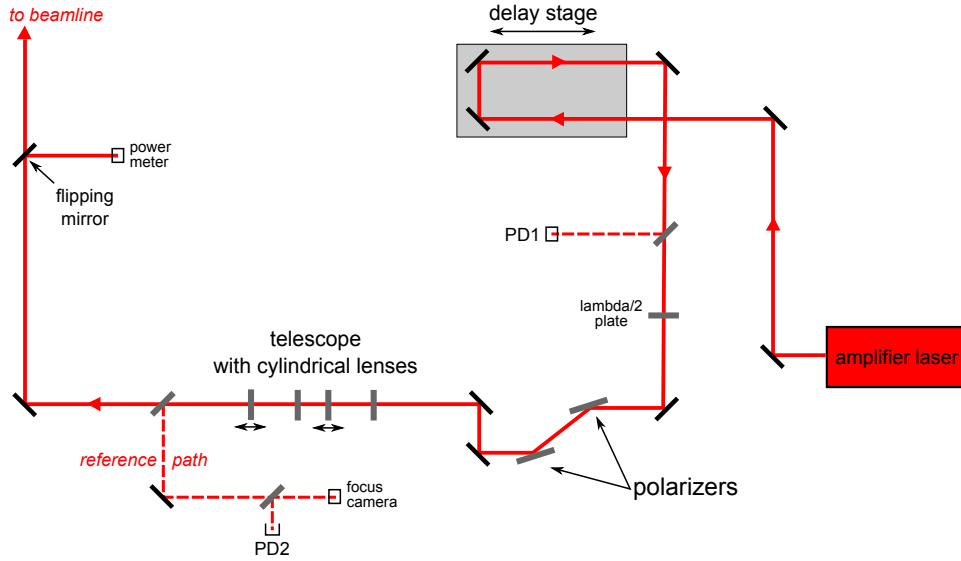


Figure 3.5: **Pump laser path setup.** A simplified view of the pump laser path setup at the experiment. The pump-probe delay is finely adjusted with a motorized optical delay stage. Photodiodes PD1 and PD2 are part of the BeamLock keeping the pump laser spot at the sample position stable. The spot size is adjusted with a telescope made of two pairs of cylindrical lenses and measured with a CCD camera in a reference path, which has the same length as the distance between telescope and sample position. The pump power is adjusted with a $\lambda/2$ plate and measured with a power meter.

is available so far. Therefore, before starting an experiment in Femtoslicing mode, pump-probe delay scans with the normal mode ps x-ray pulses are performed, narrowing down the window of pump-probe overlap which can then be scanned further in Femtoslicing mode. The pump-probe delay is finely adjusted with a motorized optical delay stage covering a maximum range of 1.6 ns. Due to the jitter-free synchronization of the 50 fs pump and 100 fs probe pulses, the total time resolution of the pump-probe experiment is 130 fs (FWHM). Drift of the pump-probe temporal overlap, i.e. time zero, can occur due to temperature and air pressure changes since the oscillator beam for seeding the pump amplifier is guided over a 40 m long transfer line under prevacuum. These drifts can be on the order of 200-400 fs over a whole day if strong changes in temperature from daytime to night occur, but they can also be corrected in the XMCD data, as will be described in Chapters 4.1 and 5.

3.2.3 Endstation and Detection Scheme

The static and time-resolved XMCD measurements presented in this thesis were performed in transmission geometry. The UHV chamber used, shown in Figure 3.7, is made of two parts: the measurement chamber holding the sample, and the detector chamber. Pump laser and probe x-rays arrive on the sample practically colinearly (angle 1.5°), ensuring that the time resolution is not smeared out due to different arrival times of the pump laser photons over the relatively large pump spot sizes typically used here. At the sample position, an external magnetic field of max. 0.55 T can be applied along the x-ray propagation direction. A cryostat allows for varying the sample temperature; depending on the type of cryostat employed, a

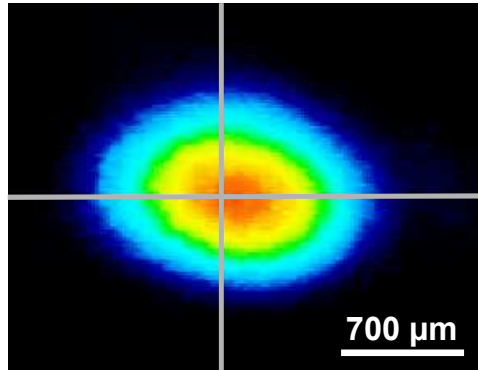


Figure 3.6: **Pump laser spot profile.** Shown here is the pump laser spot profile imaged by the CCD camera in the reference path. The spot size is determined from the FWHM of Gaussian fits to horizontal and vertical cuts through the spot profile, as indicated by the grey lines.

temperature range from 30 K to 450 K or from 120 K to 800 K can be covered. For static measurements, the transmitted intensity of the x-rays is detected with a GaAs photodiode and Keithley amperemeter. For time-resolved measurements, the detector must be gated, with a gating window smaller than 12 ns, in order to resolve the three hybrid bunches used in sequenced Femtoslicing mode (see Chapter 3.1). Therefore, and because of the low x-ray intensity, an avalanche photodiode (APD) is used, with a preamplifier and boxcar integrator. The APD, which is also sensitive in the visible wavelength range, is protected from stray pump laser light by an Al foil between the sample and the detector chamber. For measurements at the UE56/1-ZPM beamline, which does not have an exit slit, a 100 μm slit in front of the APD is used.

3.3 Static and Time-resolved X-ray Magnetic Circular Dichroism

Put simply, X-ray magnetic circular dichroism (XMCD) is the difference of the absorption of right and left circularly polarized x-rays in a ferromagnetic sample, which is proportional to the sample's magnetic moment. XMCD is the method of choice for the investigation of ferromagnetic alloys and multilayers, since it is element-selective. It thus allows to look at magnetization dynamics in different constituents or layers separately, unraveling the coupling of the components of a particular magnetic material in the process. Furthermore, spin and orbital angular moments can be determined quantitatively from absorption spectroscopy.

In a microscopic picture, XMCD arises from the interplay of the spin-orbit splitting of an initial core level state, angular momentum conservation during the photon absorption process, and the spin and orbit polarization of the final valence band states given by exchange interaction and spin-orbit coupling, respectively [76]. The electronic transitions relevant for XMCD are schematically depicted in Figure 3.8 for a prototypical 3d ferromagnet.

For the actual measurement, switching the x-ray helicity from left to right circular polarization at a fixed external magnetic field is equivalent to switching the

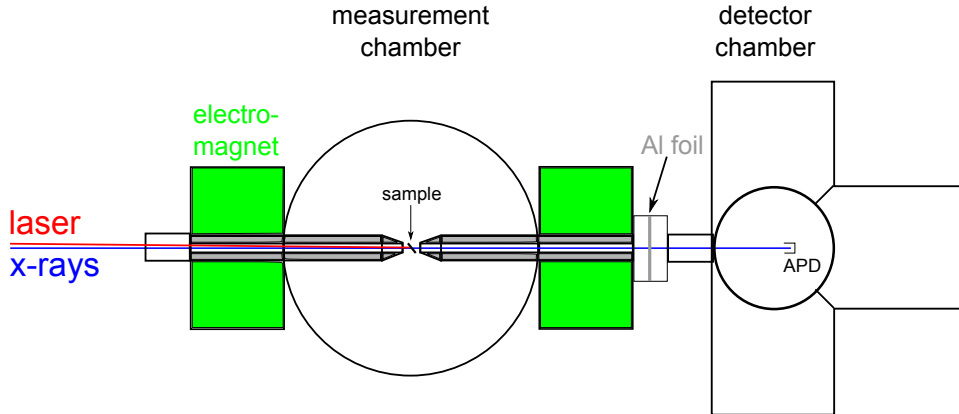


Figure 3.7: **XMCD chamber.** *X-rays and laser enter the XMCD chamber almost colinearly through the pole pieces of the electromagnet. The Al foil between the measurement and detector chambers blocks stray laser light from the detector, an avalanche photodiode (APD).*

magnetic field direction from parallel to antiparallel alignment with the x-ray propagation direction at fixed x-ray helicity [76]. The latter case is easier to realize at the Femtoslicing source since switching the typically used moderate magnetic fields of max. 0.55 T is done much faster than switching the x-ray helicity.

The XMCD signal is sensitive to the projection of the sample's magnetization in the x-ray propagation direction. The maximum dichroic effect is thus found for a parallel alignment of the external magnetic field direction with the sample's magnetization vector. Therefore, when the sample under investigation has in-plane magnetic anisotropy, it is rotated from normal incidence by a certain angle. The maximum angle in the experimental endstation shown in Figure 3.7 is 35° , given by the spacing of the pole pieces of the electromagnet.

3.3.1 Analysis Procedure for Static Spectroscopy

Before going to time-resolved measurements of the laser induced magnetization dynamics, it is important to characterize the static properties of the ferromagnet under investigation. In the following, the procedure for the analysis of static XMCD spectra will be described step by step, on the example of Ni in $\text{Ni}_{50}\text{Fe}_{50}$ measured at the UE56-1/PGM beamline.

The intensity of circularly polarized x-rays transmitted through a ferromagnetic sample, for an external magnetic field large enough to saturate the sample applied parallel and antiparallel to the x-ray propagation direction, is recorded with a GaAs photodiode and a Keithley amperemeter. This intensity is normalized to the incoming x-ray intensity, measured as the current at the last refocussing mirror of the beamline. This removes the change in x-ray intensity due to the decaying electron current in the storage ring from the spectrum. Background in the spectrum comes from absorption in the sample substrate, buffer and cap layers. This background can be removed with the help of a transmission spectrum of a reference substrate, or if this is not available, as was the case here, with the help of a linear fit to the first few datapoints below the L_3 -edge, since the background is linear over the whole energy range measured here. The absorption spectra A are then calculated from the transmission spectra T with

$$A = -\ln T. \quad (3.2)$$

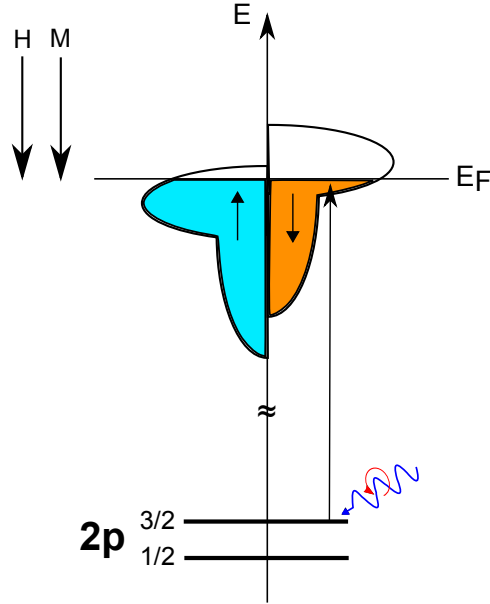


Figure 3.8: **Electronic transitions in XMCD.** A schematic view of the electronic transitions involved in XMCD of a prototypical 3d-ferromagnet, pictured in an one electron model after [76]. Electrons are excited by circularly polarized x-rays from the L core shell to empty conduction band states.

The resulting absorption spectra are shown in the upper panel of Figure 3.9. The spectrum A_{lin} , corresponding to the absorption spectrum for linearly polarized light is not measured directly, but calculated from the absorption spectra for circularly polarized light and parallel (A_+) and antiparallel (A_-) magnetic field, respectively:

$$A_{lin} = \frac{A_+ + A_-}{2}. \quad (3.3)$$

The dichroic signal D is the difference between the absorption spectra for parallel and antiparallel magnetic field,

$$D = (A_- - A_+) \frac{1/\sin \alpha}{d}, \quad (3.4)$$

multiplied with a correction factor accounting for the x-ray incident angle α , measured between x-ray propagation direction and sample normal, and circular polarization degree d , here 35% and 90%, respectively. The so-called edge jump in the absorption spectra originating from excitation into continuum states is removed with a two-step function, with the step height at the L_3 -edge set to 2/3 of the average absorption signal for the last 15 eV of the spectrum, and to 1/3 at the L_2 -edge, as outlined in [77].

Sum rules then link the integrated spectral intensities to spin and orbital angular momentum. The derivation of these sum rules can be found in [78], [79] and [80]. Here, only the resulting terms for spin moment S and orbital moment L shall be listed [24]:

$$L = -\frac{2 D_3 + D_2}{3 A_3 + A_2} \hbar n_h, \quad (3.5)$$

$$S = -\frac{1 D_3 - 2 D_2}{2 A_3 + A_2} \hbar n_h, \quad (3.6)$$

where $A_{3,2}$ and $D_{3,2}$ correspond to the integrated intensities over the absorption and dichroism spectra at the $L_{3,2}$ -edges, as indicated in Figure 3.9, and n_h to the number of holes in the valence band.

For Ni in $\text{Ni}_{50}\text{Fe}_{50}$ this gives $L = 0.13\hbar$ and $S = 0.52\hbar$ with $n_h = 1.66$ for pure Ni [81], corresponding to of total magnetic moment

$$\mu = \frac{\mu_B}{\hbar}(L + gS) = 1.18\mu_B, \quad (3.7)$$

assuming a Landé factor of $g = 2$. The resulting values for S and L are almost a factor of two larger than those for pure Ni, showing the change of magnetic moment due to alloying with Fe [82], as will be discussed in more detail in Chapter 4.1.1. These measurements also show that the orbital contribution to the total magnetic moment is much smaller than the spin part, which is generally the case for transition metals like Ni, Fe and Co [76].

For evaluating XMCD spectroscopy on rare earth elements like Gd and Tb, the sum rules for the $M_{5,4}$ -edges have different coefficients and become [32]:

$$L = -2 \frac{D_5 + D_4}{A_5 + A_4} \hbar n_h, \quad (3.8)$$

$$S = -\frac{1}{4} \frac{2D_5 - 3D_4}{A_5 + A_4} \hbar n_h. \quad (3.9)$$

Note that the magnetic dipole contribution is neglected in equations 3.6 and 3.9. This approximation is justified for Ni, Co and Fe because of the small value of the magnetic dipole term [80]. Furthermore, in polycrystalline samples it averages out [24]. The magnetic dipole term for pure Gd is exactly zero since $L = 0$ [83]. In Tb, it cannot be neglected, however, leading to a correction factor for equation 3.9 [83].

3.3.2 Time-resolved XMCD Measurements

In the dynamic case, particular attention must be paid to which quantity is measured, and whether transient, non-magnetic artifacts can influence the result.

It has been shown that the sum rules introduced in the previous section remain valid under laser excitation [84]. According to sum rules, the XMCD signal measured at the L_3 -edge of 3d metals represents a linear combination of spin angular momentum S and orbital angular momentum L , namely $S + 3/2 L$, and was found to decrease with a characteristic time constant of 120 ± 70 fs after femtosecond laser excitation in Ni [23]. By also measuring the ultrafast decrease of the XMCD signal at the Ni L_2 -edge, and thus separating the contributions of S and L via sum rule analysis, Stamm et al. [24] found a concomitant decrease of S and L with a characteristic time constant of 130 ± 40 fs. So the reduction of the XMCD signal at the 3d metal L_3 -edges can indeed be linked to a reduction of the total magnetic moment. In fact, Boeglin et al. [63] derived from fs time-resolved spectroscopy on $\text{Co}_{50}\text{Pd}_{50}$ alloy that L even decreases slightly faster than S during ultrafast demagnetization; a time constant for the reduction of L of 220 ± 20 fs was found, compared to 280 ± 20 fs for S . Also, in 3d metals L makes up only a small part of the total magnetic moment, as could be seen for the example of Ni in $\text{Ni}_{50}\text{Fe}_{50}$ in the previous section. Therefore, it is sufficient to look at the XMCD signal at the L_3 -edge of transition metals to determine the characteristic time constant of demagnetization.

A transient non-magnetic effect found during ultrafast demagnetization is a small shift of the $L_{3,2}$ -edges [23, 24]. This peakshift was linked to a transient increase of the spin-orbit interaction [24]. Since the peakshift involves only a small change of the peak position of about 130 meV and shows no dependence on the magnetization,

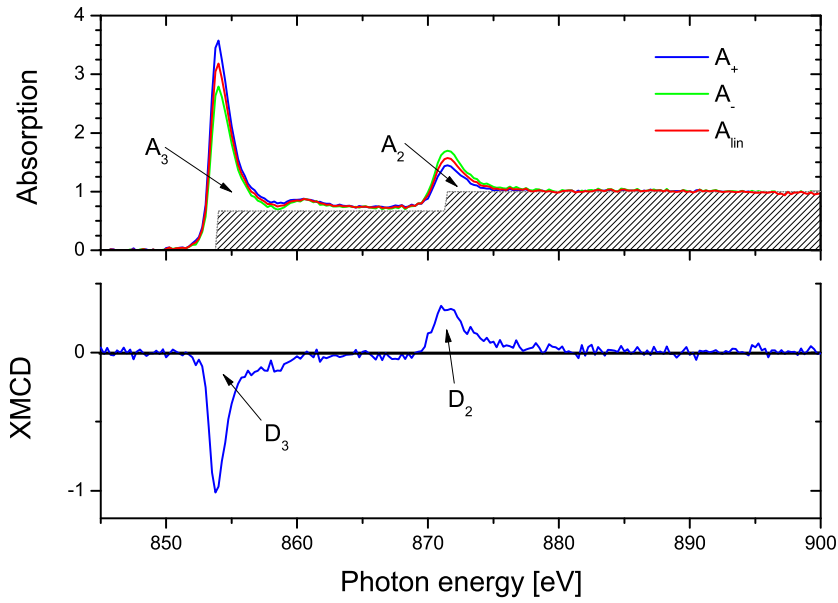


Figure 3.9: **Static absorption and XMCD spectra.** Absorption spectra at the Ni $L_{3,2}$ -edges of $Ni_{50}Fe_{50}$ for circularly polarized light and opposite orientations of the external magnetic field along the x-ray propagation direction (A_+ and A_-), as well as the absorption spectrum for linearly polarized light A_{lin} , are shown in the upper panel. The shaded area corresponds to the two-step-function used for edge jump removal as outlined in [77]. The absorption spectra are normalized to the continuum step. The resulting XMCD is plotted in the lower panel. The areas indicated under the curves are those relevant for the determination of spin and orbital angular momentum with sum rules.

it cancels out in the observed magnetization dynamics. This is in particular true for time-resolved XMCD measurements performed at the ZPM beamline, where an energy resolution of 5 eV assures that the measured magnetic signal is an integration over the whole absorption edge. The moderate energy resolution also minimizes any artifacts that might occur due to so-called bleaching or state-blocking effects in highly nonequilibrium electron distributions after laser excitation [84].

Finally, it should be noted that the value for the time-resolved XMCD signal measured at the ZPM beamline cannot easily be converted into an absolute value for the atomic magnetic moment, due to the lack of a suitable signal for the normalization of the XMCD. Since the ZPM consists of only a single set of zone plates on a Si substrate, no mirror current for the normalization of the signal can be taken like it is done at the PGM beamline. Consequently, a quantitative determination of the atomic magnetic moment has to be performed at the PGM beamline.

Chapter 4

Relation between Ultrafast Demagnetization and Exchange Interaction in Ferromagnetic Alloys

Ultrafast magnetization dynamics in ferromagnetic alloys has been studied previously with all-optical methods like magneto-optical Kerr effect (MOKE) [35, 41, 44]. However, due to the fact that MOKE in the visible wavelength range provides no element specificity, the observed magnetic signal has to be treated as an average over all constituents in the alloy. Alternatively, x-ray methods like x-ray magnetic circular dichroism (XMCD) can access the contribution of each constituent individually, but so far lacked the necessary time resolution to reach the femtosecond timescale. This ultrafast timescale is interesting since it comes close to the intrinsic timescale of exchange interaction [36]. Exchange interaction causes ferro-, antiferro- or ferrimagnetic coupling (depending on the sign of the exchange constant) of the elements that make up an alloy under static, equilibrium conditions. This is also true on a timescale of several tens of picoseconds after excitation with a magnetic field pulse; measurements of the magnetization precession on $\text{Ni}_{81}\text{Fe}_{19}$ showed coupled dynamics of the Ni and Fe magnetic moments within the experimental time resolution of 90 ps [85]. But does this still hold on the fs timescale, especially in a highly non-equilibrium state after laser excitation? With element-selective x-ray sources with sub-ps time resolution, such as Femtoslicing described in Chapter 3, it is now possible to study the transient behavior of the constituents of ferromagnetic alloys after laser excitation separately.

In the following chapter, I will present time-resolved XMCD measurements on two classes of alloys, transition metal alloys $\text{Ni}_{50}\text{Fe}_{50}$ and $\text{Ni}_{80}\text{Fe}_{20}$ and rare earth alloy $\text{Gd}_{60}\text{Tb}_{40}$. Transition metals like Ni or Fe and rare earths like Gd or Tb differ considerably in their magnetic configuration. In the transition metal case, the magnetic moment is given by the 3d electrons, which have itinerant character. But in rare earths, the magnetic moment is mainly carried by localized 4f electrons, with a small contribution by an induced magnetic moment in the 5d electrons. Already as pure materials, transition metals and rare earths show quite different dynamic behavior, qualitatively as well as quantitatively. After laser excitation, the magnetization of transition metal samples decreases with a characteristic time constant on the order of 100-300 fs [36]. In contrast, demagnetization in rare earth

samples happens in two steps. The first step occurs with a characteristic time constant of about 750 fs, while the subsequent second decrease in magnetization takes at least an order magnitude longer – values ranging from 8 ps for pure Tb to 40 ps for pure Gd have been observed experimentally [29].

Starting from such a varying behavior already for pure materials, it can be expected that the type and speed of ultrafast demagnetization also varies considerably in their alloys, depending on the type of magnetic moments of the constituents (itinerant or localized) and the kind of coupling between them. For alloys consisting of the two transition metals Ni and Fe investigated in Chapter 4.1 I will focus on the first few hundreds of femtoseconds after laser irradiation, when the material is in a non-equilibrium state. Resolving the transient behavior of the constituent elements separately will give an indication of the relation between the demagnetization time constant and materials properties like the magnetic moment and the strength of exchange interaction. When it comes to alloys made up of two rare earths, in this case Gd and Tb as shown in Chapter 4.2, also the quasi-equilibrium timescale up to a few tens of picoseconds is of interest: Looking at how the time constant of the second, slower step in the observed two-step demagnetization changes when going from pure Gd and Tb to their alloy, I can estimate the influence of indirect exchange coupling between the Gd and Tb 4f electrons in the alloy on the observed magnetization dynamics.

So for each sample class, I will describe the structure and preparation of the samples used as well as their magnetic properties as determined by static characterization. Then, the experimental results will be shown and discussed with regard to how materials properties and exchange interaction influence the time constants of the observed demagnetization; here, theoretical models will be taken into account if available.

4.1 Transition Metal Alloys $\text{Ni}_{50}\text{Fe}_{50}$ and $\text{Ni}_{80}\text{Fe}_{20}$

NiFe alloys, especially $\text{Ni}_{80}\text{Fe}_{20}$ or permalloy, are well-studied materials commonly used in magnetic devices. Favorable magnetic properties, in particular very high magnetic permeability and low coercivity, lead to frequent technological application, for example in recording heads or magnetic shielding. NiFe alloys also serve as model systems in basic research on magnetism; the observation of magnetic vortex cores [86] or domain wall dynamics [87, 88] are only two fields of study that have piqued the interest of the scientific community in recent years. Yet despite the volume of research done on these materials, some surprising behavior remained to be discovered on the sub-ps timescale: In this work, I will show that Ni and Fe magnetic moments in both $\text{Ni}_{50}\text{Fe}_{50}$ and $\text{Ni}_{80}\text{Fe}_{20}$ decrease with distinctly different time constants after laser excitation. These time constants also differ from those observed in pure Ni and Fe, and vary with the composition of the alloy. The composition dependence of the dynamical behavior already points to a relation between the demagnetization time constant and the magnetic moments of the Ni and Fe sublattices in the alloys, which can be changed from their pure element values due to alloying, and which differ depending on stoichiometry [82]. Accordingly, I will first derive the element-resolved magnetic moments in $\text{Ni}_{50}\text{Fe}_{50}$ and $\text{Ni}_{80}\text{Fe}_{20}$ from static XMCD spectroscopy via sum rule analysis [77] before presenting the element-specific transient demagnetization curves for these alloys. A comparison with theoretical models for ultrafast demagnetization shows that the observed behavior can only be explained in a satisfactory way when both the magnetic moments of the Ni and Fe sublattices as well as the exchange interaction between them is taken into account.

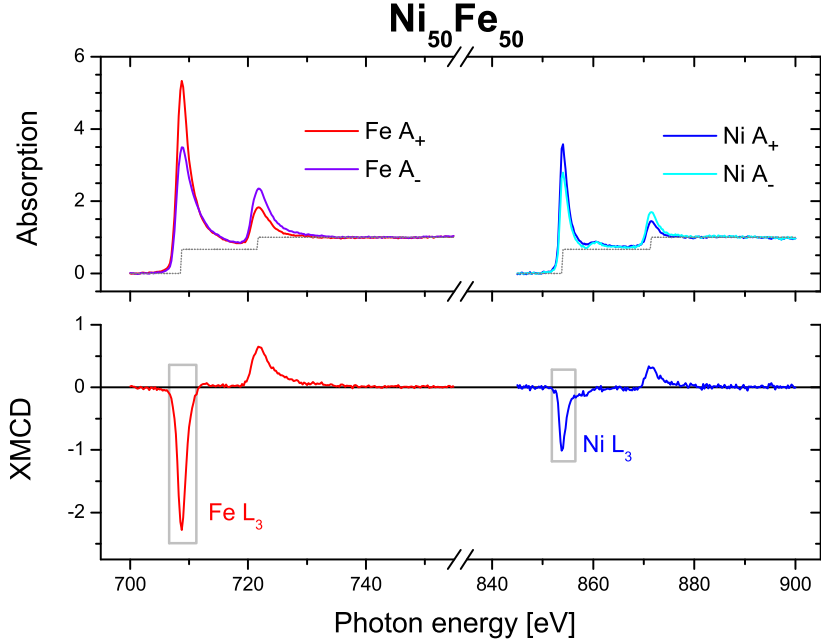


Figure 4.1: **Static absorption and XMCD spectra of $\text{Ni}_{50}\text{Fe}_{50}$ sample.** Absorption spectra at the Fe and Ni $L_{3,2}$ -edges for opposite orientations of the external magnetic field along the x-ray propagation direction (A_+ and A_-) are shown in the upper panel. The gray dotted line corresponds to the two-step-function used for edge jump removal as outlined in [77]. The absorption spectra are normalized to the continuum step. The resulting XMCD is plotted in the lower panel. The gray boxes mark the energy regions where time-resolved XMCD measurements were performed.

4.1.1 Sample Structure and Static Characterization

The $\text{Ni}_{50}\text{Fe}_{50}$ and $\text{Ni}_{80}\text{Fe}_{20}$ samples were prepared by magnetron co-sputtering from Ni and Fe targets. 500 nm thick, freestanding Al foils were used as substrates. A Pt buffer layer of 2.5 nm thickness served two purposes: first, preventing oxidation from the substrate side through pinholes in the Al foil, and second, avoiding interdiffusion of Al from the substrate into the magnetic layer, which can occur under continuous exposure to the pump laser beam. The composition of the 20 nm thick NiFe layers was controlled by adjusting the evaporation rates from the Ni and Fe targets. As the samples were not prepared in situ, a Pt cap layer, also of 2.5 nm thickness, was used to prevent oxidation. Pure Fe samples with the same thickness, substrate, buffer and cap layers were also manufactured as references for determining the demagnetization time constant of pure Fe.

The $\text{Ni}_{50}\text{Fe}_{50}$ and $\text{Ni}_{80}\text{Fe}_{20}$ samples are ferromagnetic, as can be seen from the x-ray absorption (XAS) and XMCD spectra measured at the Ni and Fe $L_{3,2}$ -edges, displayed in Figure 4.1 for $\text{Ni}_{50}\text{Fe}_{50}$ and in Figure 4.2 for $\text{Ni}_{80}\text{Fe}_{20}$. Since the samples have in-plane anisotropy, all static and time-resolved XMCD measurements shown in this section were performed under an angle of 35° between the sample normal and the direction of the incident x-rays. XMCD was measured with circularly polarized x-rays in transmission geometry, while the external magnetic field of 0.2 T applied to the sample was reversed at each step in the photon energy scan. XAS and XMCD measurements were done at room temperature. The static spectra were taken at the

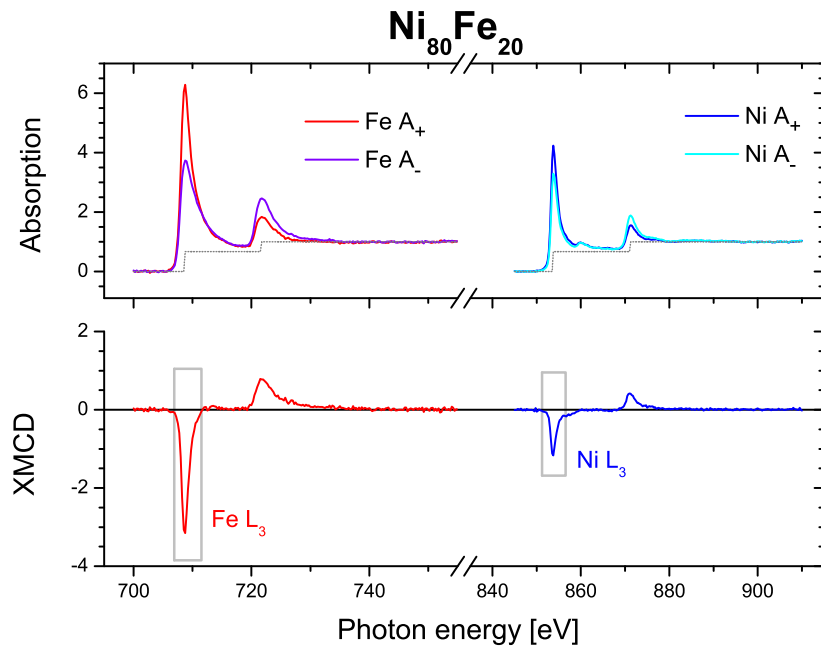


Figure 4.2: **Static absorption and XMCD spectra of $\text{Ni}_{80}\text{Fe}_{20}$ sample.** Absorption spectra at the Fe and Ni $L_{3,2}$ -edges for opposite orientations of the external magnetic field along the x-ray propagation direction (A_+ and A_-) are shown in the upper panel. The gray dotted line corresponds to the two-step-function used for edge jump removal as outlined in [77]. The absorption spectra are normalized to the continuum step. The resulting XMCD is plotted in the lower panel. The gray boxes mark the energy regions where time-resolved XMCD measurements were performed.

sample	$\mu_{\text{Ni}} [\mu_{\text{B}}]$	$\mu_{\text{Fe}} [\mu_{\text{B}}]$
Ni	0.62	–
Ni ₈₀ Fe ₂₀	0.98 ± 0.04	2.31 ± 0.09
Ni ₅₀ Fe ₅₀	1.18 ± 0.08	2.09 ± 0.08
Fe	–	2.2

Table 4.1: **Magnetic moments vs. stoichiometry in NiFe alloys.** *The element-specific magnetic moments for the NiFe alloys, derived from XMCD sum rule analysis as described in the text, are shown here. The magnetic moments for pure Ni and Fe are taken from [89].*

UE56/1-PGM beamline, a standard plane grating monochromator beamline, where proper normalization of the transmitted x-ray intensity can be assured. Background in the spectra from the Al sample substrate (and the Pt buffer and cap layers) was assumed to be linear over the measured photon energy range; hence, the background was removed with the help of a linear fit of the first few points below the L₃-edges in the absorption data. Then, XMCD sum rule analysis was performed according to the procedure outlined in Chapter 3.3 and [77] in order to obtain the magnetic moments of the Ni and Fe sublattices in the NiFe alloys. The number of holes in the valence band used for calculating spin and orbital momenta was that of pure bulk Ni, $n_{\text{h,Ni}} = 1.66$ (or Fe, $n_{\text{h,Fe}} = 3.34$) taken from [81]. The resulting total magnetic moments for the Ni and Fe sublattices of Ni₅₀Fe₅₀ and Ni₈₀Fe₂₀ are listed in Table 4.1.

When comparing the results obtained for the element-specific magnetic moments in both NiFe alloys to the literature values for pure Ni and Fe, $0.62 \mu_{\text{B}}$ and $2.2 \mu_{\text{B}}$ [89], respectively, it is immediately obvious that the Ni magnetic moments in the alloys are significantly larger than the value for pure Ni. In particular, the Ni magnetic moment in Ni₅₀Fe₅₀ increases almost by a factor of two compared to pure Ni. The Fe magnetic moments in the alloys vary to a much lesser degree and stay in the same range as the pure Fe value. This trend was also observed by Glaubitz et al. [82], who saw an increasing Ni magnetic moment with increasing Fe concentration in Fe_{1-x}Ni_x alloys, while the Fe magnetic moments remained almost constant.

4.1.2 Decoupling of Constituent Magnetic Moments on the Ultrafast Timescale

Now that I have shown what the initial configuration of the magnetic moments of the constituent elements of ferromagnetic NiFe alloys looks like, and how the magnetic moments can be significantly different from those of pure materials, I will illustrate how they evolve after excitation of the sample with a femtosecond laser pulse. The focus of this section will lie on deriving the characteristic time constants of demagnetization for each magnetic sublattice in Ni₅₀Fe₅₀ and Ni₈₀Fe₂₀, and comparing these values to the results obtained for pure Ni and Fe.

Ultrafast demagnetization of pure Ni thin films has already been studied extensively with femtosecond XMCD measurements [23, 24]; the characteristic time constant of pure Ni of 130 ± 40 fs [24] is well known. Pure Fe films have previously been studied with all-optical methods [28, 90], resulting in time constants of demagnetization of 50-75 fs for pump fluences ranging from 1.5 mJ/cm^2 to 6 mJ/cm^2 [28]. However, no measurement of the demagnetization of pure Fe with femtosecond XMCD had been performed yet. For this reason, transient XMCD of a pure Fe sample was also measured under experimental conditions comparable to the NiFe alloy measurements.

The time-resolved XMCD measurements were performed at the UE56/1-ZPM beamline, a beamline with a reflection zone plate as the single optical element used for focussing and monochromatizing the x-rays. In this way, the photon flux is maximized at the cost of a somewhat decreased energy resolution. The photon energy is tuned to the Ni L₃-edge at 853 eV or the Fe L₃-edge at 708 eV for measuring the Ni or Fe constituent in the alloys, respectively. The energy resolution of the zone plate monochromator of about 5 eV implies that the obtained XMCD signal corresponds to an integration over practically the whole L₃-edge, which assures that the XMCD signal remains a valid measure of the spin momentum despite possible effects of a laser-induced non-equilibrium distribution like state-blocking [84].

As previously mentioned in Section 4.1.1, XMCD was measured under an angle of 35° between the sample normal and the x-ray propagation direction because of the in-plane anisotropy of the samples. Furthermore, all samples were measured at room temperature, with an external applied magnetic field of ±0.2 T along the x-ray propagation direction.

As for the pump laser parameters, they differed somewhat between the measurements on Ni₅₀Fe₅₀ and pure Fe on the one hand, and the Ni₈₀Fe₂₀ measurements on the other hand, due to the extensive upgrade of the Femtoslicing facility in the second half of 2010 as detailed in Chapter 3.1. The Ni₅₀Fe₅₀ and Fe pump-probe delay scans were obtained with a pump laser repetition rate of 1.5 kHz and a pump power of 150 mW, resulting in a power per pulse of 100 μJ. Together with a pump spot diameter of 750 μm, this gives a pump fluence of 22.6 mJ/cm², as calculated with the formula

$$\rho = \frac{4E_P}{\pi d^2} \quad (4.1)$$

where ρ stands for the fluence, E_P for the power per pulse and d for the pump spot diameter¹. In contrast, the Ni₈₀Fe₂₀ delay scans were acquired with a pump repetition rate of 3 kHz and pump power of 250 mW. The resulting power per pulse of 83 μJ and the spot diameter 750 μm then correspond to a pump fluence of 18.8 mJ/cm². In both cases, the pump fluence was adjusted to reach a demagnetization of the NiFe alloy samples to about 50 % of their initial XMCD values.

In Figure 4.3, the evolution of the XMCD signal measured at the Ni and Fe L₃-edges of Ni₅₀Fe₅₀ after laser excitation is plotted versus the time delay between pump and probe pulses. The magnetic moments of both constituents of the alloy decrease by slightly more than 40 % of their initial value within the first picosecond after laser excitation. It is striking that, while the final XMCD value reached after 1 ps is similar for both constituents, ultrafast demagnetization happens much faster for Ni than for Fe in Ni₅₀Fe₅₀. The Ni magnetic moment reaches its final value already after 300 fs, while the Fe magnetic moment is still decreasing. Such dissimilar dynamic behavior means that the Ni and Fe magnetic moments are decoupled on the ultrafast timescale, despite their strong ferromagnetic coupling under equilibrium conditions. No recovery of the XMCD signal is observed within the measured delay range; recovery of the XMCD to its initial value happens on a timescale of several hundreds of picoseconds, in time for the next pump laser shot, as can be seen in time-resolved measurements that employ the full 70 ps long x-ray pulses as the probe, the so-called normal mode (see Chapter 3).

Before I come to a more quantitative description of the observed dynamics, it should be noted here that we cannot observe any shift in the onset of demagnetization of the Ni and Fe magnetic moments in alloys in this experiment. There is no cross-correlation independent of the actual measurement at the Femtosling beamlines.

¹Formula 4.1 assumes a flat-top profile of the pump spot. The actual pump spot diameter d was determined as the full width at half maximum of a Gaussian fit to the spot profile measured with a CCD camera, as shown in Chapter 3.2.2.

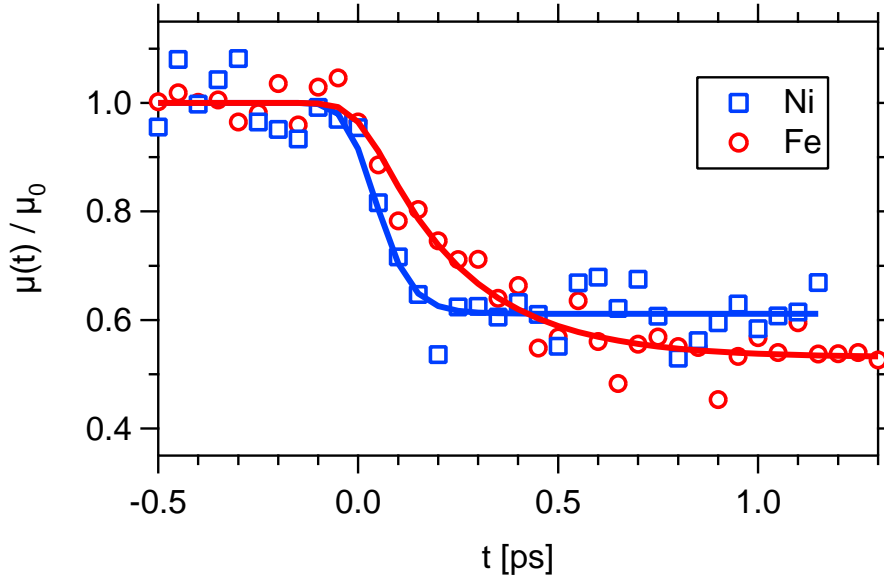


Figure 4.3: **Time-resolved XMCD measurement of $\text{Ni}_{50}\text{Fe}_{50}$.** *The evolution of the magnetic moment μ depending on the temporal delay t between pump laser and probe x-ray pulse is displayed for Ni (blue squares) and Fe (red circles) in $\text{Ni}_{50}\text{Fe}_{50}$. The blue and red lines correspond to fits to the Ni and Fe data as described in the text. μ is normalized to the average value μ_0 for the unexcited sample.*

Due to the low flux of femtosecond x-ray photons generated by Femtoslicing, cross-correlation schemes that employ changes in the optical reflectivity of GaAs substrates induced by powerful free electron laser VUV/x-ray beams [92, 93] cannot be used; so far, no other solution has been found for an independent determination of time zero. For this reason, any long-term drifts in time zero due to changes in ambient temperature or air pressure that occur over the days or weeks it takes to acquire the transient XMCD data presented here, are determined directly from the experimental data and corrected by shifting the time axis; time zero for the delay scans for the constituent magnetic moments of the NiFe alloys is accordingly set to the same delay value.

In order to derive the characteristic time constants of demagnetization for the Ni and Fe sublattices of $\text{Ni}_{50}\text{Fe}_{50}$, the datasets are fitted with an exponential decay convoluted with a Gaussian of 130 fs full width at half maximum (FWHM), which conforms to the time resolution of the experiment given by 100 fs long x-ray probe pulses and 50 fs laser pump pulses. The fit function can be written as

$$f(t) = S(t) \cdot G(t) * [A - B(1 - e^{-\frac{t}{t_D}})], \quad (4.2)$$

where $S(t)$ refers to a step function, $G(t)$ to the Gaussian representing the experimental time resolution, A to the XMCD value at negative delays, B to the amplitude of the exponential decay and t_D to the characteristic time constant of demagnetization. A single exponential decay was chosen since there occurs no further decay or recovery of the XMCD signal over the delay range investigated here. Thus, a single exponential fit adequately describes the observed behavior while involving the smallest number of free parameters.

Applying the fit function of equation 4.2 to the $\text{Ni}_{50}\text{Fe}_{50}$ delay scans returns a time constant $t_{Ni} = 60 \pm 20$ fs for the demagnetization of Ni, whereas the characteristic

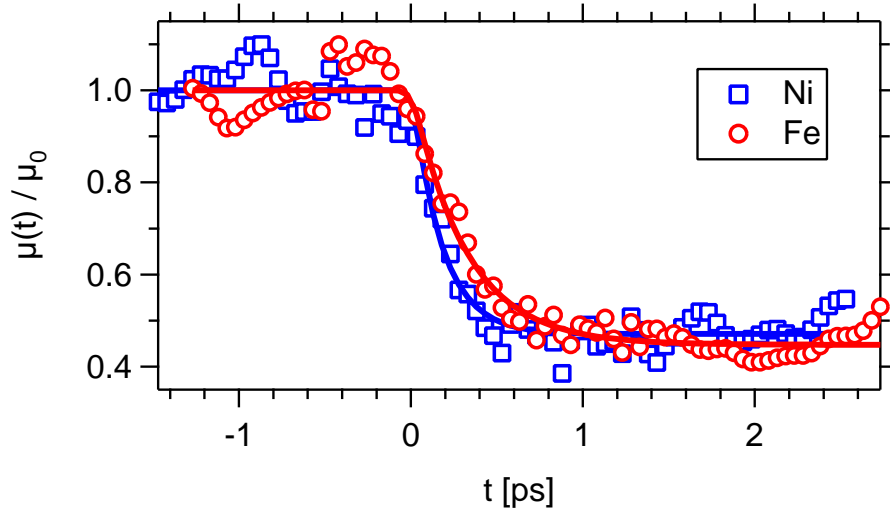


Figure 4.4: **Time-resolved XMCD measurement of $\text{Ni}_{80}\text{Fe}_{20}$.** The evolution of the magnetic moment μ depending on the pump-probe delay t is plotted for Ni (blue squares) and Fe (red circles) in $\text{Ni}_{80}\text{Fe}_{20}$. The blue and red lines correspond to fits to the Ni and Fe data as described in the text. μ is normalized to the average value μ_0 for the unexcited sample.

sample	t_{Ni} [fs]	t_{Fe} [fs]
Ni	130 ± 40	–
$\text{Ni}_{80}\text{Fe}_{20}$	170 ± 30	310 ± 40
$\text{Ni}_{50}\text{Fe}_{50}$	60 ± 20	240 ± 30
Fe	–	230 ± 40

Table 4.2: **Demagnetization time constants vs. stoichiometry in NiFe alloys.** The characteristic time constants of demagnetization for the Ni and Fe magnetic moments in the NiFe alloys, as well as for pure Fe, were derived from exponential fits to the data as described in the text. The demagnetization time constant for pure Ni is taken from [24].

time constant for Fe is $t_{\text{Fe}} = 240 \pm 30$ fs. The error bars of the time constants correspond to the standard deviation of the fit. The time constants are distinctly different; Ni in $\text{Ni}_{50}\text{Fe}_{50}$ demagnetizes faster than Fe by a factor of four.

Looking now at the time-resolved XMCD measurements for the Ni and Fe sublattices in $\text{Ni}_{80}\text{Fe}_{20}$ shown in Figure 4.4, one immediately sees that the decoupling of the Ni and Fe magnetic moments is not an anomaly only observed in the $\text{Ni}_{50}\text{Fe}_{50}$ sample. Even though the transient difference between the two delay scans is not as large as for $\text{Ni}_{50}\text{Fe}_{50}$, it is certainly present. Again, of the constituent elements, Ni shows a faster demagnetization than Fe. A fit to the data using equation 4.2 gives a characteristic time constant of demagnetization for Ni in $\text{Ni}_{80}\text{Fe}_{20}$ of 170 ± 30 fs, while the corresponding time constant for Fe is 310 ± 40 fs.

Finally, the time-resolved XMCD data measured at the L_3 -edge the pure Fe sample (see Figure 4.5) is similarly fitted with the exponential decay from equation 4.2, resulting in a characteristic time constant of 230 ± 40 fs. For convenience, a tabulation of the demagnetization time constants for all samples investigated so far is

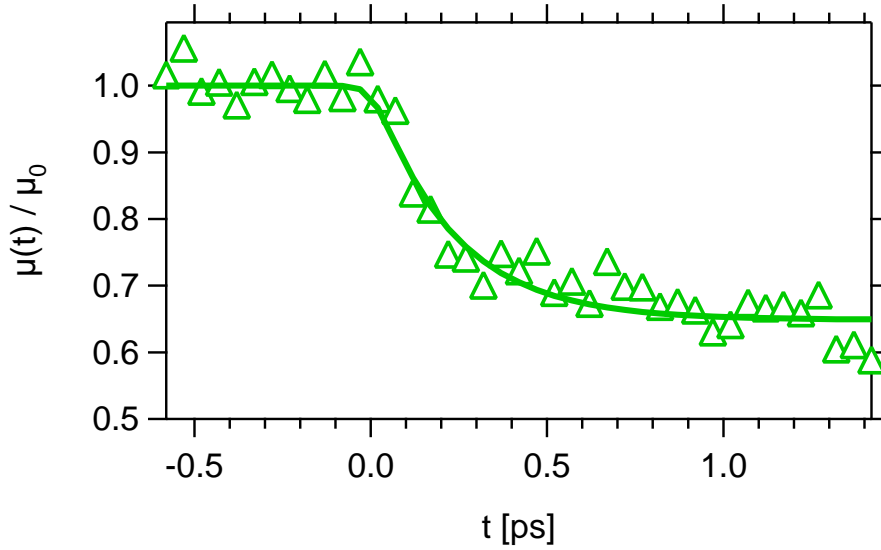


Figure 4.5: **Time-resolved XMCD measurement of Fe.** *The transient evolution of the magnetic moment μ is shown for the pure Fe sample. The line corresponds to a fit as described in the text. μ is normalized to the average value μ_0 for the unexcited sample.*

shown in Table 4.2.

Several trends can be observed in the different time constants of demagnetization for the $\text{Ni}_{50}\text{Fe}_{50}$ and $\text{Ni}_{80}\text{Fe}_{20}$ alloy samples and the pure elements Ni and Fe. First of all, ultrafast demagnetization always proceeds faster for Ni than for Fe, regardless of whether one compares pure materials or alloys. Second, the characteristic time constants of demagnetization at the Ni L_3 -edge can differ from each other in the two NiFe alloys, and the time constant of pure Ni is in turn different from those of the alloys. The same is true at the Fe L_3 -edge. Consequently, the dynamical magnetic behavior is decidedly not determined by the properties of atomic Ni or Fe. Like the strong variation of the equilibrium magnetic moments of Fe and especially Ni upon alloying already leads us to expect, the observed dynamics also vary with the alloy composition. In order to find the precise relationship between equilibrium properties and ultrafast dynamics, the interaction of the constituent atoms with their neighbours in the alloy has to be taken into account.

Furthermore, the most striking observation here is the apparent decoupling of the magnetic moments of the Ni and Fe constituent elements in $\text{Ni}_{50}\text{Fe}_{50}$ and $\text{Ni}_{80}\text{Fe}_{20}$ under non-equilibrium conditions. Initially, in the unexcited material, the Ni and Fe sublattices are strongly coupled as can be seen from static x-ray spectroscopy shown in Chapter 4.1.1. Also, after thermal equilibration of the electron system with the lattice on a timescale of several picoseconds, both Ni and Fe reach a common value mainly given by the pump fluence, i.e. the amount of excitation energy brought into the material. And yet, the strong coupling between Ni and Fe magnetic moments seen in the static case or on longer timescales does not hold in the first few hundreds of femtoseconds after laser excitation.

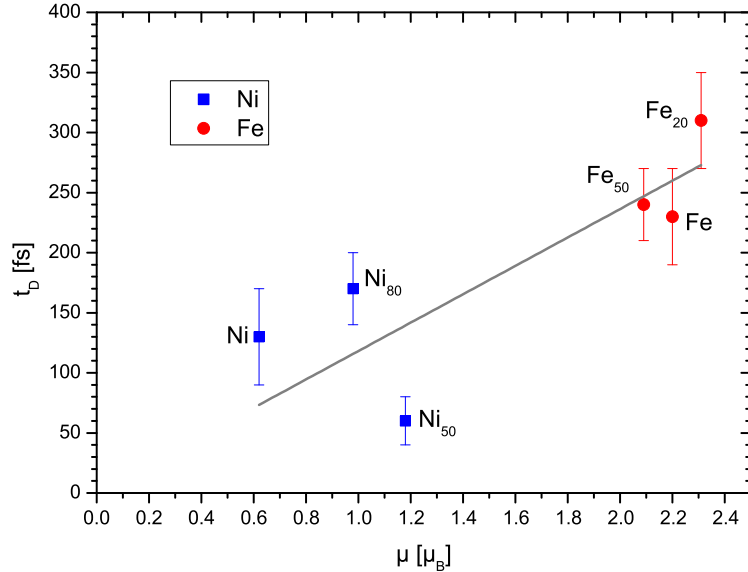


Figure 4.6: **Demagnetization time constants vs. magnetic moments in NiFe alloy.** Time constants of demagnetization t_D for the different samples investigated here, derived from fits to XMCD pump-probe delay scans, are plotted relative to the respective magnetic moments μ obtained from static XMCD spectroscopy. Pure Ni and Fe magnetic moments are taken from [89]. t_D for pure Ni is taken from [24]. In the $Ni_{50}Fe_{50}$ and $Ni_{80}Fe_{20}$ alloys, blue squares refer to the values for the Ni sublattice, red circles to the values for the Fe sublattice. The line is a guide to the eye.

4.1.3 Composition Dependence of Demagnetization – Experiment vs. Theory

The challenge now is to find out how the equilibrium magnetic properties of these samples, primarily the magnetic moments, relate to the observed transient behavior. An overview of the demagnetization time constants and magnetic moments determined in the preceding sections has been compiled in Figure 4.6. At first glance, the generally larger demagnetization time constants of Fe magnetic moments compared to Ni correlate with the larger values of Fe magnetic moments. When going into detail however, such a simple proportionality between demagnetization time constant and magnetic moment does not hold: While Ni in $Ni_{50}Fe_{50}$ has a much larger magnetic moment than pure Ni, ultrafast demagnetization of Ni in $Ni_{50}Fe_{50}$ is clearly accelerated compared to the pure element. So in the following, I will look at two recently proposed theoretical models for ultrafast demagnetization which take other materials parameters like Curie temperature and exchange interaction into account and check how well their predictions correspond to the experimental results.

Shortcomings of the Microscopic Three-Temperature Model

The first model is the so-called microscopic three-temperature model (M3TM) proposed by Koopmans et al. [27]. This model, which posits electron-phonon mediated spin-flip scattering as the main reason behind ultrafast demagnetization, was originally developed as an extension to the purely phenomenological three-temperature model, as already mentioned in Chapter 2.3.2. The M3TM neither explicitly includes nor excludes alloys in its description; in principle, alloys can be treated like pure materials, either by modeling the constituents separately or by using a composition dependent average over materials parameters like the magnetic moments of the constituents as input. Actually, Koopmans et al. themselves applied the M3TM to a TbFe alloy, finding that the experimentally observed demagnetization corresponded to the theoretical description [27].

Koopmans et al. propose that the characteristic time constants of demagnetization t_D of ferromagnetic materials are proportional to a simple figure of merit

$$\frac{1}{t_D} \propto \frac{T_C}{\mu_{\text{at}}}, \quad (4.3)$$

where T_C is the Curie temperature and μ_{at} the atomic magnetic moment, if several preconditions are fulfilled: Ambient temperature and pump fluence of the measurements done on the materials to be compared must be similar, in order to rule out a strong dependence of the observed effect on these parameters. Furthermore, the probability a_{SF} that an electron-phonon scattering event is accompanied by a spin-flip, the underlying reason for the proposed mechanism for ultrafast demagnetization, must be similar for the investigated materials.

So in order to find out whether the M3TM correctly predicts the observed variation of demagnetization time constants in the NiFe alloys investigated here, I will first check if the aforementioned preconditions are met. All time-resolved XMCD measurements were performed at room temperature and with similar pump fluences, see Chapter 4.1.2. The spin-flip probability a_{SF} can be expressed as

$$a_{\text{SF}} = pb^2, \quad (4.4)$$

where b^2 is a spin-mixing parameter and $1 < p < 10$ [27, 58]. b^2 can be calculated by ab initio theory [58]; the values for pure Ni and Fe are identical within 10 % of their respective values. No such calculations have been performed for NiFe alloys so far; however, since the spin-mixing parameters for the pure materials are already practically the same, it is justified to assume that b^2 for the alloys will lie in the same range. Thus, with $p = 4$ as assumed by Koopmans et al. for all ferromagnetic materials [27], a_{SF} is similar for Ni, Fe and their alloys. The trend in the demagnetization times for $\text{Ni}_{50}\text{Fe}_{50}$ and $\text{Ni}_{80}\text{Fe}_{20}$ as predicted by the M3TM figure of merit from equation 4.3 is then calculated, using magnetic moments from Table 4.1 and Curie temperatures of 631 K for pure Ni [89], 1043 K for pure Fe [89] and 800 K for both $\text{Ni}_{50}\text{Fe}_{50}$ and $\text{Ni}_{80}\text{Fe}_{20}$ [91]. The result is displayed in Figure 4.7.

It should be noted that the proportion constant in the figure of merit from equation 4.3 is adjusted such that the predicted values of the demagnetization times for pure Ni ($x=0$) and Fe ($x=1$) in Figure 4.7 coincide with the experimentally found time constants. In fact, the quantitative agreement between the M3TM predictions and the experimental values for pure Ni determined by Koopmans et al. is not very good. They find a theoretical demagnetization time constant of pure Ni of 210 fs compared to their experimental value of 160 fs [27], even though the M3TM contains several adjustable parameters to account for the cooling of the electron gas, the magnitude of demagnetization and heat diffusion to the sample substrate, among other things. Still, even with such optimistic scaling, the predicted trend does not correspond to my experimental results, as demonstrated by the deviation

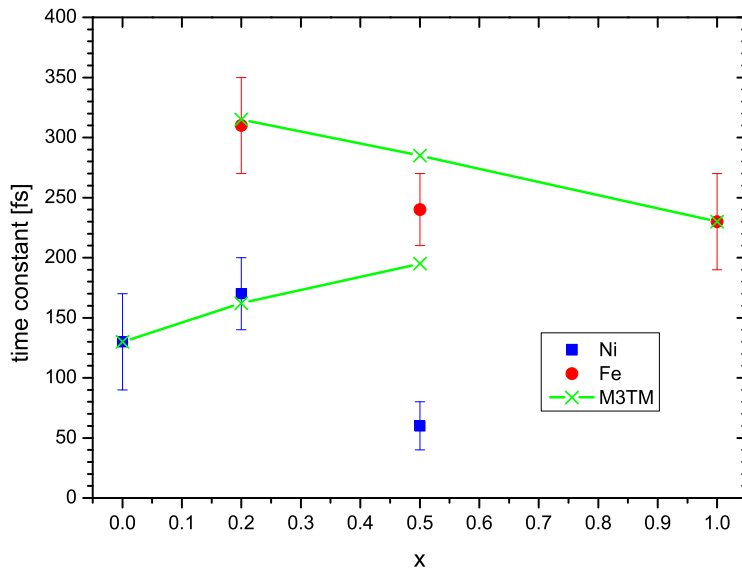


Figure 4.7: **Demagnetization time constants vs. Fe concentration x in $\text{Ni}_{1-x}\text{Fe}_x$.** Time constants of demagnetization t_D are plotted depending on the Fe content in the samples. t_D for pure Ni is taken from [24]. In the $\text{Ni}_{50}\text{Fe}_{50}$ and $\text{Ni}_{80}\text{Fe}_{20}$ alloys, blue squares refer to the values for the Ni sublattice, red circles to the values for the Fe sublattice. Shown as green lines are the trends predicted by the microscopic three-temperature model (M3TM) for the Ni and Fe sublattices.

of the time constants calculated with the M3TM from the experimental results in Figure 4.7. A smaller figure of merit for Ni in $\text{Ni}_{50}\text{Fe}_{50}$ compared to pure Ni would lead us to expect a *slower* demagnetization of Ni in the alloy – actually, the opposite is found experimentally. The M3TM does predict different time constants of demagnetization of the Ni and Fe sublattices in the alloys on account of their different magnetic moments, agreeing with the experimentally observed decoupling of the Ni and Fe magnetic moments. However, the M3TM misses part of the microscopic origin of the observed dynamic behavior and captures broad trends at best. Also, any predictions for *absolute* values of the demagnetization times is hampered by uncertainties surrounding the determination of the spin-flip probability a_{SF} , which is fundamental to the M3TM. Carva et al. [59] found smaller spin-flip probabilities in Ni than the authors of [58], and the resulting demagnetization rates were thus too small to make electron-phonon spin-flip scattering the dominant process behind ultrafast demagnetization, especially in thermalized electron distributions as assumed by the M3TM.

Multisublattice Model for Ultrafast Magnetization Dynamics

Since applying the M3TM to NiFe alloy samples leads to unsatisfactory results, I will next have a look at a theoretical model for laser-induced magnetization dynamics developed by Mentink et al. [46], which explicitly takes multiple sublattices in a ferro- or antiferromagnetic material, and the exchange interaction between these sublattices, into account. Since the figure of merit of the M3TM involves the Curie

temperature T_C (see equation 4.3), which is linked to the interatomic exchange interaction via

$$T_C = \frac{2\langle s \rangle^2 j_0}{3k_B}, \quad (4.5)$$

with $\langle s \rangle$ being the expectation value for the atomic spin moment and j_0 the exchange coupling constant [89], it can be said that the M3TM already includes exchange interaction, however indirectly. But in contrast to the multisublattice model, this exchange constant is an average over all sublattices in an alloy, because T_C is shared by all constituents. Furthermore, the theoretical framework by Mentink et al. [46] also allows for the investigated magnetic material to be out of thermal equilibrium, just as it is the case after laser excitation. Mentink et al. derive that magnetic sublattices with different magnetic moments show different transient behavior on the sub-ps timescale, as observed in the time-resolved XMCD measurements presented in Section 4.1.2. The authors propose that generally, laser-induced demagnetization time constants are determined by the interplay of the sublattice magnetic moments and the inter- and intrasublattice exchange interactions, and that the relative weight of these contributions is determined by the type of magnetic coupling (ferro- or antiferromagnetic) as well as by the temperature of the spin system.

Applying this model, in collaboration with J. Mentink, directly to the $\text{Ni}_{50}\text{Fe}_{50}$ and $\text{Ni}_{80}\text{Fe}_{20}$ samples investigated here, allows us to describe the changes in the characteristic time constants of demagnetization when going from the pure materials to alloys [94]. In the multisublattice model, the change in the demagnetization time constant in ferromagnetic materials upon alloying is given by a trade-off between the change in magnetic moment and the contributions of the intra- and intersublattice exchange interactions [94]. The ratio of the demagnetization time constant for pure Ni, $t_{\text{Ni}}(0)$, and the time constant for Ni in a $\text{Ni}_{1-x}\text{Fe}_x$ alloy, $t_{\text{Ni}}(x)$, can then be written as

$$\frac{t_{\text{Ni}}(0)}{t_{\text{Ni}}(x)} \approx \frac{\mu_{\text{Ni}}(0)}{\mu_{\text{Ni}}(x)} \left[(1-x) + x \frac{j_{\text{Ni-Fe}}}{j_{\text{Ni-Ni}}} \right], \quad (4.6)$$

with μ being the magnetic moment and j the exchange interaction.

Both the magnetic moments and the exchange interactions vary with stoichiometry. As seen in Table 4.1, the Ni magnetic moment in the NiFe alloys increases with increasing Fe content, while the Fe magnetic moment varies only slightly with changing Fe content. The intra- and intersublattice exchange interactions in Ni, Fe and their alloys are shown in Figure 4.8. It is known from *ab initio* calculations for $\text{Ni}_{80}\text{Fe}_{20}$ that the intrasublattice exchange interaction in the Fe sublattice $j_{\text{Fe-Fe}}$ is stronger than the exchange interaction between the Ni and Fe sublattices $j_{\text{Ni-Fe}}$, which is in turn stronger than the intrasublattice exchange interaction in the Ni sublattice $j_{\text{Ni-Ni}}$ [95]. Following the multisublattice model approach, we then arrive at a slightly slower demagnetization of the Ni sublattice in the alloy with less Fe content, $\text{Ni}_{80}\text{Fe}_{20}$, compared to pure Ni, in agreement with the experimental results.

No *ab initio* calculations for the exchange interactions in $\text{Ni}_{50}\text{Fe}_{50}$ are available so far. Therefore, the values for $j_{\text{Ni-Ni}}$ and $j_{\text{Fe-Fe}}$ for $\text{Ni}_{50}\text{Fe}_{50}$ plotted in Figure 4.8 have been extrapolated from the values for $\text{Ni}_{80}\text{Fe}_{20}$ and the pure element values, in accordance with a small, weakly decreasing value for $j_{\text{Ni-Ni}}$ when going from pure Ni to $\text{Ni}_{80}\text{Fe}_{20}$ [95], and a comparable or increased ratio of $j_{\text{Fe-Fe}}$ to $j_{\text{Ni-Ni}}$ for a higher Fe concentration predicted by the authors of [95]. According to equation 4.6, the contribution of the Ni-Fe intrasublattice exchange will increase with increased Fe content compared to $\text{Ni}_{80}\text{Fe}_{20}$, and the Ni sublattice in $\text{Ni}_{50}\text{Fe}_{50}$ is expected to demagnetize faster than observed for pure Ni. Using the experimentally found magnetic moments and time constants of demagnetization for $\text{Ni}_{50}\text{Fe}_{50}$, compare Tables 4.1 and 4.7, respectively, as input, the accelerated demagnetization can be

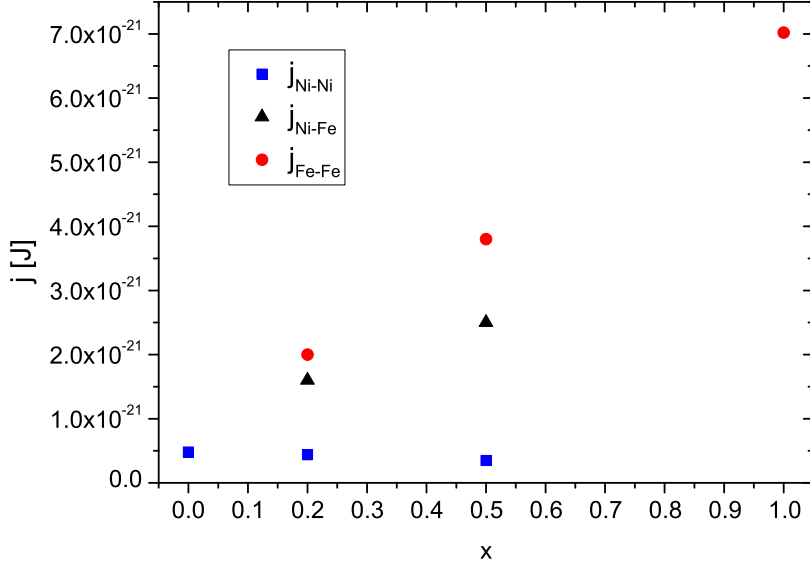


Figure 4.8: **Exchange interaction vs. Fe concentration x in $\text{Ni}_{1-x}\text{Fe}_x$.** *Inter- and intrasublattice exchange energies j are plotted depending on the Fe content x in the samples. j for pure Ni and $\text{Ni}_{80}\text{Fe}_{20}$ are taken from ab initio calculations [95], j for pure Fe is calculated from the Curie temperature of pure Fe [94]. The values for $\text{Ni}_{50}\text{Fe}_{50}$ are estimates based on trends predicted for increasing Fe concentration in NiFe alloys by [95], with the ratio between $j_{\text{Ni-Fe}}$ and $j_{\text{Ni-Ni}}$ adjusted to reproduce the experimentally observed demagnetization time constant of Ni in $\text{Ni}_{50}\text{Fe}_{50}$.*

reproduced for a sensible ratio of $j_{\text{Ni-Fe}}/j_{\text{Ni-Ni}} = 7:1$.

Making the same considerations based on the multisublattice model for the Fe magnetic moments in the alloys, only a slight increase in the demagnetization time constant compared to pure Fe is expected [94]. This is indeed observed in the experimental data, with a larger change for Fe in $\text{Ni}_{80}\text{Fe}_{20}$ than for Fe in $\text{Ni}_{50}\text{Fe}_{50}$ (compare Table 4.2).

In conclusion, the experimentally observed trends in the variation of the ultrafast magnetization dynamics in NiFe alloys can be explained much more accurately from a theoretical standpoint if both the magnetic moments of the Ni and Fe sublattices as well as the intersublattice exchange interaction are considered. The M3TM does not include intersublattice interaction and therefore fails to describe the magnetization dynamics in $\text{Ni}_{50}\text{Fe}_{50}$ (compare Figure 4.7). Only in the framework of the multisublattice model, by taking the Ni-Fe intersublattice exchange interaction into account, can the experimentally observed faster demagnetization of Ni in $\text{Ni}_{50}\text{Fe}_{50}$ be reproduced. These findings reinforce that the dynamic behavior of the constituents of ferromagnetic alloys is not determined by the atomic properties of the respective pure materials, but that the ultrafast magnetization dynamics can be tuned by varying the constituent magnetic moments and exchange interaction by adjusting the alloy composition.

4.2 Rare Earth Alloy $\text{Gd}_{60}\text{Tb}_{40}$

Rare earths are among the very first materials where laser-induced magnetization dynamics have been experimentally observed. Pioneering experiments by Vaterlaus et al. in the early 1990s [15, 16] used spin-polarized photoemission to estimate the time needed for thermal equilibration between the lattice and spin systems, the so-called spin-lattice relaxation time, in Gd after laser heating as 100 ± 80 ps. The high uncertainty of this time constant already shows that time-resolved measurements were then severely constrained by the limits of the experimental apparatus, in this case the pulse lengths of the pump and probe lasers of 10 ns and 60 ps, respectively [15]. Only recently it was found that both Gd and Tb also exhibit sub-ps magnetization dynamics: Time-resolved XMCD measurements by Wietstruk et al. [29] showed an ultrafast decrease of the magnetic moment after laser excitation in pure Gd and Tb, which happens with a characteristic time constant of about 750 fs for both elements. Additionally, a subsequent further decrease of the magnetic moment, taking place with time constants of 40 ps for pure Gd and 8 ps for pure Tb, was observed and confirmed to be connected to energy equilibration processes between the spin system and the lattice. The time constant of this second decrease of the magnetization was found to be determined by the strength of spin-lattice coupling – the faster demagnetization in Tb is linked to the non-spherical distribution of its 4f orbitals leading to a direct coupling between the atomic magnetic moment and the lattice, which is absent in Gd due to a spherical 4f distribution. Gd only shows a weaker valence electron mediated spin-lattice coupling (see [29] and references therein).

What I will show in the following chapter is that the time constants of demagnetization in rare earth metals can be manipulated by alloying. In a GdTb alloy, the Gd 4f magnetic moments are coupled to the neighboring Tb 4f magnetic moments by indirect exchange (RKKY) interaction and thus have enhanced coupling to the lattice via the neighboring Tb moments. Consequently, it can be expected that the Gd magnetic moments in GdTb alloy then decrease faster after laser excitation than in the case of pure Gd – if the indirect exchange coupling persists on the picosecond timescale. Finding changes in the time constants of demagnetization for Gd and Tb in $\text{Gd}_{60}\text{Tb}_{40}$ compared to the respective pure elements, I can estimate the timescale of indirect exchange interaction between the Gd and Tb moments in the alloy. Thereafter, I will look in more detail at the element-specific time constants of demagnetization corresponding to the sub-ps non-equilibrium demagnetization process and the subsequent quasi-equilibrium demagnetization occurring on timescales ranging from a few to several tens of picoseconds.

4.2.1 Sample Structure and Static Characterization

The 10 nm thick $\text{Gd}_{60}\text{Tb}_{40}$ sample was prepared by co-evaporation from Gd and Tb sources on a 500 nm thick Al foil for transmission geometry measurements². Y buffer and cap layers of 50 nm and 5 nm thickness, respectively, were used. Static absorption and XMCD spectra of the $\text{Gd}_{60}\text{Tb}_{40}$ sample, measured at the UE56/1-PGM beamline, are shown in Figure 4.9. The Gd and Tb atoms in the alloy show ferromagnetic alignment, which can also be seen from hysteresis measurements at the Gd and Tb M_5 -edges at 1186 eV and 1241 eV, respectively, displayed in Figure 4.10. The hysteresis measurements were performed at the UE56/1-ZPM beamline. Since the Curie temperature of $\text{Gd}_{60}\text{Tb}_{40}$ alloy is only about 270 K [96], all static and time-resolved measurements shown in this chapter were done at 82 K base

²The sample was prepared by A. Melnikov at FU Berlin.

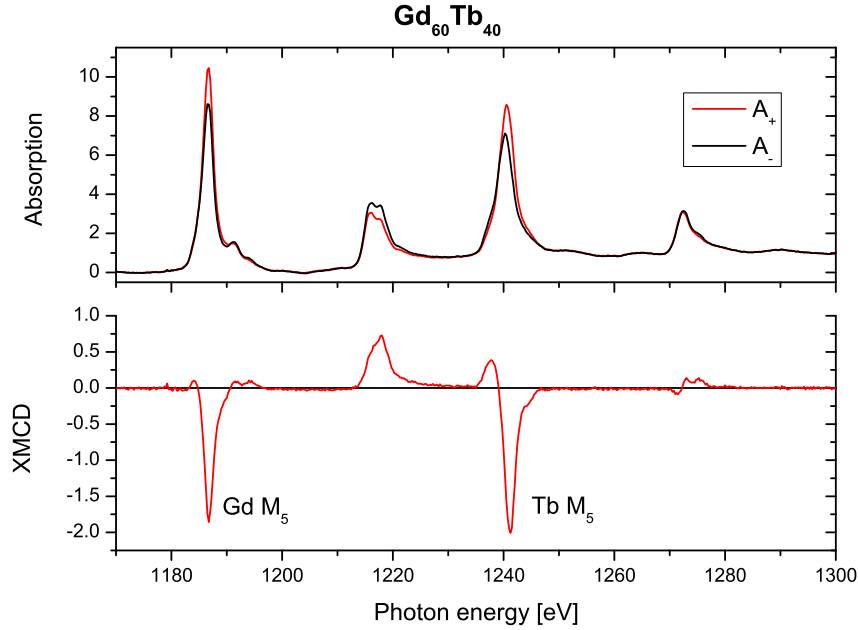


Figure 4.9: **Static absorption and XMCD spectra of $\text{Gd}_{60}\text{Tb}_{40}$ sample.** Absorption spectra at the Gd and Tb $M_{5,4}$ -edges for opposite orientations of an external magnetic field of 0.5 T along the x-ray propagation direction (A_+ and A_-) are shown in the upper panel. The absorption spectra are normalized to the continuum step. The resulting XMCD is plotted in the lower panel.

temperature. Because of the in-plane anisotropy of the sample, the angle between the sample normal and the incident x-ray direction was set to 35° . The hysteresis loops were measured with circularly polarized x-rays, while an external magnetic field cycled between ± 0.5 T, enough to saturate the sample, was applied along the x-ray propagation direction.

4.2.2 Accessing the Timescale of Indirect Exchange Interaction

Previous measurements of the ultrafast demagnetization of pure Gd and Tb [29] revealed important information regarding the relation between the observed two-step demagnetization process and spin-lattice coupling, as already mentioned in the introduction of this chapter. So, since the dynamic behavior in rare earths depends sensitively on the configuration of the 4f orbital moment leading to a difference in the strength of spin-lattice coupling between Gd and Tb, the question naturally follows whether spin-lattice coupling and thus dynamic behavior can be tuned. In the sample investigated here, the enhanced coupling to the lattice of the Gd 4f magnetic moments is realized by the admixture of Tb. In the following, I will present how the time-dependent behavior of the Gd magnetic moments in $\text{Gd}_{60}\text{Tb}_{40}$ alloy changes qualitatively compared to the pure element, using time- and element-resolved XMCD measurements.

The time-resolved XMCD data presented in this section was acquired at the UE56/1-

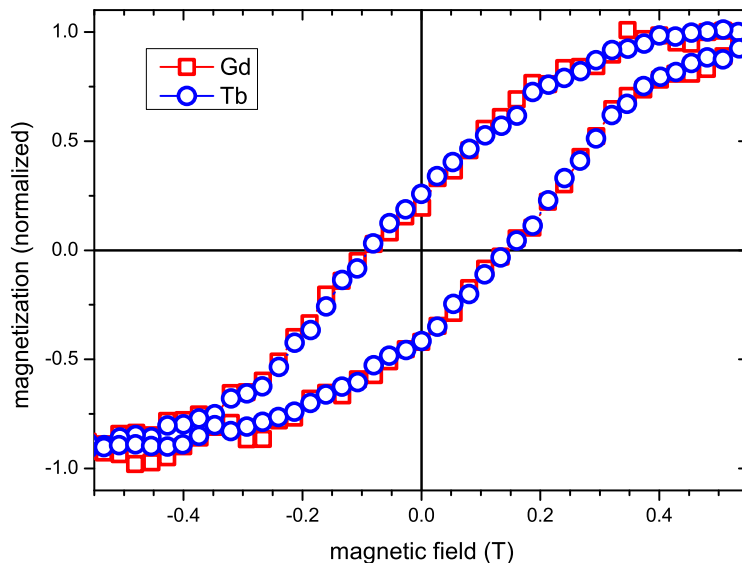


Figure 4.10: **Element-specific hystereses of Gd₆₀Tb₄₀.** *Hysteresis loops are plotted for Gd (red squares) and Tb (blue circles) in Gd₆₀Tb₄₀. The magnetization at maximum field is set to ±1. Both constituents show identical behavior and thus ferromagnetic alignment.*

ZPM beamline. The x-ray energy was set to the Gd M₅-edge at 1186 eV for measuring the Gd constituent in the Gd₆₀Tb₄₀ alloy, and to the Tb M₅-edge at 1241 eV for measuring the Tb constituent, probing the localized rare earth 4f magnetic moments. The pump fluence was 5.1 mJ/cm², as calculated with equation 4.1 from the following parameters: repetition rate 1.5 kHz and pump power 60 mW, resulting in a power per pulse of 40 μJ, and a pump spot diameter of 1 mm. Like the static measurements shown in Section 4.2.1, the time-resolved measurements were performed at 82 K base temperature. The sample was rotated to an angle of 35° between the sample normal and the x-ray propagation direction, while an external magnetic field of ±0.5 T was applied along the x-ray propagation direction.

Figure 4.11 shows the temporal evolution of the Gd and Tb magnetic moments in Gd₆₀Tb₄₀. The magnetic moments of both constituents decay to a nearly constant value within the first 4 ps after laser excitation. The final value reached for both Gd and Tb in Gd₆₀Tb₄₀ is similar; both curves overlap within the scatter of the datapoints. The slightly different transient behavior of both constituents in the first 4 ps after laser excitation, displayed in more detail in the inset of Figure 4.11, suggests a somewhat faster demagnetization for Gd in Gd₆₀Tb₄₀.

There occurs no second decay of the Gd magnetic moment as seen for pure Gd [29]. The fact that Gd in Gd₆₀Tb₄₀ qualitatively behaves like Tb shows that by alloying, an additional channel for the transfer of angular momentum from the Gd 4f magnetic moment to the lattice has been opened via the neighboring Tb 4f magnetic moments and their strong direct coupling to the lattice, leading to a faster demagnetization of Gd in the alloy. For this channel to be active, the indirect exchange coupling of the Gd 4f magnetic moments to the Tb 4f moments via the 5d valence

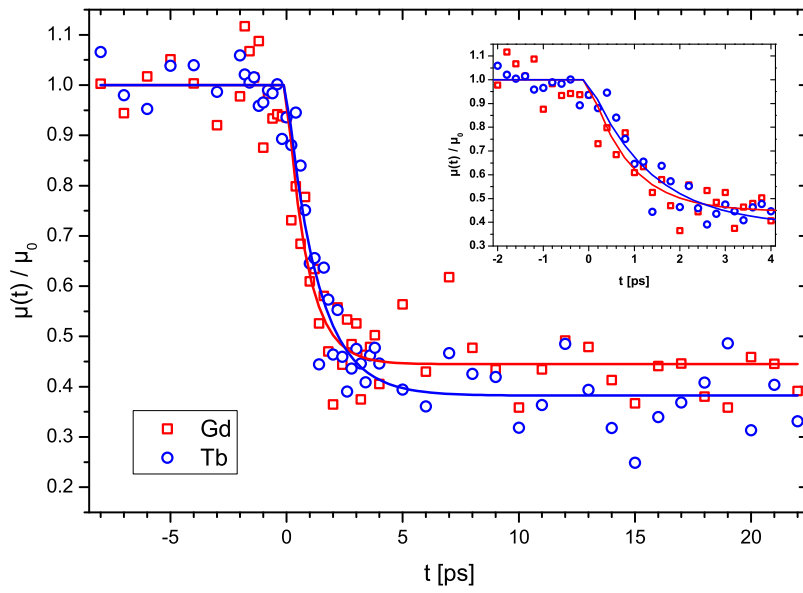


Figure 4.11: **Time-resolved XMCD measurement of $\text{Gd}_{60}\text{Tb}_{40}$.** The evolution of the magnetic moment μ depending on the pump-probe delay t is plotted for Gd (red squares) and Tb (blue circles) in $\text{Gd}_{60}\text{Tb}_{40}$. The red and blue lines correspond to single exponential fits to the Gd and Tb data as described in the text. μ is normalized to the average value μ_0 for the unexcited sample. These delay scans were taken with a pump fluence of 5.1 mJ/cm^2 .

band electrons must be present. This way, the timescale of indirect exchange coupling can be estimated to be shorter than the timescale of the dissipation of the magnetic moment of the Tb constituent by spin-lattice coupling, i.e. the second step in the ultrafast demagnetization.

In order to obtain a more quantitative picture about the observed dynamics, the time-resolved XMCD curves of the constituents of $\text{Gd}_{60}\text{Tb}_{40}$ were fitted with a single exponential decay,

$$f(t) = S(t) \cdot [A - B(1 - e^{-\frac{t}{t_D}})], \quad (4.7)$$

where $S(t)$ refers to a step function, A to the XMCD value at negative delays, B to the amplitude of the exponential decay and t_D to the characteristic time constant of demagnetization. No convolution with the experimental time resolution of 130 fs was performed since the demagnetization of $\text{Gd}_{60}\text{Tb}_{40}$ was expected and indeed found to occur on the same timescale as for pure rare earths [29], much slower than the demagnetization of transition metals and their alloys (see Chapter 4.1), and thus not in the same range as the experimental resolution. Also, it was not necessary to correct the data for possible drifts in the temporal pump-probe overlap ($t=0$). Any temporal changes of the pump-probe overlap from day to day due to variations in temperature and air pressure in the laser path were known to be smaller than or on the order of the smallest pump-probe delay step of 200 fs employed here; this was determined from pump-probe measurements on transition metals (see Chapters 4.1 and 5). In any case, delay scans at the Gd and Tb M_5 -edges were measured alternately, so that temporal drifts would affect both in the same way.

This dataset does not allow for a determination of the time constant of a possible second, slower decay of the Gd and Tb magnetic moments, as observed in the pure elements [29]. A fit to the data with a double exponential decay instead of a single exponential decay shows no dependence of the observed dynamics on a second time constant. Indeed, the magnitude of demagnetization at $t=5$ ps is equal to that at $t=20$ ps; no further decay is observed.

The single exponential fit then returns demagnetization time constants of 880 ± 290 fs for Gd and 1.3 ± 0.3 ps for Tb in $\text{Gd}_{60}\text{Tb}_{40}$. These time constants seem to be somewhat larger than the demagnetization time constants for pure Gd, 750 ± 250 fs, and pure Tb, 740 ± 250 fs, measured in the same fluence range but at a different base temperature of 140 K [29]. However, the size of the error bars and the similar yet not quite equal experimental conditions do not allow for determining a particular trend in the time constants. It has been found that the time constants of the two steps in the demagnetization in pure Tb and their relative magnitude sensitively depend on the pump laser fluence [32]. Consequently, the fluence dependence of the observed dynamics in $\text{Gd}_{60}\text{Tb}_{40}$ alloy will be addressed in the next section.

4.2.3 Non-equilibrium and Quasi-equilibrium Magnetization Dynamics

In the preceding section, I could determine an upper limit for the timescale of the indirect exchange interaction, namely the time constant of the second decay of the Tb magnetic moment in $\text{Gd}_{60}\text{Tb}_{40}$. This second, slower demagnetization is connected to the quasi-equilibrium magnetization dynamics assigned to the strength of spin-lattice coupling. However, no value for this timeconstant could be derived from the time-resolved XMCD measurements performed with 5.1 mJ/cm^2 pump fluence. This is most likely due to a strong fluence dependence of both the time constant and the relative magnitude of the two steps in the demagnetization process in rare earths, as previously seen in pure Tb [32]: With increasing fluence, the magnitude

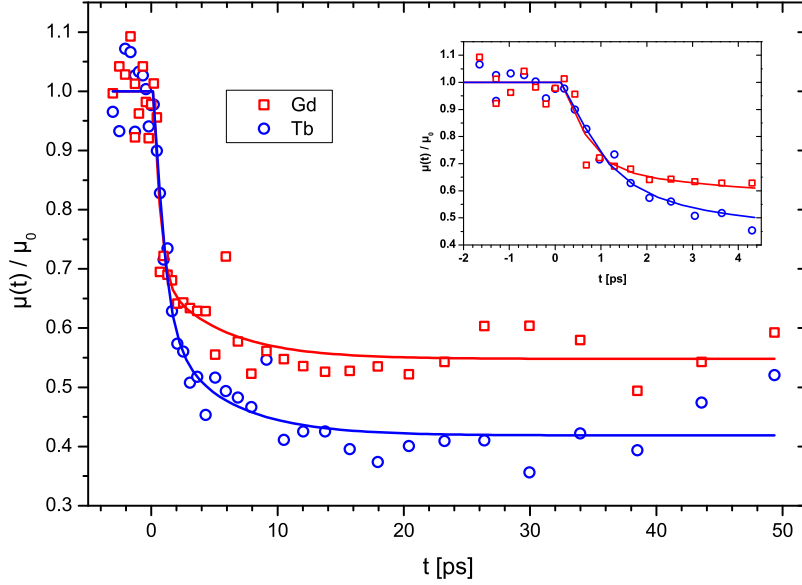


Figure 4.12: **Time-resolved XMCD measurement of $Gd_{60}Tb_{40}$ at reduced fluence.** The evolution of the magnetic moment μ depending on the pump-probe delay t is plotted for Gd (red squares) and Tb (blue circles) in $Gd_{60}Tb_{40}$. The red and blue lines correspond to double exponential fits to the Gd and Tb data as described in the text. μ is normalized to the average value μ_0 for the unexcited sample. These delay scans were taken with a pump fluence of 3.4 mJ/cm^2 .

of the first, non-equilibrium decay increases, making it difficult to determine the time constant of the second, quasi-equilibrium decay, or to observe it at all. Therefore, additional time-resolved XMCD measurements were made with reduced pump fluence.

The measurements shown here were performed with the same x-ray parameters, base temperature, magnetic field and angle as those shown in the previous section. The pump fluence was reduced to 3.4 mJ/cm^2 , as derived from equation 4.1 with 3 kHz repetition rate and 160 mW pump power, resulting in $53 \text{ } \mu\text{J}$ power per pulse, and 1.4 mm pump spot diameter.

The time-resolved XMCD measurements at lower pump fluence, displayed in Figure 4.12, in fact show a transient behavior different to those taken at higher fluence (compare Figure 4.11). The final magnitude of demagnetization is reached in two steps; the faster decay, which can be seen in more detail in the inset, comprises only half of the total magnitude of demagnetization.

Now, for obtaining the time constants of demagnetization for the fast, non-equilibrium decay, designated t_F , and for the slow, quasi-equilibrium decay, t_S , the Gd and Tb pump-probe delay scans were fitted with a double exponential decay,

$$f(t) = S(t) \cdot [A - B(1 - e^{-\frac{t}{t_F}}) - C(1 - e^{-\frac{t}{t_S}})], \quad (4.8)$$

where $S(t)$ refers to a step function, A to the XMCD value at negative delays and B and C to the amplitudes of the fast and slow exponential decay, respectively.

sample		pump fluence [mJ/cm ²]	t _F [ps]	t _S [ps]
Gd		3-5	0.76 ± 0.25	40 ± 10
Gd ₆₀ Tb ₄₀	Gd	5.1	0.88 ± 0.29	–
	Tb	5.1	1.3 ± 0.3	–
	Gd	3.4	0.45 ± 0.24	5.0 ± 2.9
	Tb	3.4	0.81 ± 0.36	5.0 ± 2.9
Tb		3-5	0.74 ± 0.25	8 ± 3

Table 4.3: **Demagnetization time constants vs. stoichiometry in rare earths.** *The non-equilibrium and quasi-equilibrium time constants, t_F and t_S, depending on the pump fluence, are listed for Gd₆₀Tb₄₀ as well as for pure Gd and Tb. Pure Gd and Tb time constants are taken from [29]; the exact pump fluence could not be determined from [29] as only a range of 3-5 mJ/cm² is given by the authors.*

Employing the same arguments as for the single exponential fit in Chapter 4.2.2, neither a correction of a possible drift in the temporal pump-probe overlap nor a convolution with the experimental time resolution of 130 fs is necessary. For the fast decay, the time constant for Gd is 450 ± 240 fs, while the time constant for Tb is slightly larger at 810 ± 360 fs. When it comes to the slow decay, best fit results are achieved for a common time constant for Gd and Tb, 5.0 ± 2.9 ps.

An overview of all time constants for Gd₆₀Tb₄₀, depending on the pump fluence, is given in Table 4.3. Regarding the non-equilibrium demagnetization, Gd uniformly shows a faster time constant than Tb in Gd₆₀Tb₄₀. For the origin of the non-equilibrium demagnetization in pure Gd and Tb, hot electron enhanced spin-lattice coupling was proposed by Wietstruk et al. [29]. It is not clear how this mechanism would influence the non-equilibrium dynamics in GdTb alloy, if at all, since already pure Gd and Tb exhibit practically identical time constants for the fast magnetization decay. Other proposed mechanism for ultrafast demagnetization, such as the microscopic three-temperature model [27] and superdiffusive spin transport [4], were found not to apply to the rare earth case, due to the large magnetic moments and their localized nature [29].

A clearer picture emerges for the quasi-equilibrium demagnetization: The time constant of the second decay t_S of Gd in the alloy is definitely smaller than for pure Gd. This confirms the enhancement of the coupling between the Gd 4f magnetic moments and the lattice in Gd₆₀Tb₄₀. The value of t_S in the alloy is slightly smaller but in the same range as for pure Tb, indicating that the quasi-equilibrium demagnetization for both constituents is dominated by the strong spin-lattice coupling of the Tb 4f magnetic moments. Consequently, the indirect exchange interaction binding the Gd 4f magnetic moments to the Tb 4f magnetic moments via the 5d electrons must be active on a timescale of a few picoseconds.

One remaining question is the nature of the offset in the magnitude of demagnetization between Gd and Tb in Gd₆₀Tb₄₀ which appears in the measurements performed with reduced fluence. Care was taken to exclude any systematic errors that could be responsible for such an offset. The two curves do return to a common value at about 120 ps after laser excitation, as shown in the pump-probe delay scans in Figure 4.13, which were measured in low-alpha mode (see Chapter 3) with a time resolution of about 10 ps. One possible origin for this offset would be that the spin angular momentum of Gd in the alloy does not fully dissipate to the lattice via the coupling to the neighboring Tb atoms, but that the weak valence electron mediated spin-lattice coupling known from pure Gd is still active. This process takes place

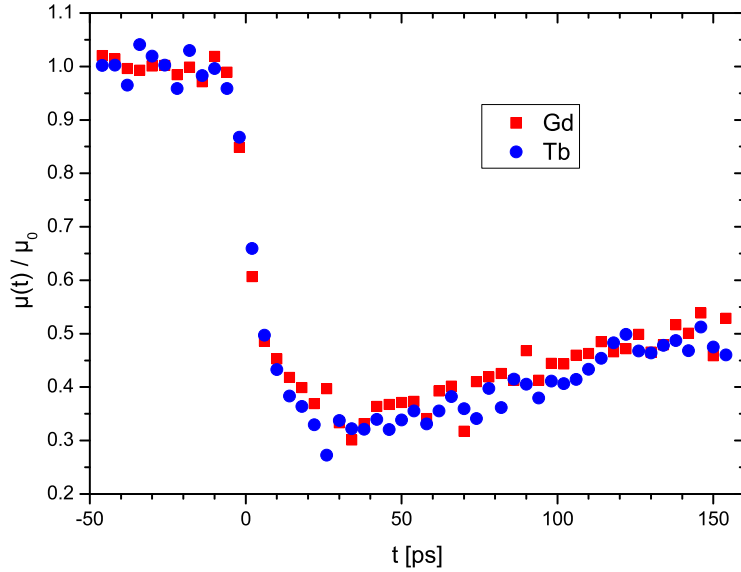


Figure 4.13: **Low-alpha mode measurement of $\text{Gd}_{60}\text{Tb}_{40}$.** *The evolution of the magnetic moment μ depending on the pump-probe delay t is plotted for Gd (red squares) and Tb (blue circles) in $\text{Gd}_{60}\text{Tb}_{40}$, as measured in low-alpha mode. μ is normalized to the average value μ_0 for the unexcited sample.*

with a time constant of about 40 ps in pure Gd, in the same timeframe in which the offset between Gd and Tb is present in $\text{Gd}_{60}\text{Tb}_{40}$.

The example of $\text{Gd}_{60}\text{Tb}_{40}$ alloy shows that, like for the NiFe alloys presented in Chapter 4.1, the time-dependent behavior of the magnetization can be tuned through the sample's microscopic properties. So far, uncertainties remain regarding the behavior of the constituents of $\text{Gd}_{60}\text{Tb}_{40}$ on the fast, non-equilibrium part of the magnetization decay due to the lack of a satisfying microscopic description. However, the finding of a faster quasi-equilibrium demagnetization of Gd in $\text{Gd}_{60}\text{Tb}_{40}$ compared to the pure material due to enhanced spin-lattice coupling confirms that ultrafast demagnetization is determined by both an interplay of the different degrees of freedom – electrons, spins and the lattice – and the exchange coupling of the constituents in a ferromagnetic alloy.

Chapter 5

Influence of Hot Electron Transport on Ultrafast Demagnetization in Ferromagnetic Multilayers

Almost every description of the ultrafast demagnetization process, phenomenological or microscopic, is based on different energy reservoirs or heat baths and the exchange of energy and angular momentum between them. This exchange of energy and angular momentum is thought to happen via scattering processes, between electrons, phonons and magnons [27, 28, 60]. However, generally spin transport or spin dependent transport effects also play an important role in magnetization dynamics. Examples for this are numerous and include the switching of magnetic domains by spin-polarized current [97], spin current induced propagation of domain walls [98], spin torque induced gyration of magnetic vortices [99], the spin Hall effect [100, 101] as well as the spin Seebeck effect [102]. This list shows the importance of transport effects and evokes the question whether they are relevant in ultrafast magnetization dynamics as well.

In normal metals, transport of electrons excited by pulsed laser irradiation in the optical range is already well known and extensively described [103, 104]. Directly after a femtosecond laser pulse excites the sample and before thermalization of the excited electrons occurs, ballistic transport of nonequilibrium electrons out of the excited sample volume with velocities on the order of 10^6 m/s takes place. Then, when the excited electrons have thermalized, still at elevated temperature compared to the lattice, diffusion of hot electrons occurs with velocities on the order of 10^4 m/s [105]. All these processes take place in the first few hundreds of femtoseconds after laser irradiation, in the same range of time where ultrafast demagnetization has been observed. In fact, recently Battiato et al. [4] developed a model describing spin-dependent electron transport from the ballistic to the diffusive range in ferromagnetic metals, the so-called superdiffusive spin transport, and the process was proposed to significantly contribute to ultrafast demagnetization. The aim of this chapter is to test this and other microscopic models for the underlying origin of ultrafast demagnetization.

The following chapter shows time-resolved XMCD measurements of multilayer samples. Inducing ultrafast demagnetization in an indirect way, through the injection of laser-excited hot electrons into a ferromagnetic layer, represents a novel way of

studying magnetization dynamics. In the sample geometry conventionally used for time-resolved magnetic measurements, be it MOKE or photoemission, the ferromagnetic sample is uncapped or capped only by a protective layer far thinner than the pump laser penetration depth. Direct interaction between the pump laser photons and the electron spins in the excited material, which has been proposed for the explanation of ultrafast demagnetization [47, 52], can thus never be excluded as a possible mechanism causing ultrafast demagnetization. A longstanding point of contention regarding this kind of microscopic model has been the number of photons needed to induce a demagnetization as large as experimentally observed [48, 49]. So, in an experiment testing the different microscopic models proposed for ultrafast demagnetization, it would be desirable to exclude direct excitation of the ferromagnetic layer by the pump pulse as much as possible, by lowering the number of photons able to reach the ferromagnetic layer significantly. This is achieved by capping a ferromagnetic layer with a thick nonmagnetic film. For looking at transport induced effects in the buried ferromagnetic layer, a cap layer material known for optimal transport properties of laser excited electrons is used, as detailed in Chapter 5.1. Since this sample geometry involves making the top layer at least as thick as the penetration depth of the optical pump laser, observing the magnetization dynamics in the buried ferromagnetic layer is only possible with XMCD spectroscopy in transmission geometry. Here, the probe x-rays can reach the buried ferromagnetic layer, and, by tuning the x-ray energy to the element-specific absorption edges, the contribution from the unpumped layer can be discerned.

In this chapter, I will first outline the sample structure and the absorption profile of the pump laser in this particular geometry. Then, time-resolved XMCD measurements of the ferromagnetic layer in the samples under investigation will be shown, and the characteristic time constants of demagnetization derived. After that, the experimental results will be discussed with regards to whether the experimentally observed effects are in accordance with microscopic models proposed for the underlying origin of ultrafast demagnetization.

I will show that, in a sample designed in such a way that 90 % of the incident pump laser energy will be absorbed in a 30 nm thick gold cap layer, ultrafast demagnetization can indeed be induced in a buried ferromagnetic Ni layer. Comparing the experimental results with theory will demonstrate that superdiffusive spin transport [4] explains the effect. My finding that ultrafast demagnetization of the buried layer can indeed be triggered by hot electrons excited in the top layer illustrates the importance of taking transport effects into account in a microscopic description of the ultrafast demagnetization process.

5.1 Sample Structure and Pumping Conditions

In order to have a direct comparison between the magnetization dynamics induced by the injection of hot electrons into the ferromagnetic Ni layer by pumping the Au layer on the one hand, and, on the other hand, those seen in the standard pump-probe sample geometry, where the pump laser pulse is mainly absorbed in the ferromagnetic layer, two samples were prepared by magnetron sputtering.

The reference sample consists of a 20 nm thick Ni film deposited on a 500 nm thick, freestanding Al foil, whereby Pt buffer and cap layers of 2.5 nm thickness each were used. This sample will be called "Ni reference" in the following. As for the sample intended for the demonstration of demagnetization through hot electron injection, a 15 nm thick Ni layer was capped by a 30 nm thick Au layer. Like for the Ni reference sample, a 500 nm thick Al substrate and 2.5 nm thick Pt buffer layer were used. This sample will be referred to as "Au/Ni" in the following.

Gold was chosen for the thick cap layer designed to absorb the pump pulse since its

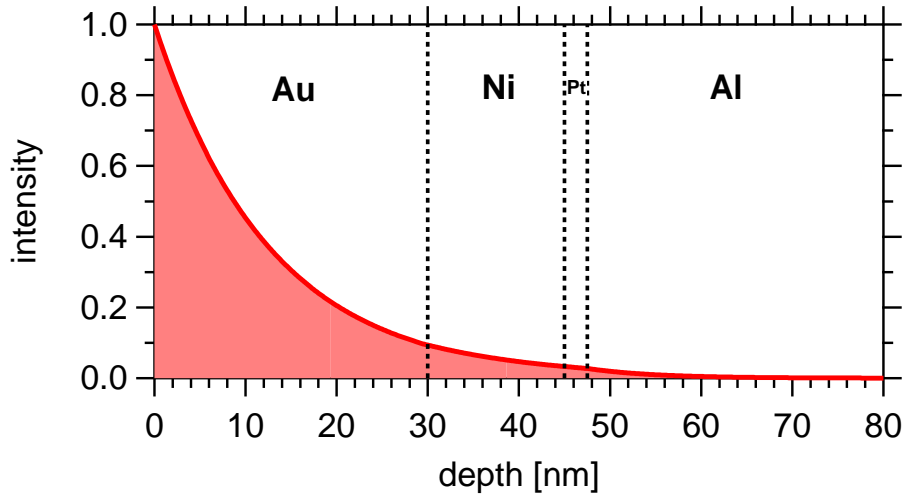


Figure 5.1: **Pump laser absorption in Au/Ni sample.** A calculation of the absorbed intensity of the pump laser pulse with 780 nm wavelength is shown depending on the distance from the sample surface. The different layers of the sample are indicated by dotted lines.

transient behavior after optical laser irradiation has been studied extensively with time-resolved reflectivity measurements [11, 14, 105, 106] as well as time-resolved photoemission spectroscopy [12, 13]. A long mean free path for ballistic electrons of about 100 nm has been found in Au [105]. Also, the inelastic mean free path of electrons excited at energies of up to 1.5 eV was calculated to be on the order of several tens of nm [62]. This means that at the pump wavelength of 780 nm used here, electrons excited in the 30 nm thick Au cap layer can indeed transfer into the Ni layer. A thickness of 30 nm for this Au layer was used since it represents a thickness where the pump laser is almost completely absorbed in the cap layer, as depicted in Figure 5.1, but the probe x-rays transmitted through the sample, which already have a quite low flux in Femtoslicing mode, are not reduced much further in intensity. As the calculated absorption profile for the Au/Ni sample in Figure 5.1 shows, 90 % of the pump laser energy is already absorbed in the Au cap layer, with 5 % reaching the Ni layer. In contrast, the majority of the pump laser energy (55 %) in the Ni reference sample is absorbed in the Ni layer; see Figure 5.2 for the calculated absorption profile. In the calculation of the absorption profiles, the following extinction coefficients, i.e. the imaginary parts of the complex index of refraction at 780 nm wavelength, were used: 4.9123 for Au, 4.3240 for Ni, 4.8627 for Pt and 8.60 for Al, as taken from [107].

Finally, it should be noted that the ferromagnetic Ni layers in both samples show in-plane anisotropy.

5.2 Ultrafast Demagnetization of the Buried Ni Layer in Au/Ni

For the time-resolved XMCD measurements, the x-ray energy was set to the Ni L_3 -edge at 853 eV. All measurements shown in this chapter were performed at room temperature. Because of the in-plane anisotropy of the Ni layers in both samples, they were set to an angle of 35° between the sample normal and the incident x-ray

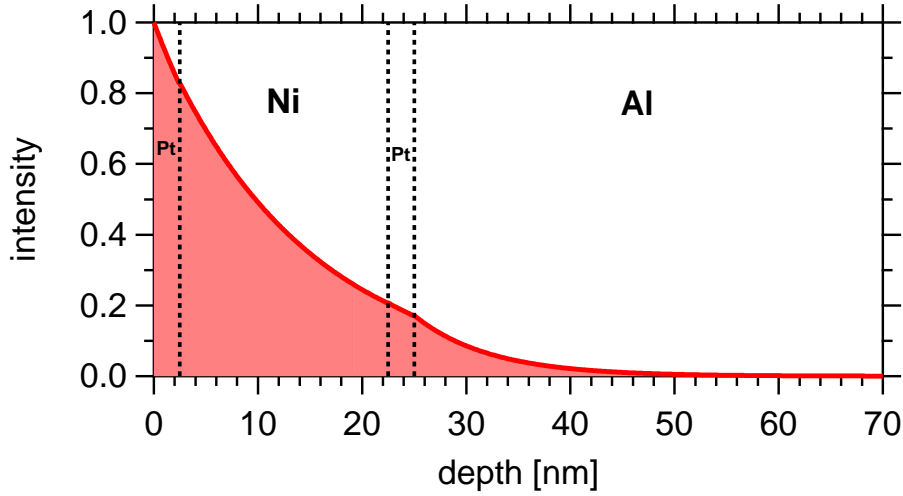


Figure 5.2: **Pump laser absorption in Ni reference sample.** *A calculation of the absorbed intensity of the pump laser pulse with 780 nm wavelength is shown depending on the distance from the sample surface. The different layers of the sample are indicated by dotted lines.*

direction. XMCD was measured with circularly polarized x-rays while an external magnetic field of ± 0.2 T was applied along the x-ray propagation direction. The pump laser repetition rate was 3 kHz, and the diameter of the pump laser spot on the sample 0.8 mm for all measurements. The pump power was not the same for the Au/Ni and Ni reference samples since the different reflectivities of the cap layers, Au and Pt, respectively, have to be taken into account. For the p-polarized pump pulses with 780 nm wavelength under an angle of incidence of 35° employed here, the reflectivity of Au on the Au/Ni sample was measured to be 0.880, while that of Pt on the Ni reference is much lower at 0.518. In order to compensate, the pump power was adjusted so that the same degree of demagnetization was achieved in the Au/Ni and the Ni reference sample. For Au/Ni, the pump laser power was set to 500 mW, resulting in a power per pulse of $167 \mu\text{J}$ and thus a fluence of $33.2 \text{ mJ}/\text{cm}^2$ as calculated with equation 4.1. The Ni reference was measured with a pump power of 150 mW, giving a power per pulse of $50 \mu\text{J}$ and fluence of $9.9 \text{ mJ}/\text{cm}^2$. This pump configuration will in the following be termed "high fluence". A second set of measurements was also done at reduced fluence: Au/Ni was measured with 350 mW pump power, resulting in a power per pulse of $117 \mu\text{J}$ and fluence of $23.3 \text{ mJ}/\text{cm}^2$, while the Ni reference measurements were taken with 100 mW pump power and thus $33 \mu\text{J}$ power per pulse and $6.6 \text{ mJ}/\text{cm}^2$ fluence.

In order to counteract drifts in the measurement parameters for Au/Ni and the Ni reference, the two samples were alternated every few hours. This was, however, not sufficient to prevent drifts in the pump beam path due to changes in ambient temperature and air pressure over the day from influencing the measured delay scans. Consequently, the drift in temporal pump-probe overlap (time zero) was determined by fitting the Ni reference data acquired during a measurement cycle lasting a few hours, before the sample was switched to Au/Ni, and then shifting the time axis of the Ni reference delay scans accordingly before averaging. Time zero for the Au/Ni data was found by a linear interpolation of the values for time zero determined from the Ni reference data recorded before and after the Au/Ni delay scans in question.

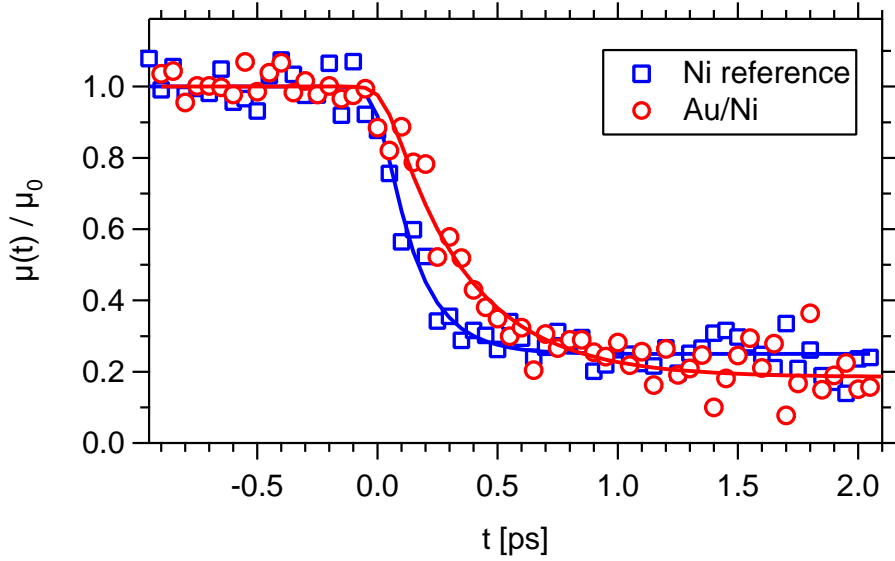


Figure 5.3: **Ultrafast demagnetization of Au/Ni at high pump fluence.** Shown is the evolution of the Ni magnetic moment μ depending on the pump-probe delay t in the Au/Ni sample (red circles) compared to the Ni reference sample (blue squares). The red and blue lines correspond to fits to the Au/Ni and Ni reference data as described in the text. μ is normalized to the average value μ_0 for the unexcited sample. The pump fluence was set to 33.2 mJ/cm^2 for Au/Ni and 9.9 mJ/cm^2 for the Ni reference, leading to a demagnetization of about 75 % for both cases.

By following this procedure, similar to what was used in Chapter 4.1.2, the characteristic demagnetization time constant for pure Ni could be reproduced, as will be discussed below.

The evolution of the magnetic moment in the buried Ni layer in Au/Ni after laser irradiation is displayed in Figure 5.3 in direct comparison to the ultrafast demagnetization of the Ni reference sample. Shown here is the high fluence scenario, where pumping the Au/Ni sample with a fluence of 33.2 mJ/cm^2 and the Ni reference with 9.9 mJ/cm^2 leads to a demagnetization of about 75 % in both cases. It is immediately obvious that the resulting demagnetization in Au/Ni happens on the sub-ps timescale, as in the Ni reference sample, where the ferromagnetic layer is excited directly by the pump laser. In both cases, the Ni magnetic moment decreases to its final value within the first picosecond. A recovery is not observed in the measured delay range, and happens only on longer timescales of several tens to hundreds of picoseconds.

Looking in more detail at the Au/Ni and Ni reference pump-probe delay scans in Figure 5.3, it can be seen that the demagnetization in Au/Ni happens more slowly than in the Ni reference sample. In order to derive the characteristic time constants of demagnetization, both curves were fitted with a single exponential decay convoluted with the experimental time resolution of 130 fs, as described by equation 4.2. The fit gives time constants of $330 \pm 40 \text{ fs}$ for Au/Ni compared to $140 \pm 10 \text{ fs}$ for the Ni reference. The latter time constant reproduces the literature value for the demagnetization of pure Ni of $130 \pm 40 \text{ fs}$ [24] within the error bars, showing that the correction of the drift in time zero outlined above can reliably remove temporal broadening of the measured pump-probe delay scans due to changes in the pump

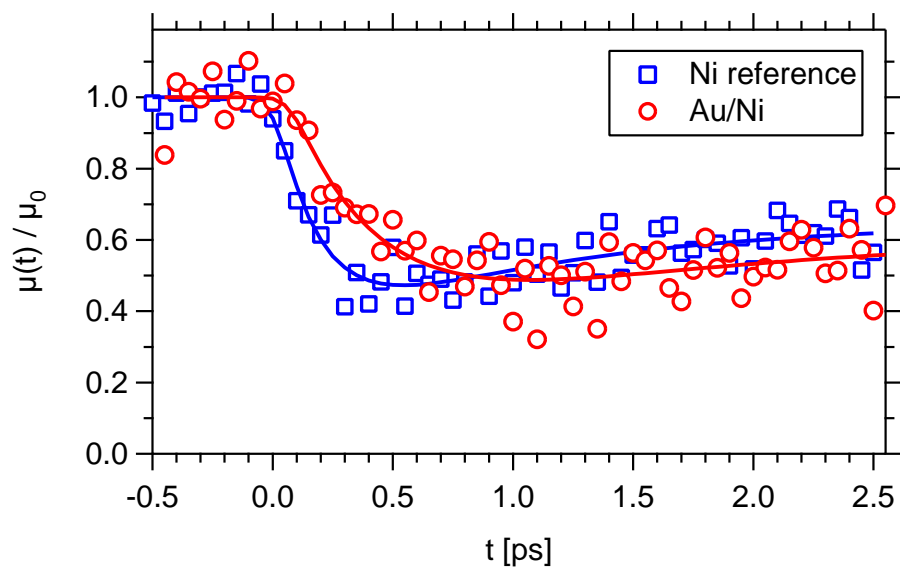


Figure 5.4: **Ultrafast demagnetization of Au/Ni at reduced pump fluence.** Ultrafast demagnetization of Au/Ni at high pump fluence. Shown is the evolution of the Ni magnetic moment μ depending on the pump-probe delay t in the Au/Ni sample (red circles) compared to the Ni reference sample (blue squares). The red and blue lines correspond to fits to the Au/Ni and Ni reference data as described in the text. μ is normalized to the average value μ_0 for the unexcited sample. The pump fluence was set to 23.3 mJ/cm^2 for Au/Ni and 6.6 mJ/cm^2 for the Ni reference, leading to a demagnetization of about 50 % for both cases.

path length.

There is no measurable delay in the onset of demagnetization between the Au/Ni and Ni reference samples. The single exponential fit of the Au/Ni does return a time of 25 ± 30 fs for the onset of demagnetization, but since the error bars are large enough to include time zero, no reliable statement can be made. This is, however, concordant with the fact that hot electron transport directly after laser irradiation takes place in the ballistic regime, with transport velocities close to the Fermi velocity, on the order of 10^6 m/s [105, 108]. Purely ballistic transport would lead to a travel time of about 30 fs for hot electrons that traverse the 30 nm thick Au layer; this value is below both the experimental time resolution of 130 fs and the step size of 50 fs used in the pump-probe delay scans shown here and thus difficult to resolve under the present experimental conditions.

The same measurement comparing the ultrafast demagnetization of Au/Ni to the Ni reference was also performed at reduced fluence and is shown in Figure 5.4. Here, the pump fluence used for Au/Ni was 23.3 mJ/cm², while the Ni reference was pumped with a fluence of 6.6 mJ/cm². This resulted in a demagnetization of about 50 % for both samples. As in the high fluence scenario, the decay of the Ni magnetic moments takes place on a sub-ps timescale, with Au/Ni being somewhat slower than the Ni reference. In contrast to the high fluence measurements, a slight recovery of the magnetic moments can already be observed within the measured delay range of 2.5 ps. For this reason, a double exponential function convoluted with the experimental time resolution of 130 fs, was used to fit the data. This fit function is written as

$$f(t) = S(t) \cdot G(t) * [A - B(1 - e^{-\frac{t}{t_D}}) - C(1 - e^{-\frac{t}{t_R}})], \quad (5.1)$$

where $S(t)$ refers to a step function, $G(t)$ to the Gaussian representing the experimental time resolution, A to the XMCD value at negative delays and B and C to the amplitudes of the ultrafast decay and the recovery, respectively, while t_D and t_R stand for the time constants of decay and recovery. This gives time constants of demagnetization t_D of 400 ± 160 fs for Au/Ni and 185 ± 30 fs for the Ni reference. The time constant of the recovery of the magnetic moment t_R was fixed to 1 ps for both samples. The time constant of the recovery was fixed to a certain value because leaving it as a free parameter did not give sufficient certainty for determining this time constant at all. Instead, fits were performed on the Ni reference data with fixed, reasonable values for t_R ranging from 0.5 ps to 3 ps, giving smallest χ^2 for a value of 1 ps. Also, a delay in the onset of demagnetization in Au/Ni compared to the Ni reference of 70 ± 40 fs was determined.

When one compares the time constants of demagnetization determined in the high and reduced pump fluence scenarios, listed in Table 5.1 for convenience, the difference between the Ni reference and the buried Ni layer in Au/Ni is always there, with Au/Ni showing a longer time constant. The respective time constants for Au/Ni and the Ni reference are in the same range for both fluence scenarios; while they seem to be a bit larger for reduced fluence, the statistics in the reduced fluence case are not good enough to make a definitive statement. The same argument holds for the delay in the onset of demagnetization. If there is a fluence dependence, it is not strong. The very similar behavior for high and reduced pump fluences shows that the underlying process behind the demagnetization of the buried Ni layer in Au/Ni must be the same for both cases.

sample	t_D , high fluence [fs]	t_D , reduced fluence [fs]
Ni reference	140 ± 10	185 ± 30
delay of onset	25 ± 30	70 ± 40
Au/Ni	330 ± 40	400 ± 160

Table 5.1: **Demagnetization time constants vs. fluence in Au/Ni.** *The characteristic time constants of demagnetization t_D for the Ni layers in the Au/Ni as well as the Ni reference sample were derived from exponential fits to the data as described in the text. "High fluence" refers to the pump conditions leading to about 75 % demagnetization in both samples, while the magnitude of demagnetization was about 50 % in the "reduced fluence" case.*

5.3 Theoretical Description of Ultrafast Demagnetization in Au/Ni

Having shown in the previous section that demagnetization of the buried Ni layer in Au/Ni is possible, it is now desirable to compare the observed results to the predictions made by theoretical models for the microscopic origin of ultrafast demagnetization, especially with regards to the observed magnitude of demagnetization for the pump fluence used. Therefore, I will first calculate the effective absorbed fluence in the Ni layer in both samples, Au/Ni and the Ni reference.

Starting with the high fluence scenario, the reflectivities of the respective cap layers, 0.880 for Au in Au/Ni and 0.518 for Pt in the Ni reference, are taken into account for calculating the fluence absorbed in the sample from the values of the incident fluence of 33.2 mJ/cm^2 for Au/Ni and 9.9 mJ/cm^2 for the Ni reference. This results in an absorbed fluence of 4.0 mJ/cm^2 for the whole Au/Ni sample and 4.8 mJ/cm^2 for the Ni reference, showing that despite a lower incident fluence, the total absorbed fluence in the Ni reference is actually slightly higher due to a lower reflectivity of the Pt cap layer. From the calculated pump laser absorption profiles in Chapter 5.1 it is known that, in Au/Ni, only 5 % of the absorbed fluence is absorbed in the ferromagnetic Ni layer, leading to an effective pump fluence for the Ni layer only of just 0.2 mJ/cm^2 . In comparison, in the Ni reference, 55 % of the absorbed fluence is absorbed in the Ni layer, resulting in an effective pump fluence of 2.6 mJ/cm^2 . And yet, the observed magnitude of demagnetization of about 75 % of the initial magnetic moment is similar for both samples.

In the low fluence scenario, effective pump fluences for the Ni layers in Au/Ni and in the Ni reference of 0.1 mJ/cm^2 and 1.7 mJ/cm^2 , respectively, are obtained. In this case, too, a much lower fluence absorbed in the Ni layer in Au/Ni leads to a demagnetization of about 50 %, as large as in the Ni reference.

In the following, I will discuss how through these findings, taken together with the respective time constants of demagnetization for Au/Ni and the Ni reference derived in Chapter 5.2, the relative contribution of two microscopic mechanisms proposed for the underlying origin of ultrafast demagnetization can be estimated. These two mechanisms are direct interaction between the pump laser photons and the electron spins, as first introduced in Chapter 2.3.1, and superdiffusive spin transport (see Chapter 2.3.3).

5.3.1 Direct Interaction Between Photons and Spins

One of the earliest microscopic explanations for ultrafast demagnetization was proposed by Zhang et al. in 2000 [47]. According to the authors, pump laser field and spin-orbit coupling act together to induce demagnetization in the sample material.

A later iteration of this type of microscopic model by Bigot et al. [52] additionally takes a dynamic modification of the spin-orbit interaction due to the laser field into account, leading to a coherent interaction between the laser field and the electron spins during the pulse duration. A more detailed description of these models was already given in Chapter 2.3.1, and various criticisms discussed. In particular, recent theoretical calculations by Essert et al. [49] found that excitation with the electrical field generated by an incident laser pulse with a fluence of 4 mJ/cm^2 only leads to a decrease of the magnetization of below 1 % in Ni and Fe. Here, I would like to emphasize that the magnitude and time constants of the experimentally observed demagnetization in Au/Ni and the Ni reference, depending on the absorbed pump laser energy, allows me to exclude such a direct interaction between photons and spins as the dominant process behind ultrafast demagnetization.

Unfortunately, Zhang et al. [47] do not specify the pump laser intensities needed to achieve significant demagnetization in their theoretical description. They do state, however, that there is an exponential dependence of the magnitude of demagnetization on the absorbed intensity; when the intensity is reduced by a factor of 10, no demagnetization occurs any more. But this is contrary to the experimental observation of equal magnitudes of demagnetization despite an absorbed fluence in the Ni layer of Au/Ni that is only a few percent of the fluence absorbed in the Ni layer of the Ni reference. Also, Zhang et al. [47] predict a saturation of the magnitude of demagnetization at 50 % – here, a magnitude of demagnetization of about 75 % is experimentally observed in the high fluence scenario (compare Figure 5.3).

Furthermore, according to Zhang et al. [47], demagnetization happens only during the presence of the pump laser pulse and the observed demagnetization time-constant is basically given by the pump pulse length. However, even if demagnetization in the buried Ni layer of Au/Ni is induced by the small number of photons able to reach this layer, the length of the pump laser pulse is the same as for the Ni reference, and the time constant should thus be the same. But as seen in Chapter 5.2, ultrafast demagnetization in Au/Ni proceeds with a time constant of $330 \pm 40 \text{ fs}$, significantly longer than for the Ni reference.

In the conceptually similar model by Bigot et al. [52], a signature of their proposed coherent photon-spin interaction is observed at an absorbed fluence of 1 mJ/cm^2 in a 7.5 nm thick Ni layer. Since, for the Ni reference in both the high and reduced fluence scenario in the experiment presented here, the fluence absorbed in the Ni layer exceeds 1 mJ/cm^2 , a coherent photon-spin interaction could in principle occur. Still, for the much lower absorbed fluence in the buried Ni layer in Au/Ni a significant contribution from coherent photon-spin interaction can be ruled out: Bigot et al. see no signature of the coherent process for absorbed fluences below about 0.1 mJ/cm^2 [52], whereas here the buried Ni layer in Au/Ni is pumped with no more than 0.1 mJ/cm^2 in the low fluence scenario but still shows a significant demagnetization of 50 %.

So both theories, by Zhang et al. [47] and Bigot et al. [52], are not sufficient to explain the observed magnitude of demagnetization in Au/Ni. While it cannot be ruled out that a direct or coherent interaction of the laser field with the spins occurs during the presence of the pump laser pulse, it does not result in the experimentally observed demagnetization in Au/Ni.

5.3.2 Superdiffusive Spin Transport

Having excluded direct interaction between the pump laser photons and the electron spins as an explanation for the ultrafast demagnetization of the buried Ni layer in Au/Ni in the previous section, it is highly likely that electron transport into the ferromagnetic layer is the reason behind the effects observed in Chapter 5.2.

In order to get a more detailed picture for the sample geometries used here, model

calculations were performed by M. Battiato, P. Maldonado and P.M. Oppeneer from Uppsala University [109], using a numerical solution of their superdiffusive spin transport model [4, 61], already introduced in Chapter 2.3.3.

For the theoretical modeling, the spatial and temporal profile of the pump laser was used as input, i.e. spot size, absorption profile and pulse length. The calculations take all layers in the structure of the Au/Ni and Ni reference samples as described in Chapter 5.1 into account. The superdiffusive spin transport model assumes transport to be uniaxial in the direction perpendicular to the sample surface [4], since typical pump spot sizes are much larger than the electron mean free path. This assumption is fully justified in our case since the pump spot size was $800\ \mu\text{m}$, compared to electron mean free paths in the tens of nanometers. The absorbed pump fluences used in the simulations are $4.0\ \text{mJ}/\text{cm}^2$ in the Au/Ni sample, and $6.3\ \text{mJ}/\text{cm}^2$ in the Ni reference sample. The spin and energy dependent electron lifetimes are taken from refs. [62] and [110]. The results from the simulation can be seen in Figure 5.5.

Comparing the theoretical results with the experimental results from Figure 5.4, the qualitative agreement is immediately obvious. In the simulated curves, both the Ni reference and Au/Ni show a sub-ps demagnetization, with Au/Ni being slower to demagnetize. Looking closer, the simulated demagnetization also agrees quite well quantitatively with the experiment: The maximum amount of demagnetization is reached at a pump-probe delay of about 750 fs for the Ni reference, compared to about 1.2 ps for Au/Ni. A slight delay in the onset of demagnetization also fits well with the experimental results.

The ultrafast demagnetization of the Ni layers in the Ni reference and Au/Ni is explained by the spin-dependent transport of hot carriers. The situation in the Ni reference is similar to superdiffusive spin transport in a 15 nm Ni film on an Al substrate calculated earlier by Battiato et al. [4]. Both majority and minority electrons are excited mainly in the Ni layer. Majority electrons have a longer mean free path than minority electrons and are thus transported out of the Ni layer, into the Al substrate and also the Pt cap and buffer layers. Minority electrons remain trapped in the Ni layer. The ultrafast demagnetization observed is therefore a consequence of the unequal transport properties of hot majority and minority electrons during their thermalization. Magnetization is effectively shifted out of the ferromagnetic layer probed with element-sensitive XMCD.

In Au/Ni, electrons are mainly excited in the Au layer. The subsequent electron current going into the Ni layer is not spinpolarized. Only when the majority and minority electrons reach the Ni layer, the spin dependency of the electron lifetime in Ni leads, again, to a higher probability of majority electrons leaving the ferromagnetic layer and traveling into buffer layer and substrate, whereas minority electrons become trapped in the Ni layer. A backflow of cascade electrons – both majority and minority – created by inelastic scatterings of minority electrons in Ni also contributes to the demagnetization, because the majority cascade electrons escape to the Au layer and the substrate side. This leads to further accumulation of minority electrons in Ni, in particular at the interfaces.

The superdiffusive spin transport model somewhat underestimates the amount of demagnetization in both samples. For the absorbed pump fluences used in the simulation seen in Figure 5.5, a reduction of the magnetization of about 50 % of the initial value is reached. In the experiment, a demagnetization closer to 70 % was observed for similar absorbed pump fluences (compare the high fluence scenario in Figure 5.3). This discrepancy is likely due to the fact that the superdiffusive spin transport model incorporates a linear dependence of the amount of demagnetization on the pump fluence. Non-linear effects coming from changes in the occupation of the electron density of states in Ni during the superdiffusive transport, that can

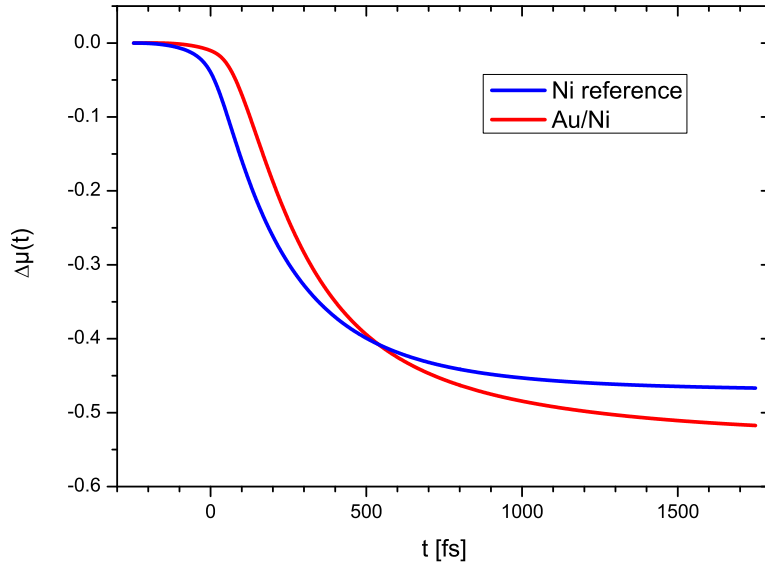


Figure 5.5: **Simulated ultrafast demagnetization of Au/Ni.** *The transient reduction of the Ni magnetic moment $\Delta\mu$ in the Ni reference (blue line) and in Au/Ni (red line), depending on the pump-probe delay t , as calculated with the superdiffusive spin transport model. Figure courtesy of Marco Battiato.*

further enhance the demagnetization, are not included so far.

The successful modeling of the timescales of demagnetization in the Ni reference and Au/Ni shows that spin transport can contribute significantly to ultrafast demagnetization. In Au/Ni, the superdiffusive spin transport is actually the only theoretical model developed so far that can explain the experimental observations. Direct interaction between photons and spins could be excluded as the dominant cause of ultrafast demagnetization in Au/Ni (see Chapter 5.3.1). Finally, it should be noted that phonon-mediated spin flips [27] are also unlikely to cause ultrafast demagnetization in Au/Ni of the magnitude observed here, since significant spin-flip probabilities occur only in highly non-equilibrium electron distributions [59]. However, due to the fact that most of the laser intensity is absorbed in the Au layer of Au/Ni, the electron system in the Ni layer is not strongly excited by the pump laser pulse.

Chapter 6

Conclusion and Outlook

With element-resolved XMCD measurements at the BESSY II Femtoslicing facility I investigated the ultrafast demagnetization of ferromagnetic NiFe and GdTb alloys as well as a Au/Ni multilayer structure with 130 fs time resolution. These measurements contribute to the microscopic understanding of ultrafast magnetization dynamics in two regards: The relation between the time constant of demagnetization and materials properties is clarified, and the relative contribution of different microscopic mechanisms for the underlying origin of ultrafast demagnetization proposed by theory can be estimated.

6.1 Materials Dependence of Ultrafast Demagnetization

Measurements on the ultrafast demagnetization of $\text{Ni}_{50}\text{Fe}_{50}$ and $\text{Ni}_{80}\text{Fe}_{20}$ revealed that the characteristic time constant of demagnetization varies with the magnetic moment of the respective sublattice – Ni or Fe – and the strength of exchange interaction between the sublattices. Static XMCD spectroscopy shows that the constituents' magnetic moments in $\text{Ni}_{50}\text{Fe}_{50}$ and $\text{Ni}_{80}\text{Fe}_{20}$ can be quite different from the respective pure materials, up to a factor of two in the case of Ni in $\text{Ni}_{50}\text{Fe}_{50}$. The characteristic time constants of demagnetization in the alloys also deviate from those found for pure Ni and Fe. Broadly speaking, the time constant of demagnetization is longer for larger magnetic moments. This also leads to distinctly different time constants for the Ni and Fe sublattices in both NiFe alloys, so that they exhibit decoupled dynamics after laser excitation. However, exchange coupling cannot be neglected in a theoretical description of the observed behavior, as the example of Ni in $\text{Ni}_{50}\text{Fe}_{50}$ shows, whose shorter demagnetization time constant compared to pure Ni, despite a larger magnetic moment, could only be correctly predicted when the intersublattice exchange interaction between Ni and Fe in $\text{Ni}_{50}\text{Fe}_{50}$ was taken into account.

$\text{Gd}_{60}\text{Tb}_{40}$ shows a two-step demagnetization which is also characteristic for the pure rare earths Gd and Tb. A sub-ps demagnetization is followed by a second, slower decrease of the magnetic moment. The time constant for this second decrease was previously linked to the strength of spin-lattice coupling [29], with the stronger spin-lattice coupling in Tb causing a faster demagnetization. In $\text{Gd}_{60}\text{Tb}_{40}$, the demagnetization of Gd follows Tb on all timescales, leading to a characteristic time constant of 5.0 ± 2.9 ps for the second decay. This deviation from the slow demagnetization with a time constant of 40 ps in pure Gd [29] can be explained with the indirect exchange interaction linking the Gd 4f magnetic moments in the alloy to the Tb 4f moments, which have a strong direct coupling to the lattice. An

additional channel for the dissipation of Gd spin angular momentum to the lattice is thus opened, resulting in a faster demagnetization compared to pure Gd.

These results show that magnetization dynamics can be tuned by changing the properties of a ferromagnetic material through alloying. This might pave the way for new materials for magnetic storage media, which could be tailored to exhibit a certain dynamic behavior.

6.2 Applicability of Proposed Theoretical Models for Ultrafast Demagnetization

The most prominent theoretical models proposed for the microscopic origin of ultrafast demagnetization are direct interaction between photons and spins [47, 52], phonon mediated spin-flip scattering [27] and superdiffusive spin transport [4]. Time-resolved measurements of the ultrafast demagnetization of a Ni layer buried under a Au cap layer, which was made thick enough to absorb nearly all of the incident pump laser light, showed that direct interaction between photons and spins could not explain the magnitude and time constant of the observed demagnetization. Instead, simulations based on the superdiffusive spin transport model reproduced the slower, delayed demagnetization of the buried Ni layer in Au/Ni compared to a Ni reference sample. This gives a strong indication for a central role of superdiffusive spin transport in ultrafast magnetization dynamics.

The M3TM [27], a model based on phonon mediated spin-flip scattering, could describe broad trends in the demagnetization time constants of Ni, Fe and their alloys. It does not take exchange interaction into account, however, and therefore failed to describe the accelerated demagnetization of Ni in Ni₅₀Fe₅₀. Moreover, the spin-flip probability assumed by the M3TM has been calculated to be large enough only in strongly nonequilibrium electron distributions [59]. My finding of a significant demagnetization in the buried Ni layer of Au/Ni, which is not strongly excited, would suggest no more than a small contribution to the demagnetization by phonon mediated spin flips.

6.3 Outlook

As a short outlook, I would like to mention two topics: A continuation of my work on ultrafast demagnetization caused by hot electron injection into a ferromagnetic layer, and future experiments with complementary and improved fs x-ray sources.

6.3.1 Demagnetization through Injection of Spin-polarized Electrons in Co/Ru/Fe

Chapter 5 showed that an electron current which is not spinpolarized can induce ultrafast demagnetization. But would a spinpolarized electron current work equally well, or even induce different effects such as enhancement or generation of magnetization?

By exciting a ferromagnetic thin film with a fs laser pulse, a spinpolarized hot carrier pulse can be generated [111]. Here, I used a sample consisting of two ferromagnetic layers separated by a thin Ru spacer layer. The thickness of the upper ferromagnetic layer, a 20 nm thick Co layer, is matched to the penetration depth of the pump laser, so that hot electrons are mainly excited in this layer. With XMCD in transmission geometry, the transient behavior of the lower ferromagnetic layer, a 20 nm thick Fe layer, is probed at the Fe L₃-edge, whereas the upper layer is probed at the Co L₃-edge. The Ru spacer layer leads to an antiparallel orientation

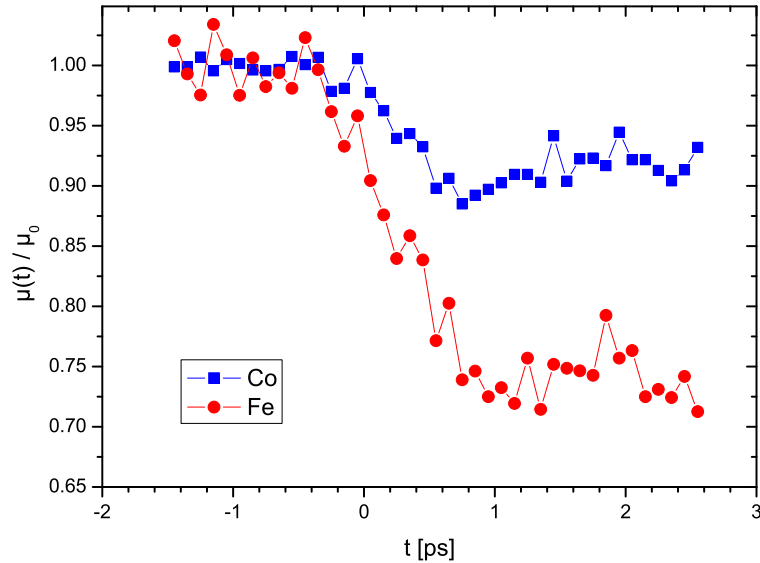


Figure 6.1: **Time-resolved XMCD measurement of Co/Ru/Fe.** *The evolution of the magnetic moment μ depending on the temporal delay t between pump laser and probe x-ray pulse is displayed for the upper Co layer (blue squares) compared to the lower Fe layer (red circles). The magnetic moments of the Fe and Co layers are aligned parallel in an external magnetic field. μ is normalized to the average value μ_0 for the unexcited sample.*

of the magnetic moments of the Co and Fe layers without an external magnetic field, while the two ferromagnetic layers can also be oriented parallel in an external magnetic field of 0.2 T. First time- and layer-resolved XMCD measurements for a parallel alignment of the two ferromagnetic layers can be seen in Figure 6.1. Both ferromagnetic layers show ultrafast demagnetization. Additional measurements are planned in order to unveil the dependence of the observed demagnetization on pump fluence and the relative orientation of the ferromagnetic layers.

6.3.2 Methodical Improvements and Complementary X-ray Sources

The measurements shown in this thesis were only made possible by the reliable performance of the Femtoslicing facility at BESSY II, in particular after the recent upgrade. However, due to the still low flux of the fs x-rays, time-resolved measurements take several days and weeks, and small pump induced effects are difficult to resolve. Therefore, further upgrades of the Femtoslicing facility are desirable, especially with regards to the unique properties of the BESSY II source: Circularly polarized 100 fs pulses in the soft x-ray range. Laboratory sources based on high harmonic generation (HHG) do not routinely reach the soft x-ray range yet, although first proof-of-principle experiments have been performed [112], and they do not deliver circular polarization. Therefore, ultrafast magnetic measurements at HHG sources so far have to rely on the transverse magneto-optic Kerr effect, which is element selective when probed resonantly, but can also contain optical artifacts

like its counterpart in the visible wavelength range [113]. Circular polarization can in principle be generated at free electron lasers (FELs) [114], but it is not implemented at any of the currently operating FEL facilities.

For enhancing the x-ray flux, the Femtoslicing source itself as well as the monochromators can be upgraded. In the long term, replacing the undulator currently used as the radiator with an in-vacuum design is expected to increase the x-ray flux by an order of magnitude. On a more short term basis, an upgrade of the ZPM monochromator is currently in the planning stages, which will lead to a smaller x-ray focus size and increased mechanical stability of the beamline.

Another planned upgrade involves the change of the BESSY II accelerator operation from decay mode to top-up mode. BESSY II currently operates in decay mode, where new electrons are injected into the storage ring every eight hours, in order to refill the decayed ring current. In top-up operation, expected to begin in the second half of 2012, electrons will be constantly re-injected into the storage ring, keeping the ring current at a constant level. This will lead to a higher fs x-ray flux at all times and increased stability of the source, since lifetime effects from the decaying electron bunch current that occur in decay mode are avoided.

Lastly, improvements can also be made in the detection of the transmitted x-rays. The energy dispersed x-ray beam from the ZPM can be mapped on an 1D spatial detector, allowing for the parallel detection of full absorption and XMCD spectra at each step in the pump-probe delay.

As mentioned in the introduction of this thesis, in concert with investigating the elementary *time* scales, measuring on elementary *length* scales would also contribute to the microscopic understanding of ultrafast magnetization dynamics. This can be achieved with pump-probe experiments at free electron lasers (FELs), by using diffractive imaging of magnetic domains in real space with linearly polarized light [115] or by resonant magnetic small-angle scattering, which maps the reciprocal space. The high intensity of FEL pulses makes it possible to record domain patterns with resonant magnetic small-angle scattering [116], even with single FEL shots [117]. However, while FELs can generate very short x-ray pulses, down to 10 fs or even less, the self-amplified spontaneous emission (SASE) process [118, 119] employed for the generation of the ultrashort x-ray pulses leads to fluctuations in the intensity and arrival time of individual pulses. Combined with the fact that the pump laser pulses come from a different source than the x-ray probe pulses, the time resolution achievable in pump-probe experiments suffers due to timing jitter between pump and probe [120, 121, 122]. Providing that the time resolution can be improved, for example through pump-probe cross-correlation schemes [92, 93], the way is open for spatially resolved ultrafast magnetic measurements.

Bibliography

- [1] E. Beaurepaire, J.-C. Merle, A. Daunois, and J.-Y. Bigot, *Ultrafast Spin Dynamics in Ferromagnetic Nickel*, Phys. Rev. Lett. **76**, 4250 (1996).
- [2] C.D. Stanciu, F. Hansteen, A.V. Kimel, A. Kirilyuk, A. Tsukamoto, A. Itoh, and Th. Rasing, *All-Optical Magnetic Recording with Circularly Polarized Light*, Phys. Rev. Lett. **99**, 047601 (2007).
- [3] G. Malinowski, F. Dalla Longa, J.H.H. Rietjens, P.V. Paluskar, R. Huijink, H.J.M. Swagten and B. Koopmans, *Control of speed and efficiency of ultrafast demagnetization by direct transfer of spin angular momentum*, Nat. Phys. **4**, 855 (2008).
- [4] M. Battiato, K. Carva, and P.M. Oppeneer, *Superdiffusive Spin Transport as a Mechanism of Ultrafast Demagnetization*, Phys. Rev. Lett. **105**, 027203 (2010).
- [5] I. Tudosa, C. Stamm, A.B. Kashuba, F. King, H.C. Siegmann, J. Stöhr, G. Ju, B. Lu and D. Weller, *The ultimate speed of magnetic switching in granular recording media*, Nature **428**, 831 (2004).
- [6] J.-W. Kim, K.-D. Lee, J.-W. Jeong, and S.-C. Shin, *Ultrafast spin demagnetization by nonthermal electrons of TbFe alloy film*, Appl. Phys. Lett. **94**, 192506 (2009).
- [7] J. Wang, C. Sun, J. Kono, A. Oiwa, H. Munekata, L. Cywinski, and L.J. Sham, *Ultrafast Quenching of Ferromagnetism in InMnAs Induced by Intense Laser Irradiation*, Phys. Rev. Lett. **95**, 167401 (2005).
- [8] K. Holldack, N. Pontius, E. Schierle, T. Kachel, V. Soltwisch, R. Mitzner, T. Quast, G. Springholz, and E. Weschke, *Ultrafast dynamics of antiferromagnetic order studied by femtosecond soft x-ray diffraction*, Appl. Phys. Lett. **97**, 062502 (2010).
- [9] I. Radu, K. Vahaplar, C. Stamm, T. Kachel, N. Pontius, H.A. Dürr, T.A. Ostler, J. Barker, R.F.L. Evans, R.W. Chantrell, A. Tsukamoto, A. Itoh, A. Kirilyuk, Th. Rasing and A.V. Kimel, *Transient ferromagnetic-like state mediating ultrafast reversal of antiferromagnetically coupled spins*, Nature **472**, 205 (2011).
- [10] T. Ogasawara, N. Iwata, Y. Murakami, H. Okamoto, and Y. Tokura, *Submicron-scale spatial feature of ultrafast photoinduced magnetization reversal in TbFeCo thin film*, Appl. Phys. Lett. **94**, 162507 (2009).
- [11] H.E. Elsayed-Ali, T. Juhasz, G.O. Smith, and W.E. Bron, *Femtosecond thermorefectivity and thermotransmissivity of polycrystalline and single-crystalline gold films*, Phys. Rev. B **43**, 4488 (1991).

- [12] W.S. Fann, R.Storz, H.W.K. Tom, and J. Bokor, *Direct Measurement of Nonequilibrium Electron-Energy Distributions in Subpicosecond Laser-Heated Gold Films*, Phys. Rev. Lett. **68**, 2834 (1992).
- [13] W.S. Fann, R.Storz, H.W.K. Tom, J. Bokor, *Electron thermalization in gold*, Phys. Rev. B **46**, 13592 (1992).
- [14] T. Juhasz, H.E. Elsayed-Ali, G.O. Smith, C. Suarez, and W.E. Bron, *Direct measurement of the transport of nonequilibrium electrons in gold films with different crystal structures*, Phys. Rev. B **48**, 15488 (1993).
- [15] A. Vaterlaus, T. Beutler, and F. Meier, *Spin-Lattice Relaxation Time of Ferromagnetic Gadolinium Determined with Time-Resolved Spin-Polarized Photoemission*, Phys. Rev. Lett. **67**, 3314 (1991).
- [16] A. Vaterlaus, T. Beutler, D. Guarisco, M. Lutz, and F. Meier, *Spin-lattice relaxation in ferromagnets studied by time-resolved spin-polarized photoemission*, Phys. Rev. B **46**, 5280 (1992).
- [17] J. Hohlfeld, E. Matthias, R. Knorren, K.H. Bennemann, *Nonequilibrium Magnetization Dynamics of Nickel*, Phys. Rev. Lett. **78**, 4861 (1997).
- [18] J. Güdde, U. Conrad, V. Jähnke, and E. Matthias, *Magnetization dynamics of Ni and Co films on Cu(001) and of bulk nickel surfaces*, Phys. Rev. B **59**, R6608 (1999).
- [19] H. Regensburger, R. Vollmer, and J. Kirschner, *Time-resolved magnetization-induced second-harmonic generation from the Ni(110) surface*, Phys. Rev. B **61**, 14716 (2000).
- [20] B. Koopmans, M. van Kampen, J.T. Kohlhepp, and W.J.M. de Jonge, *Ultrafast Magneto-Optics in Nickel: Magnetism or Optics?*, Phys. Rev. Lett. **85**, 844 (2000).
- [21] A. Scholl, L. Baumgarten, R. Jacquemin, and W. Eberhardt, *Ultrafast Spin Dynamics of Ferromagnetic Thin Films Observed by fs Spin-Resolved Two-Photon Photoemission*, Phys. Rev. Lett. **79**, 5146 (1997).
- [22] A. Weber, F. Pressacco, S. Günther, E. Mancini, P.M. Oppeneer, and C.H. Back, *Ultrafast demagnetization dynamics of thin Fe/W(110) films: Comparison of time- and spin-resolved photoemission with time-resolved magneto-optic experiments*, Phys. Rev. B **84**, 132412 (2011).
- [23] C. Stamm, T. Kachel, N. Pontius, R. Mitzner, T. Quast, K. Holldack, S. Khan, C. Lupulescu, E.F. Aziz, M. Wietstruk, H.A. Dürr and W. Eberhardt, *Femtosecond modification of electron localization and transfer of angular momentum in nickel*, Nat. Mater. **6**, 740 (2007).
- [24] C. Stamm, N. Pontius, T. Kachel, M. Wietstruk, and H.A. Dürr, *Femtosecond x-ray absorption spectroscopy of spin and orbital angular momentum in photoexcited Ni films during ultrafast demagnetization*, Phys. Rev. B **81**, 104425 (2010).
- [25] F. Dalla Longa, J.T. Kohlhepp, W.J.M. de Jonge, and B. Koopmans, *Influence of photon angular momentum on ultrafast demagnetization in nickel*, Phys. Rev. B **75**, 224431 (2007).
- [26] B. Koopmans, J.J.M. Ruigrok, F. Dalla Longa, and W.J.M. de Jonge, *Unifying Ultrafast Magnetization Dynamics*, Phys. Rev. Lett. **95**, 267207 (2005).

- [27] B. Koopmans, G. Malinowski, F. Dalla Longa, D. Steiauf, M. Fähnle, T. Roth, M. Cinchetti and M. Aeschlimann, *Explaining the paradoxical diversity of ultrafast laser-induced demagnetization*, Nat. Mater. **9**, 259 (2009).
- [28] E. Carpene, E. Mancini, C. Dallera, M. Brenna, E. Puppini, and S. De Silvestri, *Dynamics of electron-magnon interaction and ultrafast demagnetization in thin iron films*, Phys. Rev. B **78**, 174422 (2008).
- [29] M. Wietstruk, A. Melnikov, C. Stamm, T. Kachel, N. Pontius, M. Sultan, C. Gahl, M. Weinelt, H.A. Dürr, and U. Bovensiepen, *Hot-Electron-Driven Enhancement of Spin-Lattice Coupling in Gd and Tb 4f Ferromagnets Observed by Femtosecond X-Ray Magnetic Circular Dichroism*, Phys. Rev. Lett. **106**, 127401 (2011).
- [30] M. Sultan, A. Melnikov, and U. Bovensiepen, *Ultrafast magnetization dynamics of Gd(0001): Bulk versus surface*, Phys. Status Solidi B **248**, 2323 (2011).
- [31] M. Sultan, U. Atxitia, A. Melnikov, O. Chubykalo-Fesenko, and U. Bovensiepen, *Electron- and phonon-mediated ultrafast magnetization dynamics of Gd(0001)*, Phys. Rev. B **85**, 184407 (2012).
- [32] M. Wietstruk, *Ultraschnelle Magnetisierungsdynamik in itineranten und Heisenberg-Ferromagneten*, PhD thesis, Technische Universität Berlin (2010).
- [33] C.A.C. Bosco, A. Azevedo, and L.H. Acioli, *Substrate dependent ultrafast dynamics in thin NiFe films*, Appl. Phys. Lett. **83**, 1767 (2003).
- [34] H.-S. Rhie, H.A. Dürr, and W. Eberhardt, *Femtosecond Electron and Spin Dynamics in Ni/W(110) Films*, Phys. Rev. Lett. **90**, 247201 (2003).
- [35] J. Walowski, G. Müller, M. Djordjevic, M. Münzenberg, C.A.F. Vaz, and J.A.C. Bland, *Energy Equilibration Processes of Electrons, Magnons, and Phonons at the Femtosecond Time Scale*, Phys. Rev. Lett. **101**, 237401 (2008).
- [36] A. Kirilyuk, A.V. Kimel, and Th. Rasing, *Ultrafast optical manipulation of magnetic order*, Rev. Mod. Phys. **82**, 2731 (2010).
- [37] U. Atxitia, O. Chubykalo-Fesenko, N. Kazantseva, D. Hinzke, U. Nowak, R.W. Chantrell, *Micromagnetic modelling of laser-induced magnetization dynamics using the Landau-Lifshitz-Bloch equation*, Appl. Phys. Lett. **91**, 232507 (2007).
- [38] U. Atxitia and O. Chubykalo-Fesenko, *Ultrafast magnetization dynamics rates within the Landau-Lifshitz-Bloch model*, Phys. Rev. B **84**, 144414 (2011).
- [39] U. Atxitia, O. Chubykalo-Fesenko, J. Walowski, A. Mann, and M. Münzenberg, *Evidence for thermal mechanisms in laser-induced femtosecond spin dynamics*, Phys. Rev. B **81**, 174401 (2010).
- [40] C. Bunce, J. Wu, G. Ju, B. Lu, D. Hinzke, N. Kazantseva, U. Nowak, and R.W. Chantrell, *Laser-induced magnetization switching in films with perpendicular anisotropy: A comparison between measurements and a multi-macrospin model*, Phys. Rev. B **81**, 174428 (2010).
- [41] I. Radu, G. Woltersdorf, M. Kiessling, A. Melnikov, U. Bovensiepen, J.-U. Thiele, and C.H. Back, *Laser-Induced Magnetization Dynamics of Lanthanide-Doped Permalloy Thin Films*, Phys. Rev. Lett. **102**, 117201 (2009).

- [42] C. La-O-Vorakiat, M. Siemens, M.M. Murnane, H.C. Kapteyn, S. Mathias, M. Aeschlimann, *Ultrafast Demagnetization Dynamics at the M Edges of Magnetic Elements Observed Using a Tabletop High-Harmonic Soft X-Ray Source*, Phys. Rev. Lett. **103**, 257402 (2009).
- [43] S. Mathias, C. La-O-Vorakiat, P. Grychtol, P. Granitzka, E. Turgut, J.E. Shaw, R. Adam, H.T. Nembach, M.E. Siemens, S. Eich, C.M. Schneider, T.J. Silva, M. Aeschlimann, M.M. Murnane, and H.C. Kapteyn, *Probing the timescale of the exchange interaction in a ferromagnetic alloy*, <http://www.pnas.org/cgi/doi/10.1073/pnas.1201371109> (2012).
- [44] D. Steil, S. Alebrand, T. Roth, M. Krauß, T. Kubota, M. Oogane, Y. Ando, H.C. Schneider, M. Aeschlimann, and M. Cinchetti, *Band-Structure-Dependent Demagnetization in the Heusler Alloy $\text{Co}_2\text{Mn}_{1-x}\text{Fe}_x\text{Si}$* , Phys. Rev. Lett. **105**, 217202 (2010).
- [45] G.M. Müller, J. Walowski, M. Djordjevic, G.-X. Miao, A. Gupta, A.V. Ramos, K. Gehrke, V. Moshnyaga, K. Samwer, J. Schmalhorst, A. Thomas, A. Hütten, G. Reiss, J.S. Moodera and M. Münzenberg, *Spin polarization in half-metals probed by femtosecond spin excitation*, Nat. Mater. **8**, 56 (2009).
- [46] J. Mentink, J. Hellsvik, D.V. Afanasiev, B.A. Ivanov, A. Kirilyuk, A.V. Kimel, O. Eriksson, M.I. Katsnelson, and Th. Rasing, *Ultrafast Spin Dynamics in Multisublattice Magnets*, Phys. Rev. Lett. **108**, 057202 (2012).
- [47] G.P. Zhang and W. Hübner, *Laser-Induced Ultrafast Demagnetization in Ferromagnetic Metals*, Phys. Rev. Lett. **85**, 3025 (2000).
- [48] M.S. Si and G.P. Zhang, *Resolving photon-shortage mystery in femtosecond magnetism*, J. Phys.: Condens. Matter **22**, 076005 (2010).
- [49] S. Essert and H.C. Schneider, *Electron-phonon scattering dynamics in ferromagnetic metals and their influence on ultrafast demagnetization processes*, Phys. Rev. B **84**, 224405 (2011).
- [50] G.P. Zhang, W. Hübner, G. Lefkidis, Y. Bai and T.F. George, *Paradigm of the time-resolved magneto-optical Kerr effect for femtosecond magnetism*, Nat. Phys. **5**, 499 (2009).
- [51] K. Carva, M. Battiato and P.M. Oppeneer, *Is the controversy over femtosecond magneto-optics really solved?*, Nat. Phys. **7**, 655 (2011).
- [52] J.-Y. Bigot, M. Vomir and E. Beaurepaire, *Coherent ultrafast magnetism induced by femtosecond laser pulses*, Nat. Phys. **5**, 515 (2009).
- [53] B. Koopmans, H.H.J.E. Kicken, M. van Kampen, W.J.M. de Jonge, *Microscopic model for femtosecond magnetization dynamics*, J. Magn. Magn. Mater. **286**, 271 (2005).
- [54] R.J. Elliott, *Theory of the Effect of Spin-Orbit Coupling on Magnetic Resonance in Some Semiconductors*, Phys. Rev. **96**, 266 (1954).
- [55] Y. Yafet, in: F. Seitz and D. Turnbull (Eds.), *Solid State Physics* Vol. 14, Academic, 1963.
- [56] D. Steiauf, C. Illg, M. Fähnle, *Extension of Yafet's theory of spin relaxation to ferromagnets*, J. Magn. Magn. Mater. **322**, L5 (2010).

- [57] M. Fähnle, J. Seib, and C. Illg, *Relating Gilbert damping and ultrafast laser-induced demagnetization*, Phys. Rev. B **82**, 144405 (2010).
- [58] D. Steiauf and M. Fähnle, *Elliot-Yafet mechanism and the discussion of femtosecond magnetization dynamics*, Phys. Rev. B **79**, 140401(R) (2009).
- [59] K. Carva, M. Battiato, and P.M. Oppeneer, *Ab Initio Investigation of the Elliot-Yafet Electron-Phonon Mechanism in Laser-Induced Ultrafast Demagnetization*, Phys. Rev. Lett. **107**, 207201 (2011).
- [60] M. Krauß, T. Roth, S. Alebrand, D. Steil, M. Cinchetti, M. Aeschlimann, and H.C. Schneider, *Ultrafast demagnetization of ferromagnetic transition metals: The role of the Coulomb interaction*, Phys. Rev. B **80**, 180407(R) (2009).
- [61] M. Battiato, K. Carva, P.M. Oppeneer, *Theory of laser-induced ultrafast superdiffusive spin transport in layered heterostructures*, submitted (2012).
- [62] V.P. Zhukov, E.V. Chulkov, and P.M. Echenique, *Lifetimes and inelastic mean free path of low-energy excited electrons in Fe, Ni, Pt, and Au: Ab initio GW+T calculations*, Phys. Rev. B **73**, 125105 (2006).
- [63] C. Boeglin, E. Beaurepaire, V. Halte, V. Lopez-Flores, C. Stamm, N. Pontius, H.A. Dürr and J.-Y. Bigot, *Distinguishing the ultrafast dynamics of spin and orbital moments in solids*, Nature **465**, 458 (2010).
- [64] W. Ackermann et al., *Operation of a free-electron laser from the extreme ultraviolet to the water window*, Nat. Photonics **1**, 336 (2007).
- [65] P. Emma et al., *First lasing and operation of an angstrom-wavelength free-electron laser*, Nat. Photonics **4**, 641 (2010).
- [66] J. Zhou, J. Peatross, M.M. Murnane, H.C. Kapteyn, I.P. Christov, *Enhanced High-Harmonic Generation Using 25 fs Laser Pulses*, Phys. Rev. Lett. **76**, 752 (1996).
- [67] M.-C. Chen, P. Arpin, T. Popmintchev, M. Gerrity, B. Zhang, M. Seaberg, D. Popminchev, M.M. Murnane, and H.C. Kapteyn, *Bright, Coherent, Ultrafast Soft X-Ray Harmonics Spanning the Water Window from a Tabletop Light Source*, Phys. Rev. Lett. **105**, 173901 (2010).
- [68] F. Quirin, M. Vattilana, U. Shymanovich, A.-E. El-Kamhawy, A. Tarasevitch, J. Hohlfeld, D. von der Linde, and K. Sokolowski-Tinten, *Structural dynamics in FeRh during a laser-induced metamagnetic phase transition*, Phys. Rev. B **85**, 020103(R) (2012).
- [69] Operating modi BESSY II, http://www.helmholtz-berlin.de/forschung/grossgeraete/betrieb-beschleuniger/betriebsmodi_en.html
- [70] A.A. Zholents and M.S. Zolotarev, *Femtosecond X-Ray Pulses of Synchrotron Radiation*, Phys. Rev. Lett. **76**, 912 (1996).
- [71] R.W. Schoenlein, S. Chattopadhyay, H.H.W. Chong, T.E. Glover, P.A. Heimann, C.V. Shank, A.A. Zholents, M.S. Zolotarev, *Generation of Femtosecond Pulses of Synchrotron Radiation*, Science **287**, 2237 (2000).
- [72] K. Holldack, T. Kachel, S. Khan, R. Mitzner, and T. Quast, *Characterization of laser-electron interaction at the BESSY II femtoslicing source*, Phys. Rev. Spec. Top. Accel. Beams **8**, 040704 (2005).

- [73] K. Holldack, S. Khan, R. Mitzner, and T. Quast, *Femtosecond Terahertz Radiation from Femtoslicing at BESSY*, Phys. Rev. Lett. **96**, 054801 (2006).
- [74] S. Khan, K. Holldack, T. Kachel, R. Mitzner, and T. Quast, *Femtosecond Undulator Radiation from Sliced Electron Bunches*, Phys. Rev. Lett. **97**, 074801 (2006).
- [75] P. Beaud, S.L. Johnson, A. Streun, R. Abela, D. Abramsohn, D. Grolimund, F. Krasniqi, T. Schmidt, V. Schlott, and G. Ingold, *Spatiotemporal Stability of a Femtosecond Hard-X-Ray Undulator Source Studied by Control of Coherent Optical Phonons*, Phys. Rev. Lett. **99**, 174801 (2007).
- [76] J. Stöhr, *X-ray magnetic circular dichroism spectroscopy of transition metal thin films*, J. Electron. Spectrosc. Relat. Phenom. **75**, 253 (1995).
- [77] C.T. Chen, Y.U. Idzerda, H.-J. Lin, N.V. Smith, G. Meigs, E. Chaban, G.H. Ho, E. Pellegrin, and F. Sette, *Experimental Confirmation of the X-Ray Magnetic Circular Dichroism Sum Rules for Iron and Cobalt*, Phys. Rev. Lett. **75**, 152 (1995).
- [78] B.T. Thole, P. Carra, F. Sette, and G. van der Laan, *X-Ray Circular Dichroism as a Probe of Orbital Magnetization*, Phys. Rev. Lett. **68**, 1943 (1992).
- [79] M. Altarelli, *Orbital-magnetization sum rule for x-ray circular dichroism: A simple proof*, Phys. Rev. B **47**, 597 (1993).
- [80] P. Carra, B.T. Thole, M. Altarelli, and X. Wang, *X-Ray Circular Dichroism and Local Magnetic Fields*, Phys. Rev. Lett. **70**, 694 (1993).
- [81] R. Wu and A.J. Freeman, *Limitation of the Magnetic-Circular-Dichroism Spin Sum Rule for Transition Metals and Importance of the Magnetic Dipole Term*, Phys. Rev. Lett. **73**, 1994 (1994).
- [82] B. Glaubitz, S. Buschhorn, F. Brüssing, R. Abrudan, and H. Zabel, *Development of magnetic moments in $Fe_{1-x}Ni_x$ -alloys*, J. Phys.: Condens. Matter **23**, 254210 (2011).
- [83] S. Mangin, C. Bellouard, S. Andrieu, F. Montaigne, P. Ohresser, N.B. Brookes, and B. Barbara, *Magnetization reversal in exchange-coupled $GdFe/TbFe$ studied by x-ray magnetic circular dichroism*, Phys. Rev. B **70**, 014401 (2004).
- [84] K. Carva, D. Legut and P.M. Oppeneer, *Influence of laser-excited electron distributions on the X-ray magnetic circular dichroism spectra: Implications for femtosecond demagnetization in Ni* , Europhys. Lett. **86**, 57002 (2009).
- [85] W.E. Bailey, L. Cheng, D.J. Keavney, C.-C. Kao, E. Vescovo, and D.A. Arena, *Precessional dynamics of elemental moments in a ferromagnetic alloy*, Phys. Rev. B **70**, 172403 (2004).
- [86] T. Shinjo, T. Okuno, R. Hassdorf, K. Shigeto, T. Ono, *Magnetic Vortex Core Observation in Circular Dots of Permalloy*, Science **289**, 930 (2000).
- [87] M. Hayashi, L. Thomas, C. Rettner, R. Moriya, and S.S.P. Parkin, *Direct observation of the coherent precession of magnetic domain wall propagating along permalloy nanowires*, Nat. Phys. **3**, 21 (2007).
- [88] M. Kläui, *Head-to-head domain walls in magnetic nanostructures*, J. Phys.: Condens. Matter **20**, 313001 (2008).

- [89] H.C. Siegmann and J. Stöhr, *Magnetism: From Fundamentals to Nanoscale Dynamics*, Springer Verlag, Berlin (2004).
- [90] T. Kampfrath, R.G. Ulbrich, F. Leuenberger, M. Münzenberg, B. Sass, and W. Felsch, *Ultrafast magneto-optical response of iron thin films*, Phys. Rev. B **65**, 104429 (2002).
- [91] E.H. Wasserman, in: K.H.J. Buschow and E.P. Wohlfarth (Eds.), *Ferromagnetic Materials* Vol. 5, Elsevier, 1990.
- [92] C. Gahl, A. Azima, M. Beye, M. Deppe, K. Döbrich, U. Hasslinger, F. Hennies, A. Melnikov, M. Nagasono, A. Pietzsch, M. Wolf, W. Wurth and A. Föhlisch, *A femtosecond X-ray/optical cross-correlator*, Nat. Photonics **2**, 165 (2008).
- [93] T. Maltezopoulos, S. Cunovic, M. Wieland, M. Beye, A. Azima, H. Redlin, M. Krikunova, R. Kalms, U. Frühling, F. Budzyn, W. Wurth, A. Föhlisch and M. Drescher, *Single-shot timing measurement of extreme-ultraviolet free-electron laser pulses*, New J. Phys. **10**, 033026 (2008).
- [94] I. Radu, C. Stamm, A. Eschenlohr, K. Vahaplar, T. Kachel, N. Pontius, R. Mitzner, K. Holldack, A. Föhlisch, F. Radu, R.F.L. Evans, T.A. Ostler, J. Mentink, R.W. Chantrell, A. Tsukamoto, A. Itoh, A. Kirilyuk, A.V. Kimel and Th. Rasing, *Ultrafast and Distinct Spin Dynamics in Magnetic Alloys and Heterostructures*, submitted (2012).
- [95] P. Yu, X.F. Jin, J. Kudrnovsky, D.S. Wang, P. Bruno, *Curie temperatures of fcc and bcc nickel and permalloy: Supercell and Green's function methods*, Phys. Rev. B **77**, 054431 (2008).
- [96] D.M.S. Bagguley, J.P. Partington, J.A. Robertson and R.C. Woods, *Magnetisation and microwave absorption in GdTb alloys*, J. Phys. F: Metal Phys. **10**, 967 (1980).
- [97] E.B. Myers, D.C. Ralph, J.A. Katine, R.N. Louie and R.A. Buhrman, *Current-Induced Switching of Domains in Magnetic Multilayer Devices*, Science **285**, 867 (1999).
- [98] M. Kläui, P.-O. Jubert, R. Allenspach, A. Bischof, J.A.C. Bland, G. Faini, U. Rüdiger, C.A.F. Vaz, L. Vila, and C. Vouille, *Direct Observation of Domain-Wall Configurations Transformed by Spin Currents*, Phys. Rev. Lett. **95**, 026601 (2005).
- [99] M. Bolte, G. Meier, B. Krüger, A. Drews, R. Eiselt, L. Bocklage, S. Bohlens, T. Tylliszczak, A. Vansteenkiste, B. Van Waeyenberge, K.W. Chou, A. Puzic, and H. Stoll, *Time-Resolved X-Ray Microscopy of Spin-Torque-Induced Magnetic Vortex Gyration*, Phys. Rev. Lett. **100**, 176601 (2008).
- [100] J.E. Hirsch, *Spin Hall Effect*, Phys. Rev. Lett. **83**, 1834 (1999).
- [101] S.O. Valenzuela and M. Tinkham, *Direct electronic measurement of the spin Hall effect*, Nature **442**, 176 (2006).
- [102] K. Uchida, S. Takahashi, K. Harii, J. Ieda, W. Koshibae, K. Ando, S. Maekawa and E. Saitoh, *Observation of the spin Seebeck effect*, Nature **455**, 778 (2008).
- [103] C. Suarez, W.E. Bron, and T. Juhasz, *Dynamics and Transport of Electronic Carriers in Thin Gold Films*, Phys. Rev. Lett. **75**, 4536 (1995).

- [104] E. Knoesel, A. Hotzel, and M. Wolf, *Ultrafast dynamics of hot electrons and holes in copper: Excitation, energy relaxation, and transport effects*, Phys. Rev. B **57**, 12812 (1998).
- [105] J. Hohlfeld, S.-S. Wellershoff, J. Güdde, U. Conrad, V. Jähnke, E. Matthias, *Electron and lattice dynamics following optical excitation of metals*, Chem. Phys. **251**, 237 (2000).
- [106] H.E. Elsayed-Ali, T. Juhasz, *Femtosecond time-resolved thermomodulation of thin gold films with different crystal structures*, Phys. Rev. B **47**, 13599 (1993).
- [107] Refractive Index Database, <http://refractiveindex.info>
- [108] X. Liu, R. Stock, and W. Rudolph, *Ballistic electron transport in Au films*, Phys. Rev. B **72**, 195431 (2005).
- [109] A. Eschenlohr, M. Battiato, P. Maldonado, N. Pontius, T. Kachel, K. Holl-dack, R. Mitzner, A. Föhlich, P.M. Oppeneer, and C. Stamm, *Hot Electron Mediated Ultrafast Demagnetization of Ni*, in preparation (2012).
- [110] V.P. Zhukov, E.V. Chulkov, and P.M. Echenique, *GW+T theory of excited electron lifetimes in metals*, Phys. Rev. B **72**, 155109 (2005).
- [111] A. Melnikov, I. Razdolski, T.O. Wehling, E.Th. Papaianou, V. Roddatis, P. Fumagalli, O. Aktsipetrov, A.I. Lichtenstein, and U. Bovensiepen, *Ultrafast Transport of Laser-Excited Spin-Polarized Carriers in Au/Fe/MgO(001)*, Phys. Rev. Lett. **107**, 076601 (2011).
- [112] T. Popmintchev, M.-C. Chen, D. Popmintchev, P. Arpin, S. Brown, S. Al-isauskas, G. Andriukaitis, T. Balciunas, O.D. Mücke, A. Pugzlys, A. Baltuska, B. Shim, S.E. Schrauth, A. Gaeta, C. Hernandez-Garcia, L. Plaja, A. Becker, A. Jaron-Becker, M.M. Murnane, H.C. Kapteyn, *Bright Coherent Ultrahigh Harmonics in the keV X-ray Regime from Mid-Infrared Femtosecond Lasers*, Science **336**, 1287 (2012).
- [113] C. La-O-Vorakiat, E. Turgut, C.A. Teale, H.C. Kapteyn, M.M. Murnane, S. Mathias, M. Aeschlimann, C.M. Schneider, J.M. Shaw, H.T. Nembach, T.J. Silva, *Ultrafast Demagnetization Measurements Using Extreme Ultraviolet Light: Comparison of Electronic and Magnetic Contributions*, Phys. Rev. X **2**, 011005 (2012).
- [114] G. Geloni, V. Kocharyan, E. Saldin, *Circular polarization control for the LCLS baseline in the soft X-ray regime*, arXiv: 1012.5154v1 (2010).
- [115] S. Flewett, S. Schaffert, J. Mohanty, E. Guehrs, J. Geilhufe, C.M. Günther, B. Pfau, and S. Eisebitt, *Method for Single-Shot Coherent Diffractive Imaging of Magnetic Domains*, Phys. Rev. Lett. **108**, 223902 (2012).
- [116] C. Gutt et al., *Resonant magnetic scattering with soft x-ray pulses from a free-electron laser operating at 1.59 nm*, Phys. Rev. B **79**, 212406 (2009).
- [117] C. Gutt et al., *Single-pulse resonant magnetic scattering using a soft x-ray free-electron laser*, Phys. Rev. B **81**, 100401(R) (2010).
- [118] J. Andruszkow et al., *First Observation of Self-Amplified Spontaneous Emission in a Free-Electron Laser at 109 nm Wavelength*, Phys. Rev. Lett. **85**, 3825 (2000).

- [119] G. Margaritondo and P.R. Ribic, *A simplified description of X-ray free-electron lasers*, J. Synchrotron Rad. **18**, 101 (2010).
- [120] A.L. Cavalieri et al., *Clocking Femtosecond X Rays*, Phys. Rev. Lett. **94**, 114801 (2005).
- [121] S. Cunovic et al., *Time-to-space mapping in a gas medium for the temporal characterization of vacuum-ultraviolet pulses*, Appl. Phys. Lett. **90**, 121112 (2007).
- [122] R. Radcliffe et al., *Single-shot characterization of independent femtosecond extreme ultraviolet free electron and infrared laser pulses*, Appl. Phys. Lett. **90**, 131108 (2007).

Acknowledgements

I would like to thank many people for being supportive of my work during my time at BESSY II, for interesting discussions, and for generally being great company, in particular ...

... Alexander Föhlisch for agreeing to take over as my supervisor, for continuing encouragement, insightful questions and constructive criticism.

... Christian Stamm for sharing his expert knowledge about magnetic measurements at the Femtoslicing, for giving helpful advice at all times and pointing me into the right direction whenever I got stuck on a particular problem, and for proofreading this thesis. Also, for teaching me that the key to success at the Femtoslicing is to just keep measuring.

... Torsten Kachel and Niko Pontius for help and advice on numerous things ranging from beamline settings to laser pulse length measurements, and for working many early, late and night shifts during our beamtimes.

... Karsten Holldack and Rolf Mitzner for keeping the Femtoslicing source up and running despite machine, electronics, laser, ... problems, algae in the cooling system, and the best efforts of the inventor of the SynchroLock.

... Christoph Trabant, Christian Schüssler-Langeheine and Martin Beye for hilarious and thought-provoking (often at the same time) conversations.

... Ilie Radu, collaborator on the experimental side of the NiFe project.

... my collaborators on the GdTb project: Uwe Bovensiepen, Alexey Melnikov, Nicolas Berggard and Jens Wieczorek.

... Florin Radu for showing me the basics of sample preparation with the magnetron sputtering chamber and for generous help with sample preparation at all times. Also, together with Radu Abrudan, for being great co-workers in the ultimately ill-fated first DyCo beamtime.

... Johan Mentink for his work applying the multisublattice model to NiFe alloys.

... Peter Oppeneer, Marco Battiato and Pablo Maldonado for the superdiffusive spin transport simulations.

... Roland Mattheis and Konstantin Kirsch from IPHT Jena for the FM/Ru/FM samples.

...my predecessor Marko Wietstruk for helping me get started during my first months at BESSY II.

...Femtosing users Kadir Vahaplar, Ilya Razdolski, Loïc Le Guyader and Kristian Döbrich, for, well, being model users.

...my office colleagues Vicente Zamudio-Bayer, Setti Thirupathaiiah and René Könnecke.

...Tobias Lau for my new office chair.

...Muhammad Sultan for giving me an early copy of his PhD thesis.

...Hermann Dürr for offering me the PhD position at BESSY II.

...Christian Back, Georg Woltersdorf and Alexander Weber for getting me interested in the topic of ultrafast magnetization dynamics during my Master's thesis.

...Yves Acremann and the other members of the FLASH collaboration on time- and spin-resolved photoemission from ETH Zürich, PSI, DESY, University of Hamburg and SLAC for giving me some insight into experimenting at another large scale facility.

Funding for the Femtoslicing upgrade from the German Ministry of Education and Research BMBF Grant 05K10PG2 "FEMTOSPEX" is gratefully acknowledged.

Hiermit erkläre ich, dass die Arbeit an keiner anderen Hochschule eingereicht sowie selbstständig und nur mit den angegebenen Mitteln angefertigt wurde.

Potsdam, den 22.06.2012